Control and Optimization of Electric Ship Propulsion Systems with Hybrid Energy Storage

by

Jun Hou

A dissertation submitted in partial fulfillment
of the requirements for the degree of
Doctor of Philosophy
(Electrical Engineering: Systems)
in the University of Michigan
2017

Doctoral Committee:

Professor Heath Hofmann, Co-Chair
Professor Jing Sun, Co-Chair
Professor Ilya Vladimir Kolmanovsky
Assistant Professor Johanna Mathieu

Jun Hou

junhou@umich.edu

ORCID iD: 0000-0001-7116-2945

ACKNOWLEDGEMENTS

First of all, I would like to give my deepest gratitude to my advisors, Professor Jing Sun and Professor Heath Hofmann, whose consistent encouragement and support helped me to overcome many challenges in my research and complete this dissertation. It is a great honor for me to work with them. They can always predict future obstacles and opportunities to make my research "trajectory" within "constraints" during my nonlinear non-convex Ph.D. life. I also would like to thank my dissertation committee members, Professor Ilya Kolmanovsky and Professor Johanna Mathieu, for their constructive comments and helpful suggestions.

I would like to gratefully and sincerely thank all of my colleagues and friends for their support, discussions and friendship. I want to express my special thanks to Dr. Kan Zhou and Dr. Ziyou Song. It is my great pleasure to work and study with them. I want to thank Dr. Dave Reed and Dr. Hyeongjun Park for their valuable advices and discussions. I want to thank all of my colleagues in RACE Lab and MPEL Lab: Dr. Caihao Weng, Dr. Zhenzhong Jia, Dr. Qiu Zeng, Dr. Esteban Castro, Dr. Richard Choroszucha, Dr. Mohammad Reza Amini, Dr. Aaron Stein, Dr. Fei Lu, Dr. Abdi Zeynu, Kai Wu, Hao Wang, Yuanying Wang, Fanny Pinto Delgado, Jake Chung, and my friends at Michigan: Dr. Xiaowu Zhang, Dr. Tianyou Guo, Dr. Heng Kuang, Chaozhe He, Rui Chen, Ziheng Pan, Yuxiao Chen, Zheng Wang, Yuxi Zhang, Xin Zan, Bowen Li, Sijia Geng and many others (the names could continue without an end).

I wish to acknowledge the U.S. Office of Naval Research (N00014-11-1-0831 and

N00014-15-1-2668) and the Naval Engineering Education Center to support my research.

Finally, I would like to express my greatest gratitude to my parents, Wencai Hou and Fenghui Li, for their love and faith in me, support, and encouragement throughout my life. And to Xintong Zhang, managing a long distance relationship is even more difficult than finishing the Ph.D. study. I am very happy that we are able to conquer all the "constraints" to obtain the feasible optimal solution.

TABLE OF CONTENTS

ACKNOWLEDGEMENTS ii

LIST OF FIGURES vii

LIST OF TABLES xiii

LIST OF ABBREVIATIONS xv

ABSTRACT xvii

CHAPTER

I. Introduction 1

1.1 Background 1
1.1.1 All-Electric Ships with Integrated Power System . . 1
1.1.2 Energy Storage Devices for All-Electric Ships 6
1.1.3 Energy Management for All-Electric Ships 8
1.2 Motivation 9
1.3 Main Contributions 12
1.4 Outline 15

II. Dynamic Model of An Electric Ship Propulsion System with Hybrid Energy Storage 19

2.1 Propeller and Ship Dynamic Model 19
2.1.1 Propeller Characteristics 20
2.1.2 Ship Dynamics 22
2.2 Hybrid Energy Storage System Model 25
2.3 DC Bus Dynamic Model 28
2.4 Electric Power Generation and Propulsion Motor Model . . . 28
2.5 Summary 31

III. A Low-Voltage Test-bed for Electric Ship Propulsion Systems with Hybrid Energy Storage 32

3.1 MPEL AED-HES Test-bed 32
3.1.1 System Controller 34
3.1.2 Electric Machines and Power Electronic Inverters . . 35
3.1.3 Energy Storage 36
3.2 Energy Cycling Capability of Battery and Ultra-capacitor . . 40
3.3 Energy Cycling Capability of Flywheel and Ultra-capacitor . 44
3.4 Summary 45

IV. Hybrid Energy Storage Configuration Evaluation: Battery with Flywheel vs. Battery with Ultracapacitor 46

4.1 Performance Evaluation of B/FW And B/UC HESS Configurations 47
4.1.1 Problem Formulation 47
4.1.2 Performance Evaluation 49
4.2 Receding Horizon Control for Real-Time Power Management 55
4.3 Summary 62

V. Control Strategies Evaluation: Coordinated Control vs. Prefiltered Control 64

5.1 MPC Problem Formulation 65
5.2 Performance Comparison and Results Analysis 68
5.2.1 Case I: Constant Propeller Rotational Speed 69
5.2.2 Case II: Regulated Propeller Rotational Speed by a PI Controller 73
5.3 Summary 76

VI. Energy Management Strategies for An Electric Ship Propulsion System with Hybrid Energy Storage 77

6.1 Energy Management Strategies for the Plug-in Configuration 78
6.1.1 Baseline Control System without HESS 79
6.1.2 Motor Load Following Control with HESS 80
6.1.3 Bus Voltage Regulation with HESS 82
6.1.4 Coordinated HESS EMS 86
6.1.5 Comparative Study and Simulation Results 88
6.2 Energy Management Strategies for the Integrated Configuration 91
6.2.1 Integrated System-Level EMS 92
6.2.2 Comparative Study and Simulation Results 96
6.3 Summary 99

VII. Load Torque Estimation and Prediction for An Electric Ship Propulsion System 101

7.1 Energy Management Strategy Formulation 103
7.1.1 AMPC Problem Formulation 103
7.2 Propulsion-load Torque Estimation and Prediction 105
7.2.1 First Approach: Input Observer with Linear Prediction 105
7.2.2 Second Approach: Adaptive Load Estimation/Prediction with Model Predictive Control 107
7.3 Performance Evaluation and Discussion 112
7.4 Summary 120
7.5 Appendix of Chapter VII: Derivation of simplified propulsion-load model 121

VIII. Experimental Implementation of Real-time Model Predictive Control 123

8.1 Problem Formulation 124
8.2 System-level Controller Development: Energy Management Strategy 126
8.3 Component-level Controller Development: Current Regulators for HESS 128
8.4 Experimental Implementation and Performance Evaluation . 132
8.5 Summary 142

IX. Conclusions and Future Work 143

9.1 Conclusions 143
9.2 Ongoing and Future Research 146

BIBLIOGRAPHY 148

LIST OF FIGURES

Figure

1.1 A comparison of traditional mechanical drive and IPSs. MD: motor drive; Mtr: motor; Gen: generator. [1] 2

1.2 Specific fuel consumption vs percent rated power of a typical marine diesel engine. [2] 2

1.3 SFC curves for k active diesel engines. [3] 3

1.4 Ragone plot: Comparison of energy storage energy and power density. [4] 7

1.5 Diagram of the conceptual electric propulsion system with hybrid energy storage. 11

2.1 Model structure of the electric ship propulsion system with HESS. . 20

2.2 Propeller and ship dynamics model structure. 20

2.3 Load power fluctuations (top plots), zoomed-in fluctuations (middle plots), and their frequency spectrums (bottom plots). 25

2.4 DC bus dynamic representation. 29

2.5 Model structure of electric power generation system. 30

2.6 Linearized model responses of the generator and the diode rectifier at three different operating points. 30

3.1 Electrical schematic of the MPEL test-bed. 33

3.2 MPEL AED-HES test-bed. 34

3.3 Flywheel module of MPEL test-bed. 38

3.4 Battery module of MPEL test-bed. 39

3.5 UC module of MPEL test-bed. 40

3.6 Experimental setup for the energy cycling test using batteries and ultra-capacitors. 41

3.7 Multi-frequency load power fluctuations generated by the resistive load bank. 41

3.8 DC bus voltage without HESS bus voltage regulators. 41

3.9 Schematic of the independent bus voltage regulation control using batteries and ultra-capacitors. 42

3.10 DC bus voltage with independent bus voltage regulators using batteries and ultra-capacitors: (a) bus voltage (left) and (b) UC voltage (right). 42

3.11 Schematic of the filter-based control using batteries and ultra-capacitors. 43

3.12 DC bus voltage with filter-based control using batteries and ultra-capacitors: (a) bus voltage (left) and (b) UC voltage (right). 43

3.13 Experimental setup for the energy cycling test using the flywheel and ultra-capacitors. 44

3.14 Schematic of the filter-based control using the flywheel and ultra-capacitors. 44

3.15 DC bus voltage with filter-based control using the flywheel and ultra-capacitors: (a) bus voltage (left) and (b) UC voltage (right). 45

4.1 Pareto-fronts of B/FW and B/UC HESS at sea state 2. 50

4.2 Pareto-fronts of B/FW and B/UC HESS at sea state 4. 51

4.3 Pareto-fronts of B/FW and B/UC HESS at sea state 6. 51

4.4 Pareto-fronts of B/FW and B/UC HESS at sea states 2,4 and 6 with different battery state of health. 56

4.5 B/FW HESS performance at sea state 4 without any penalty on the speed of FW. 58

4.6 The flywheel SOC of MOP dynamic programming solutions with different initial SOCs. 58

4.7 The performance comparison: MPC vs. DP. 60

4.8 MPC (N=20, without UC SOC penalty) performance at sea state 4. 62

4.9 MPC (N=20, with UC SOC penalty) performance at sea state 4. . . 62

5.1 Control strategy diagram: left: PF-MPC, right: CC-MPC. 65

5.2 Pareto-fronts of UC-Only, CC-MPC and PF-MPC at sea state 4 (N=20). 69

5.3 Pareto-fronts of UC-Only, CC-MPC and PF-MPC at sea state 6 (N=20). 70

5.4 CC-MPC and PF-MPC performance at sea state 4. 71

5.5 Sensitivity analysis of predictive horizon for CC-MPC at sea state 4. 72

5.6 Sensitivity analysis of predictive horizon for CC-MPC at sea state 6. 73

5.7 Pareto-fronts of Case I and II at sea state 4 (N=20). 74

5.8 Pareto-fronts of Case I and II at sea state 6 (N=20). 74

5.9 The HESS output currents of CC-MPC (Case II) at sea state 4. . . 75

6.1 Schematic of the electric propulsion system with HESS control strategies for the comparative study. 79

6.2 The block diagram of the feedback system with the baseline strategy. 80

6.3 The bus voltage response with the baseline strategy at sea state 4. . 81

6.4 Performance comparison of BL and MLF: bus voltage response (top plots) and their frequency spectrums (bottom plots) at sea state 4. . 82

6.5 The block diagram of the feedback system with the MLF strategy. . 83

6.6 Bode plot of load fluctuation response ($LF \rightarrow E_{DC}$) by BL and MLF. 83

6.7 Performance comparison of BL and BVR: bus voltage response (top plots) and their frequency spectrums (bottom plots). 84

6.8 The block diagram of the feedback system for the BVR strategy. . . 85

6.9 Bode plot of load fluctuation response ($LF \rightarrow E_{DC}$) by BL and BVR. 85

6.10 Undesirable interaction: fluctuating currents from the generator and battery pack for the system with BVR. 86

6.11 Performance comparison of BL and EMS: bus voltage response (top plots) and their frequency spectrums (bottom plots). 88

6.12 Performance comparison: BL, BVR and EMS. 90

6.13 Schematic of HESS-EMS for the electric propulsion system with HESS. 91

6.14 Schematic of SYS-EMS for the electric propulsion system with HESS. 93

6.15 Performance of HESS-EMS and SYS-EMS at Sea State 4. 97

6.16 Performance of HESS-EMS and SYS-EMS with pulse power load at Sea State 4. 98

7.1 Bode plot of the input observer. 107

7.2 Schematic diagram of the first approach (IO-LP). 107

7.3 Outputs of the detailed and simplified propeller-load torque models at sea state 4 (top) and sea state 6 (bottom). 109

7.4 Schematic diagram of the AMPC controller. 111

7.5 Estimation error of the adaptive load estimation and input observer. 113

7.6 Cases 2 and 3 degraded "Total Cost" performance compared to Case 1.115

7.7 Cases 4 and 5 degraded "Total Cost" performance compared to Case 1.115

7.8 Cases 2 and 4 degraded "Total Cost" performance compared to Case 1.116

7.9 Cases 3 and 5 degraded "Total Cost" performance compared to Case 1.117

7.10 Cases 2-6 degraded "Torque Oscillation Reduction" performance compared to Case 1. 118

7.11 Torque comparison at sea states 4 and 6: Case 6 vs. Test 1. 120

8.1 Simplified DC bus dynamic model of the AED-HES test-bed. 124

8.2 Schematic of the filter-based control. 125

8.3 Schematic of the real-time MPC. 126

8.4 Flowchart of the IPA-SQP algorithm [5]. 128

8.5 Hierarchical control structure for real-time control implementation. . 129

8.6 Circuit diagram of bi-directional DC/DC converters for HESS. . . . 129

8.7 The implementation of Speedgoat controller. 131

8.8 Matlab/Simulink program of the local controllers. 132

8.9 Control performance: battery and UC command power and actual power (zoom-in plots in the bottom). 133

8.10 Multi-core structure of Speedgoat. 134

8.11 Real-time simulation evaluation of system-level controller (core1). . 134

8.12 Real-time simulation evaluation of component-level controllers (core2). 134

8.13 Diagram of real-time MPC experiment. 136

8.14 Experimental results of sea state 4: MPC vs. filter-based control . . 136

8.15 Experimental results of sea state 6: MPC vs. filter-based control. . 137

8.16 Experimental results of pulse power load: MPC vs. filter-based control. 138

8.17 Experimental results of sea state 4: MPC(N=20) vs. MPC(N=40). . 139

8.18 Experimental results of sea state 6: MPC(N=20) vs. MPC(N=40). . 140

8.19 Experimental results of pulse power load: MPC(N=20) vs. MPC(N=40) 141

8.20 UC output current and the number of iteration to solve the optimization problem. 141

8.21 Real-time simulation comparison of maximum execution time. . . . 142

LIST OF TABLES

Table

1.1 The characteristics of battery, UC and flywheel. 8

2.1 Ship parameters 24

2.2 Hybrid energy storage parameters. 27

2.3 Requirement based on sea state 4 28

2.4 HESS configuration and size selection. 28

3.1 Manufacturer specifications for system controller. 35

3.2 Manufacturer specifications for electric machines. 36

3.3 Manufacturer specifications for flywheel. 37

3.4 Specifications for the battery system. 39

3.5 Specifications for the ultra-capacitors. 39

4.1 Performance metrics. 52

4.2 Performance comparison of the selected design points. 53

4.3 Performance comparison of the proposed MPC and DP. 61

6.1 Properties of control strategies. 79

6.2 Performance comparison of different control strategies. 89

6.3 EMS performance comparison. 100

7.1 Control objectives and their mathematical expression. 102

7.2 Performance metrics. 111

7.3 Performance comparison. 114

7.4 Performance comparison: Case 6 vs. Case 1 with 2% modeling error. 119

7.5 Performance comparison: weighting factor effects. 119

8.1 Performance comparison: filter-based vs. MPC. 135

8.2 Performance comparison: MPC(N=20) vs. MPC(N=40). 139

LIST OF ABBREVIATIONS

AED Advanced Electric Drive

AES All-Electric Ship

AMPC Adaptive Load Estimation/Prediction with Model Predictive Control

BCM Battery Control Module

BMS Battery Management System

BVR Bus Voltage Regulation

B/FW Battery with Flywheel

B/UC Battery with Ultra-capacitor

CC Coordinated Control

CPP Controllable Pitch Propeller

EMS Energy Management Strategy

ESD Energy Storage Device

FPP Fixed Pitch Propeller

HESS Hybrid Energy Storage System

HEV Hybrid electric vehicle

IM Induction Machine

IO Input Observer

IPS Integrated Power System

LP Linear Prediction

LPC Linear Prediction Coefficient

MLF Motor Load Following

MOP Multi-objective Optimization Problem

MPC Model Predictive Control

MPEL University of Michigan Power and Energy Lab

PM Prime Mover

PF Pre-filtering

RMS Root Mean Square

UPS Uninterruptible Power Supply

SOC State of Charge

SQP Sequential Quadratic Programming

SS Sea State

UC Ultra-capacitor

VSD Variable Speed Drives

ABSTRACT

Electric ships experience large propulsion-load fluctuations on their drive shaft due to encountered waves and the rotational motion of the propeller, affecting the reliability of the shipboard power network and causing wear and tear. This dissertation explores new solutions to address these fluctuations by integrating a hybrid energy storage system (HESS) and developing energy management strategies (EMS). Advanced electric propulsion drive concepts are developed to improve energy efficiency, performance and system reliability by integrating HESS, developing advanced control solutions and system integration strategies, and creating tools (including models and testbed) for design and optimization of hybrid electric drive systems.

A ship dynamics model which captures the underlying physical behavior of the electric ship propulsion system, is developed to support control development and system optimization. To evaluate the effectiveness of the proposed control approaches, a state-of-the-art testbed has been constructed which includes a system controller, Li-Ion battery and ultra-capacitor (UC) modules, a high-speed flywheel, electric motors with their power electronic drives, DC/DC converters, and rectifiers.

The feasibility and effectiveness of HESS are investigated and analyzed. Two different HESS configurations, namely battery/UC (B/UC) and battery/flywheel (B/FW), are studied and analyzed to provide insights into the advantages and limitations of each configuration. Battery usage, loss analysis, and sensitivity to battery aging are also analyzed for each configuration. In order to enable real-time application and achieve desired performance, a model predictive control (MPC) approach is developed, where a state of charge (SOC) reference of flywheel for B/FW or UC

for B/UC is used to address the limitations imposed by short predictive horizons, because the benefits of flywheel and UC working around high efficiency range are ignored by short predictive horizons. Given the multi-frequency characteristics of load fluctuations, a filter-based control strategy is developed to illustrate the importance of the coordination within the HESS. Without proper control strategies, the HESS solution could be worse than a single energy storage system solution.

The proposed HESS, when introduced into an existing shipboard electrical propulsion system, will interact with the power generation systems. A model-based analysis is performed to evaluate the interactions of the multiple power sources when a hybrid energy storage system is introduced. The study has revealed undesirable interactions when the controls are not coordinated properly, and leads to the conclusion that a proper EMS is needed.

Knowledge of the propulsion-load torque is essential for the proposed system-level EMS, but this load torque is immeasurable in most marine applications. To address this issue, a model-based approach is developed so that load torque estimation and prediction can be incorporated into the MPC. In order to evaluate the effectiveness of the proposed approach, an input observer with linear prediction is developed as an alternative approach to obtain the load estimation and prediction. Comparative studies are performed to illustrate the importance of load torque estimation and prediction, and demonstrate the effectiveness of the proposed approach in terms of improved efficiency, enhanced reliability, and reduced wear and tear.

Finally, the real-time MPC algorithm has been implemented on a physical testbed. Three different efforts have been made to enable real-time implementation: a specially tailored problem formulation, an efficient optimization algorithm and a multi-core hardware implementation. Compared to the filter-based strategy, the proposed real-time MPC achieves superior performance, in terms of the enhanced system reliability, improved HESS efficiency, and extended battery life.

CHAPTER I

Introduction

1.1 Background

1.1.1 All-Electric Ships with Integrated Power System

Electric propulsion in marine applications is not a new concept, dating back over 100 years [6, 7, 8]. Recently, marine electrification has become increasingly popular after the development of high power variable speed drives (VSDs) in the 1970's-1980's [6, 9, 10]. With the introduction of VSDs, a common set of generators could power both the ship service and propulsion systems. This concept is referred to as an integrated power system (IPS), which is the characterizing element of an all-electric ship (AES) [1, 9, 10, 11, 12]. The comparison of traditional mechanical drive and IPSs is shown in Figure 1.1.

The IPS architecture provides the electrical power for both ship service and electric propulsion loads by integrating power generation, distribution, storage and conversion. Compared to the traditional mechanical drive, the benefits of IPS are summarized in the following:

- IPS improves the efficiency of the prime movers [1, 2, 3, 6, 7, 13, 14, 15]: The optimal operating power of marine diesel engines is typically between 70%-90% of their rated power; however, they often operate at 20-50% of their rated power

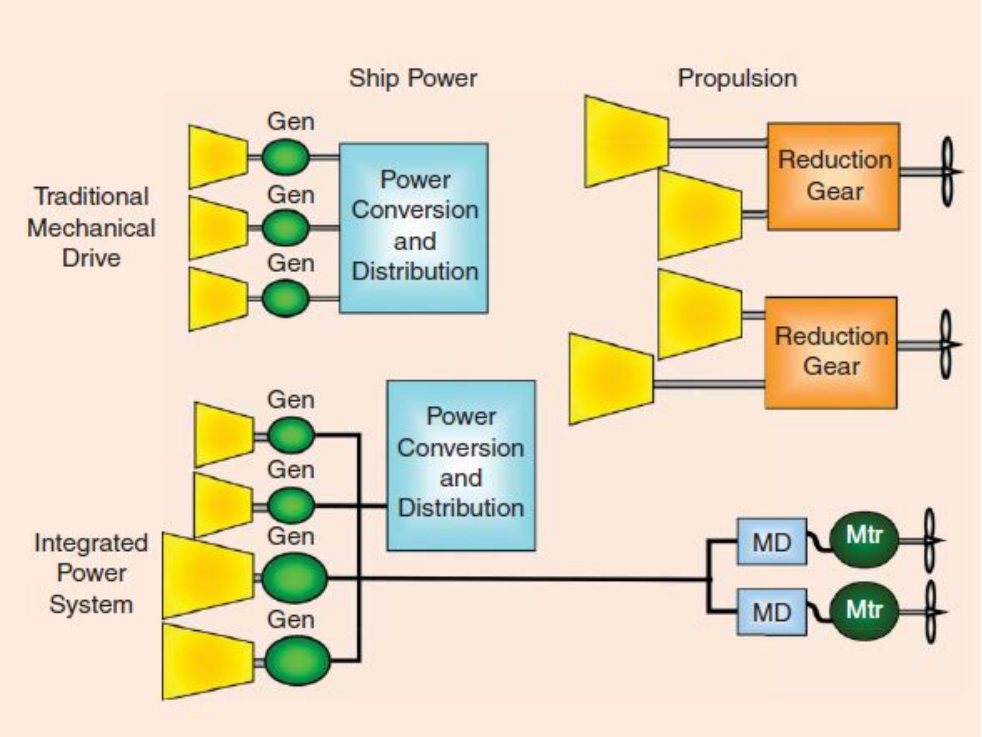

Figure 1.1: A comparison of traditional mechanical drive and IPSs. MD: motor drive; Mtr: motor; Gen: generator. [1]

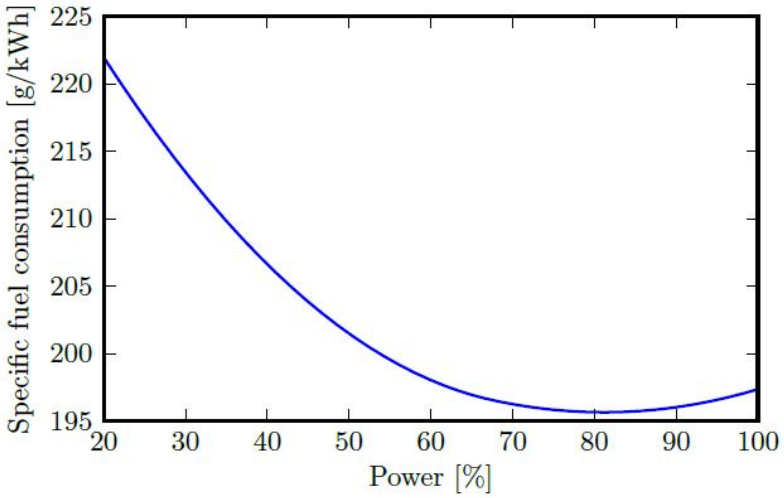

Figure 1.2: Specific fuel consumption vs percent rated power of a typical marine diesel engine. [2]

[2], especially for large military ships. The specific fuel consumption of a typical marine diesel engine is shown in Figure 1.2. Since the prime movers do not

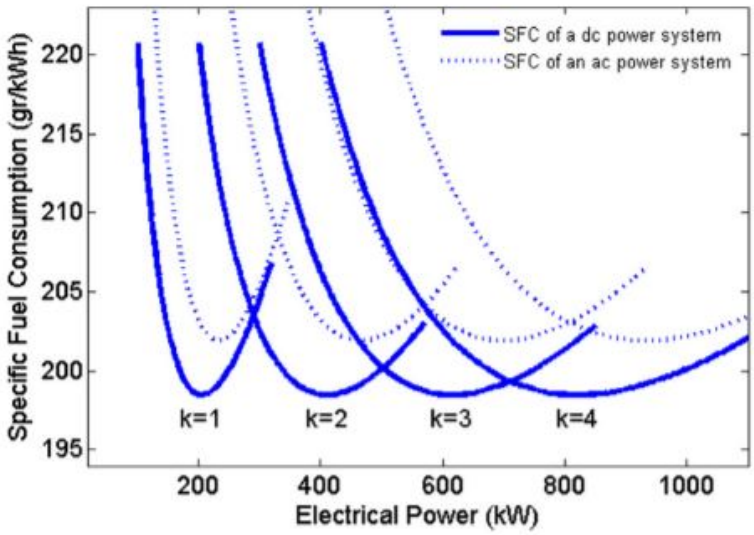

Figure 1.3: SFC curves for k active diesel engines. [3]

operate in their most efficient speed and power range under many operating conditions, the overall prime mover efficiency can be significantly degraded. IPS is able to optimize the number of operating prime mover and generator sets based on the overall power of the propulsion system and ship service systems. For example, as shown in Figure 1.3 [3], when the total power requirement is less than 300kW, only 1 prime mover and generator set will operate; if it is between 300kW and 500kW, then 2 generators are preferred. Therefore, the overall system efficiency of an IPS configuration can be considerably higher than that of an equivalent mechanical drive design, particularly at low power levels. As a result, fuel consumption and emissions are reduced [6].

- IPS improves the efficiency of the propulsors [1, 13, 15]: In an integrated power system, the traditional controllable-pitch propeller (CPP) in the propulsion-shaft line can be replaced by a high-efficiency fixed-pitch propeller (FPP). The CPP is able to control the ship's speed, both forward and reverse. This is important when the propeller is coupled with prime movers such as diesel engines and gas turbines that are not reversible and may have a minimum operating

rotational speed. Compared to FPP, CPP needs a large hub to hold the apparatus in order to adjust its pitch. Due to this large hub, the efficiency of CPP will be reduced. In contrast, the motors in IPS are able to operate from zero to their maximum speed for both forward and reverse operation. As a result of this characteristic, a high-efficiency FPP can be employed in IPS.

- IPS provides flexibility of arrangements [1, 7, 13, 14, 16]: For the electrical network, the prime mover and generator sets can be placed almost anywhere, which offers flexibility to the designers. Furthermore, long shaft lines can be simplified with direct motor drives, leading to space saving.

- IPS improves the survivability of electrical systems [1, 7, 14, 15, 16, 17]: IPS supports zonal survivability, which is the ability of a distributed system to ensure that loads in one zone do not experience a service interruption by faults which occurs in other zones. Zonal survivability also facilitates the ship's ability to maintain or restore the damaged zones without interrupting other zones.

- IPS supports high-power mission systems, such as high-power radar and weapon systems [1, 15]: As the demand of power missions increases [4, 18], it is essential to support high-power mission systems for future naval ships. IPS outperforms traditional mechanical drives in coordinating the propulsion system with ship service systems. Usually, the need for high-power mission systems is not required at the same time as maximum propulsion. The power sharing ability of IPS requires less generator sets than non-integrated power systems to support the same high-power mission systems, contributing to acquisition savings, reduced maintenance costs, and reduced volume.

- IPS offers a more comfortable residential environment [15, 16]: Because of the reduction of mechanical equipment, such as long shafts and large gearboxes, noise and vibration, can be significantly attenuated by an electric propulsion

system. This is one of the main reasons that IPS has become standard in large cruise ships [16].

IPS provides considerable benefits to modern ships; at the same time, it faces challenges. One of these challenges is propulsion load fluctuations from the propeller. These load fluctuations do not affect the electrical shipboard network in traditional mechanical drives, because the fluctuations are isolated by the non-integrated power system. For the integrated power system, however, these fluctuations can affect the electrical shipboard network.

Three different types of propulsion load fluctuation are studied in the literature [19, 20, 21, 22, 23, 24, 25, 26]:

- fluctuations from the impact of the first order wave at the encounter wave frequency (load periods typically from seconds to minutes),
- fluctuations from the in-and-out-of-water effect (load periods in seconds),
- fluctuations caused by the propeller rotation at the propeller-blade frequency (i.e. number of blades times shaft speed in revolutions per second).

The impact of the encounter-wave-frequency fluctuations combined with the in-and-out-of-water effect has also been reported in the literature [19, 20, 21, 22, 23]. These fluctuations, especially when the propeller is in-and-out-of-water, will significantly reduce electrical efficiency, affect power quality on the shipboard power network, and cause wear and tear. The fluctuations caused by the in-and-out-of-water effect can be as high as 100% of the nominal power. These two load fluctuations are defined as low-frequency fluctuations in this dissertation.

The high-frequency fluctuation discussed in this dissertation is at the propeller-blade frequency (i.e. number of blades times shaft speed in rps) [19, 20, 21, 22]. This fluctuation, caused by the wake field, has been discussed in [24]. The Fourier

analysis of the wake field, discussed in Chapter 5 of [25], is used to capture these high-frequency dynamics. It it worth noting that the fluctuations at the propeller-blade frequency can be very significant during ventilation [19]. The experimental results of the propeller at both non-ventilation and ventilation conditions were provided by [26], where significantly large torque fluctuations at both high and low frequencies were observed. The importance of the mechanical effects caused by the propeller-blade frequency fluctuations has been discussed in [19, 20, 21, 22]. This high-frequency fluctuation is reported as one of the main causes for severe mechanical wear and tear of the propulsion unit. The impact on the electrical system, however, highly depends on the propeller inertia and the associated controller.

1.1.2 Energy Storage Devices for All-Electric Ships

The importance of Energy Storage Device (ESD) development in the electrification of ships is highlighted in the Naval Next Generation Integrated Power System Technology Development Roadmap in 2007 and 2013 [4, 18], where batteries, ultra-capacitors (UCs), and flywheels are discussed as possible ESDs. The battery is an electrochemical device with high energy density but relatively poor power density. In contrast, ultra-capacitors store energy in an electric field without chemical reactions, while flywheels store energy mechanically in the form of kinetic energy, both yielding power densities that are much higher than that of batteries. However, their lower energy densities make ultra-capacitors and flywheels unsuitable for sustained operation. The Ragone plot of batteries, ultra-capacitor (double-layer capacitors) and flywheel is shown in Figure 1.4. These complementary characteristics of batteries, ultra-capacitors, and flywheels suggest that different combinations of ESDs should be considered for different applications [4, 27]. Only using one single type of ESD can result in increased size, weight and cost for electric ship operations [28]. The combination of different ESDs is defined as a Hybrid Energy Storage System (HESS).

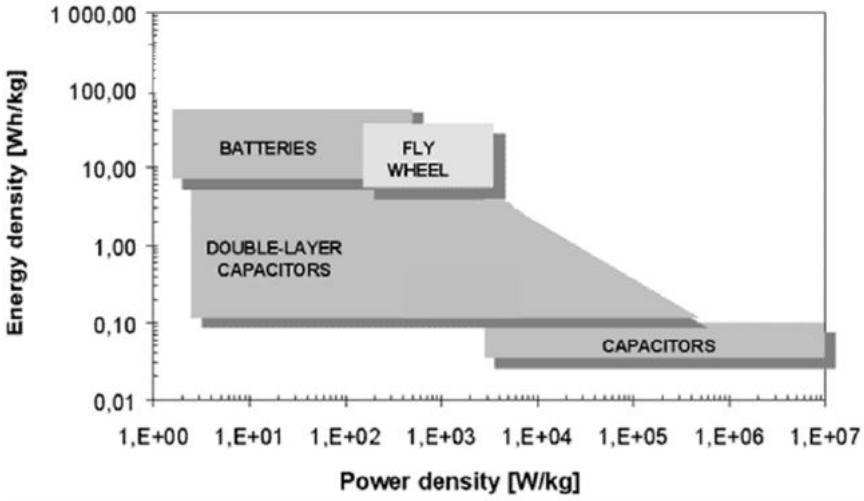

Figure 1.4: Ragone plot: Comparison of energy storage energy and power density. [4]

ESDs (namely batteries, UCs and flywheels) and their combinations (i.e., HESS) have been explored by the automotive, power system and control engineering communities. ESDs and HESSs are widely used in applications, such as electric/hybrid electric vehicles [29, 30, 31, 32, 33, 34, 35], micro grids [36, 37, 38, 39], and uninterruptible power supplies (UPS) [4, 40]. However, the ESDs/HESSs in marine applications are still understudied [4]. The potential benefits of integrating ESDs/HESSs have been reported in the literature. In order to support pulse power loads, such as high-power radar and lasers, UCs have been used in [41, 42] and flywheels have been studied in [43, 44, 45]. The combination of the battery, UC and flywheel for mitigating pulse power loads is studied in [46]. Note that the studies in [41, 43, 44, 45, 46] are based on simulations, while the approach in [42] is experimentally validated. In order to reduce wear and tear on the generator sets, batteries are used in [2, 47] to "smooth" the generator power. In [17], battery modules are used to assist the turbine and fuel cell in tracking the power command. The reduction of fuel consumption using ESD/HESS has been explored in [3, 48, 49, 50]. A battery ESD is used in [3], and an HESS, which combines batteries with UCs, is studied in [48, 49, 50]. In order to address propulsion load fluctuations, batteries, UCs, flywheels and their combinations,

i.e., HESS, have been studied in [51, 52, 53, 54, 55].

According to the literature review, UCs and flywheels are the best candidate for mitigating pulse power effects. This is because the pulse power load is usually of high power and short duration. The UC and flywheel have higher power density than the battery. Additionally, the UC and flywheel have fast dynamic response to compensate the pulse power load. For a long-duration load, the battery is preferred due to its high energy density. Compared to UC and flywheel, however, the main disadvantages of the battery are its relatively short cycle life and limited recharge rate. Furthermore, as the capacity of the battery degrades, the internal resistance will be increased, leading to increased losses. In order to address the limitations of the battery, the HESS, thanks to its complementary characteristic, is one of the most popular solutions. The characteristics of each ESD are summarized in Table 1.1. Note that the preferred characteristics are in blue and undesirable ones are in red.

Table 1.1: The characteristics of battery, UC and flywheel.

	Battery	UC	Flywheel
Energy density	High	Low	Medium
Power density	Low	High	Medium
Cycle life	Short	Medium	Long
Recharge rate	Low	High	Medium
Self-discharge	Low	Medium	High

1.1.3 Energy Management for All-Electric Ships

Energy/power management strategies coordinate multiple power sources and multiple power loads, in order to achieve robust and efficient operation and to meet various dynamic requirements. An effective energy management system is needed to provide improved fuel efficiency, enhanced response speed, superior reliability and reduced mechanical wear and tear [17, 42, 47, 56]. In order to achieve these expectations, optimization-based energy management is required to address the trade-offs among these objectives. Furthermore, optimization-based energy management is also

suggested in the Naval Power Systems Technology Development Roadmap [4]. The characteristics of IPS in all-electric ships have been summarized in [56], including:

- Nonlinear and multi-input-and-multi-output plant characteristics;
- Reconfigurable underlying physical components;
- Multi-scale time dynamics;
- Multiple operating constraints.

These characteristics suggest model predictive control (MPC) as a natural choice for optimization-based energy management strategies. Energy management strategies using MPC have been investigated in the literature. A sensitivity-function-based approach is proposed in [17], which achieves real-time trajectory tracking. In [42, 57], a nonlinear MPC is developed to compensate pulse power loads and follow the desired references, including the desired bus voltage, desired reference power for generator sets and desired reference speed for the motor. In [47], a stochastic MPC is developed to smooth out power fluctuations. A multi-level MPC is used in [50] to address disturbances from the environment. The main challenge to implement the model predictive control approaches discussed above is to solve the optimization problem in real-time within a relatively short sampling time. In order to evaluate the effectiveness of the proposed approach, the energy management strategy developed in this dissertation is implemented on a test-bed. To our best knowledge, the study in [42] is the only one prior to this work, which has demonstrated the feasibility of optimization-based shipboard energy management with test results on a physical platform.

1.2 Motivation

Ship electrification has been a technological trend in commercial and military ship development in response to recent energy efficiency and environmental protection ini-

tiatives [4, 18]. Electric propulsion plays a central role in this design paradigm shift. The introduction of electric propulsion has brought about new opportunities for taking a fresh look at old problems and developing new solutions. Thrust and torque fluctuations due to the hydrodynamic interactions and wave excitations have been identified as inherent elements in the ship propulsion system [19, 20, 24, 26, 58]. As discussed in Section 1.1.1, three different propulsion load fluctuations are studied in this research: fluctuations from the impact of the first order wave at the encounter wave frequency, fluctuations from the in-and-out-of-water effect (load periods in seconds) and fluctuations at the propeller-blade frequency (i.e. number of blades times shaft speed in rps). These fluctuations significantly affect the performance and life cycle of both mechanical and electrical systems involved, as has been analyzed in [21, 22, 23, 59]. For mechanical systems, excessive fluctuations on torque and power will increase mechanical stress and cause wear and tear. The importance of the mechanical effects caused by propeller-blade frequency fluctuations has been discussed in [19, 20, 21, 22]. For electrical systems, power fluctuations, especially when the propeller is in-and-out-of-water, will reduce electrical efficiency and affect power quality on the shipboard power network [19, 20, 21, 22, 23, 24, 25, 26]. In order to address these issues, several studies have been discussed in the literature, such as using thrust control for power smoothing [19, 20]. The trade-offs between speed control, torque control, and power control of the motor have been studied in [19]. Using thruster biasing for vessels with dynamic positioning systems has been proposed in [60, 61, 62] to reduce load fluctuations. These methods deal primarily with low-frequency variations and are typically applied to dynamic positioning systems.

In order to address the load fluctuations, a hybrid energy storage system solution is proposed. The concept of the proposed system is shown in Figure 1.5. The energy storage elements serve as a buffer to absorb energy when the motor is underloaded and supply energy when overloaded, thereby isolating the power network from

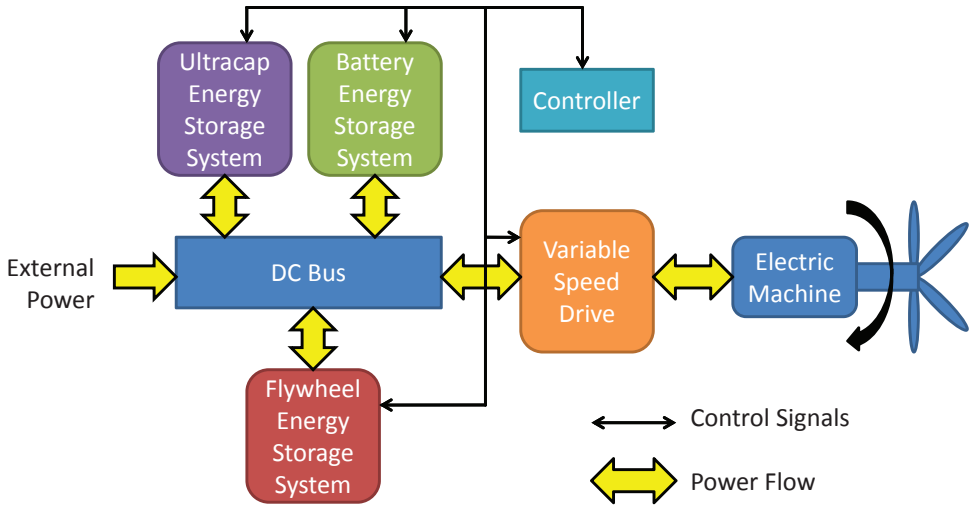

Figure 1.5: Diagram of the conceptual electric propulsion system with hybrid energy storage.

propulsion load fluctuations and improving overall system efficiency. Using different energy storage mechanisms allow one to exploit their different characteristics to address different frequency components in the power and thrust fluctuations. Besides the well-configured HESS, the integration and operation of a shipboard electrical propulsion system with HESS relies on effective power/energy management strategies in order to mitigate the load power fluctuation effects and achieve the desired benefits, in terms of increased system efficiency, improved reliability, and reduced wear and tear. To improve the robustness of the control strategy, addressing the uncertainties in the model, especially in the propulsion load torque model, is one of the key issues. Furthermore, a physical test-bed is required for implementing the control strategies in real-time and evaluating their effectiveness. In summary, the motivation of this research is to answer the following questions:

- How to capture the underlying dynamics in the electric ship propulsion system, especially the propulsion load dynamics, to support control and system integration?

- How to evaluate the benefits and limitations of different energy storage/hybrid

energy storage configurations?

- How to develop an energy management strategy to achieve the desired performance?
- How to accurately estimate and predict the propulsion load torque and demonstrate robustness of the energy management solution?
- How to build a physical test-bed for implementing and evaluating the proposed approaches?

1.3 Main Contributions

This research aims to address propulsion load fluctuations in all-electric ships with HESS. Although HESS has been investigated in many applications, such as hybrid electric vehicle, this is the first attempt to exploit HESS to address propulsion-load fluctuations in all-electric ships. Configuration optimization and energy management strategy development has been studied. A coordinated approach is used to exploit the complementary characteristics of HESS. A system-level energy management strategy is developed using model predictive control. This strategy encompasses the controls of the primary power sources and propulsion motor, in addition to the HESS, and allows judicious coordination to achieve desired performance in terms of increased system efficiency, enhanced reliability, reduced mechanical wear and tear, and improved load-following capability. The main contributions of this research are summarized in the following:

1) Model development [63]: To support research activities associated with the control and optimization of electric ship propulsion systems, a control- and optimization-oriented model is an essential tool for feasibility analysis and system design. The models developed in this dissertation include the propeller

and ship dynamic model, hybrid energy storage models, the diesel engine and generator set model, electrical motor models and the DC bus dynamic model. The main contribution of model development is the propeller and ship dynamic model. To the best knowledge of the author, this is the first model to capture both high- and low-frequency load fluctuations on the propeller.

2) Test-bed development [64, 65]: In order to provide a flexible hardware environment for testing and validation of control algorithms for electric propulsion systems with HESS, the Advanced Electric Drive with Hybrid Energy Storage test-bed has been constructed in the University of Michigan Power and Energy Lab (MPEL). This state-of-the-art test-bed, which includes a system controller, Li-Ion battery modules, ultra-capacitor modules, a high speed flywheel, permanent magnet motors, induction motors, DC/DC converters, and three-phase inverters, is uniquely designed for HESS development to address the load fluctuation problem in electric ship propulsion systems. The test-bed will be used to implement and validate the proposed control approaches.

3) Evaluation of energy storage configurations [53, 66]: Since there is no literature to report the effectiveness of HESS in addressing the multi-frequency propulsion-load fluctuation problem for all-electric ships, we first explore the HESS solution as a buffer to isolate the load fluctuations from the shipboard power network. Two different HESS configurations, namely battery combined with UC and battery combined with flywheel, are studied. We first quantitatively analyze the performance of these two configurations and provide insights into the advantages and limitations of each configuration. The battery usage, loss analysis, and sensitivity to battery aging of these two configurations are also analyzed.

4) Control development and performance evaluation of HESS [51, 52, 66, 67]: In order to enable real-time applications and achieve desired performance, a model

predictive control (MPC) strategy is developed. In this MPC formulation, a state of charge (SOC) reference is used to address the limitations imposed by short predictive horizons. Furthermore, because of the multi-frequency characteristics of load fluctuations, a filter-based control strategy is investigated to illustrate the importance of coordination. Without proper control strategies, the HESS solution could be worse than a single ESD solution. The proposed MPC and filter-based control strategies are implemented on the physical testbed. The experimental results demonstrate the effectiveness of the proposed MPC strategy.

5) Development of energy management strategy [54, 55]: When the HESS is introduced into the existing system, there are two potential configurations: a 'plug-in configuration' and an 'integrated configuration'. For 'plug-in' configuration, a novel energy management strategy is developed to avoid undesirable interactions between multiple energy sources. Compared to conventional strategies, the comparison study demonstrates the effectiveness of the proposed energy management strategy. For 'integrated configuration', an integrated energy management strategy is developed to fully coordinate generator sets, HESS, and motor drive. A cost function is formulated to achieve desirable performance in terms of improved efficiency, enhanced reliability, and reduced mechanical wear and tear.

6) Estimation and prediction of propulsion-load torque [68]: The propulsion-load torque is not measurable in most marine applications. To address this issue, we develop a model-based approach to estimate the propulsion-load torque for all-electric ships. Due to the complexity of the propulsion-load torque model, we first develop a simplified model which is able to capture the key dynamics, including both high- and low-frequency load fluctuations. Because of uncer-

tainties in the model parameters, adaptive load estimation is used, leading to improved control performance. This model-based approach can be easily integrated with the MPC to formulate an adaptive load estimation/prediction with MPC (AMPC).

Most of the results outlined above have been documented and published in archived journals and/or referred conference proceedings [51, 52, 53, 54, 55, 63, 64, 69]. Other results are under reviewed or preparation for archived journals [65, 66, 67, 68].

1.4 Outline

The dissertation is organized as follows:

In Chapter II, control-oriented models are presented for all-electric ships with hybrid energy storage. These models include the propeller and ship dynamic model, hybrid energy storage models, the diesel engine and generator set model, electrical motor models and the DC bus dynamic model.

Chapter III presents the development of the Advanced Electric Drive with Hybrid Energy Storage test-bed for electric ship propulsion systems at the University of Michigan Power and Energy Lab. To address load fluctuations in electrical propulsion systems, this test-bed is developed to validate modeling and control solutions. Experimental test results, which demonstrate the energy cycling capability of the test-bed to mitigate the impact of load fluctuations on the bus, are documented in this chapter.

Chapter IV evaluates different HESS configurations and provides the insights into the advantages and limitations of each HESS configuration. Two main objectives are power-fluctuation compensation and HESS loss minimization. Since these objectives conflict with each other in the sense that effective compensation of fluctuations will lead to HESS losses, the weighted-sum method is used to convert this multi-objective

optimization problem (MOP) into a single-objective problem. Global optimal solutions are obtained using dynamic programming (DP) by exploiting the periodicity of the load. These global optimal solutions form the basis of a comparative study of B/FW and B/UC HESS, where the Pareto fronts of these two technologies at different sea state (SS) conditions are derived. The analysis aims to provide insights into the advantages and limitations of the B/FW and B/UC HESS solutions. To enable real-time application and achieve desired performance, a model predictive control (MPC) strategy is developed. In this MPC formulation, a state of charge (SOC) reference is used to address the limitations imposed by short predictive horizons.

Chapter V evaluates the control strategies of HESS. Since the effectiveness of HESS highly depends on its control strategies, two strategies for real-time energy management of HESS are analyzed in this chapter. The first one splits the power demand such that high- and low-frequency power fluctuations are compensated by fast- and slow-dynamic energy storage devices, respectively; the second considers the HESS as a single entity and coordinates the operations of the hybrid energy storage system. Results show that the coordination within HESS provides substantial benefits in terms of reducing power fluctuation and losses. The battery/ultra-capacitors (B/UC) configuration is used to elucidate the control implications in this chapter.

Chapter VI introduces two approaches to integrate the new HESS with an existing propulsion system: the first one is defined as a 'plug-in approach', i.e., the new HESS controller does not change the existing propulsion system; the other one is defined as an 'integrated approach', in which a new integrated controller is developed for the HESS and propulsion system. For the plug-in approach, the interaction analysis of different control strategies is performed. The integrated approach takes advantage of the predictive nature of MPC and allows the designers to judiciously coordinate the different entities of the shipboard network under constraints, thereby providing benefits to system performance.

In Chapter VII, load torque estimation and prediction for implementing MPC-based energy management strategies is addressed. An AMPC approach is developed to estimate the unknown parameters in the propulsion-load model. Due to the complexity of the propulsion-load torque model, a simplified model is developed for the proposed AMPC to capture the key dynamics. In order to evaluate the proposed AMPC approach, an alternative approach is developed where an input observer (IO) is used to estimate the propeller-load torque, and a linear prediction is combined with the IO to predict the future load torque. A comparative study is performed to evaluate the effectiveness of the proposed AMPC, in terms of minimizing the bus voltage variation, regulating the rotational speed, and reducing the high-frequency motor torque variations. The implications of accurate estimation and prediction are also illustrated and analyzed in this study.

In Chapter VIII, real-time MPC is implemented on an AED-HES testbed. In order to achieve real-time feasibility, three different efforts have been made: properly formulating the optimization problem, identifying efficient optimization algorithm, and exploiting a multi-core system controller. First, a problem formulation of the proposed CC-MPC is crafted to achieve the desired performance with a relatively short predictive horizon. Then, an integrated perturbation analysis and sequential quadratic programming (IPA-SQP) algorithm is developed to solve the optimization problem with high computational efficiency. Finally, a multi-core code structure is developed for the real-time system controller to guarantee system signal synchronization and to separate system-level and component-level controls, thereby increasing the real-time capability. Compared with the filter-based control strategy, the improvements provided by the proposed real-time MPC demonstrated on the testbed can be over 50% in terms of reduced bus voltage variations, reduced battery peak and RMS currents, and reduced HESS losses. Furthermore, given the uncertainties presented in any testbed, the experimental results also demonstrate the robustness of

the real-time MPC.

Chapter IX provides conclusions and presents future research directions.

CHAPTER II

Dynamic Model of An Electric Ship Propulsion System with Hybrid Energy Storage

The schematic of the electric propulsion system under investigation is shown in Figure 2.1. The system consists of a prime mover and a generator (PM/G) for power generation, an electric motor for propulsion, the ship and its propeller, and a hybrid energy storage system (HESS). Note that the battery/ultra-capacitor HESS is used as an example in Figure 2.1. Power converters (i.e., DC/DC and AC/DC converters) are used to connect electrical components. The modeling of each component is described in this chapter and the resulting control-oriented models are presented.

2.1 Propeller and Ship Dynamic Model

The focus of the propeller and ship dynamic model is to capture the dynamic behavior of the propeller and ship motion, including the power and torque fluctuations induced on the motor drive shaft. The characteristics of the propeller, subject to the wake field and in-and-out-of-water effects, are investigated and simulation results are presented. As shown in Figure 2.2, the ship dynamics, propeller characteristics, and motor dynamics are mechanically coupled; they influence each other through mechanical connections and internal feedback [63].

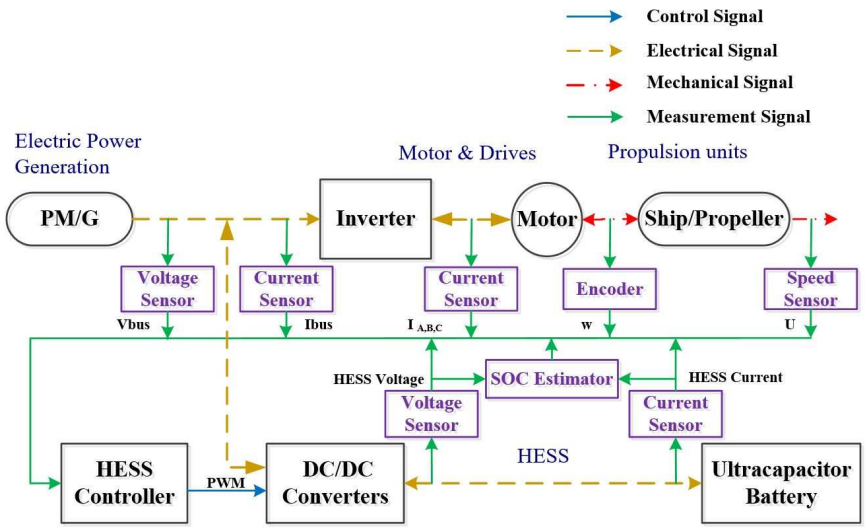

Figure 2.1: Model structure of the electric ship propulsion system with HESS.

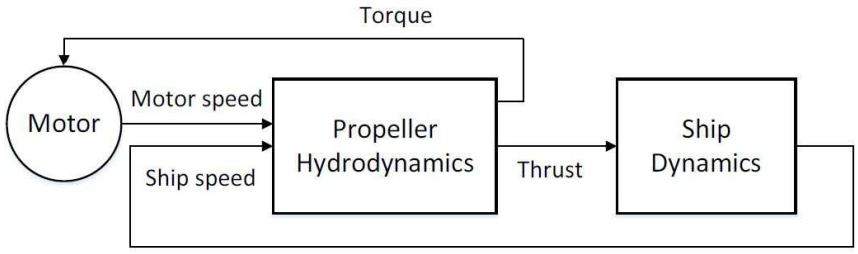

Figure 2.2: Propeller and ship dynamics model structure.

2.1.1 Propeller Characteristics

The propeller responses, in terms of thrust T and torque Q, are nonlinear functions of propeller rotational speed n (in rps), ship speed U, and propeller parameters (e.g. pitch ratio, propeller diameter, loss factor). In this work, we assume that the propeller speed n is kept at the nominal set point and address the load power fluctuation problem by integrating an HESS system and developing an optimized control solution to manage the power.

The thrust, torque, and power can be expressed as:

$$T = \text{sgn}(n)\beta\rho n^2 D^4 f_{K_T}\left(J_A, Pitch/D, A_e/A_o, Z, R_n\right), \tag{2.1}$$

$$Q = \text{sgn}(n)\beta\rho n^2 D^5 f_{K_Q}\left(J_A, Pitch/D, A_e/A_o, Z, R_n\right), \tag{2.2}$$

$$P = 2\pi\,\text{sgn}(n)\beta\rho n^3 D^5 f_{K_Q}\left(J_A, Pitch/D, A_e/A_o, Z, R_n\right), \tag{2.3}$$

where β is the loss factor, ρ is the density of water, D is the diameter of the propeller, and f_{K_T} and f_{K_Q} are the functions of thrust and torque coefficients, respectively [70]-[71].

In f_{K_T} and f_{K_Q}, J_A is the advance coefficient, $Pitch/D$ is the pitch ratio, A_e/A_0 is the expanded blade-area ratio, with A_e being the expanded blade area and A_0 being the swept area, Z is the number of propeller blades, and R_n is the Reynolds number. The parameters of the propeller used in this dissertation are listed in Table 2.1.

The loss factor β is used to account for the torque and thrust reduction experienced by the propeller when it goes in-and-out-of-water.

In our case, we assume $\beta_T = \beta_Q = \beta$, and the dynamic effects of ventilation and lift hysteresis are neglected. The effects of propeller in-and-out-of-water motion and the sensitivity to submergence, however, will be captured in the loss factor using the following expression, originally given in [21]:

$$\beta = \begin{cases} 0, & h/D \leq -0.24; \\ 1 - 0.675(1 - 1.538h/D)^{1.258}, & -0.24 < h/D < 0.65; \\ 1, & h/D \geq 0.65; \end{cases} \tag{2.4}$$

where h is the propeller shaft submergence. A positive value of h means that the propeller stays in the water, and a negative value means the propeller is out of the water.

To complete the propeller model, one needs to know V_a, the advance speed, in order to calculate the advance coefficient $J_A = \frac{V_a}{nD}$. Note that the wake field, defined

as $w = \frac{U-V_a}{U}$, should be taken into account. The wake field model is taken from [25], which includes the average and fluctuation components. In this model, we assume that the fluctuation component consists of 5 terms which are harmonic to the fundamental $\cos(\theta)$, given as follows:

$$\begin{aligned} w = \frac{1}{Z}\sum_{i=0}^{Z-1}[0.2 + 0.12cos(\theta - \frac{i}{2}\pi) \\ + 0.15cos(2\theta - \frac{2i}{2}\pi) + 0.028cos(3\theta - \frac{3i}{2}\pi) \\ + 0.035cos(4\theta - \frac{4i}{2}\pi) - 0.025cos(5\theta - \frac{5i}{2}\pi)], \end{aligned} \tag{2.5}$$

where $\theta \in [0, 2\pi]$ is the angular position of a single blade. The parameters in equation (2.5) are estimated from [25]. The fluctuation component of the wake field is related to the blade motion, which causes the high-frequency fluctuations on the shipboard network.

Remark 2.1: The resulting fluctuations on the power bus will largely depend on the motor control strategy used. If the rotation speed and the parameters of the propeller are constant, the thrust, torque, and power will depend on the ship speed U, loss factor β, and wake field w. The wake field oscillation in w results in high-frequency fluctuations, and the wave effect leads to low-frequency fluctuations through the ship speed U.

2.1.2 Ship Dynamics

The ship dynamics encompass the response of the ship speed to different forcing functions, including those from the propulsion system, wave excitations, wind, and hydrodynamic resistance from water, as well as from the environment:

$$(m + m_x) \times \frac{dU}{dt} = T(1 - t_d) + R_{ship} + F, \tag{2.6}$$

where m is the mass of the ship, m_x is the added-mass of the ship, t_d is the thrust deduction coefficient, which represents the thrust loss due to the hull resistance, F is wave disturbances, R_{ship} is the total resistance including frictional resistance R_F, wave-making resistance R_R, wind resistance R_{wind} [25, 72]:

$$R_{ship} = R_F + R_R + R_{wind}, \tag{2.7}$$

where

$$\begin{cases} R_F = \frac{1}{2} C_F \rho U^2 S, \\ R_R = \frac{1}{2} C_R \rho U^2 S, \\ R_{wind} = \frac{1}{2} C_{air} \rho U^2 A_T. \end{cases} \tag{2.8}$$

In equation (2.8) S is the wetted area of the ship, and A_T is the advance facing area in the air. Parameters C_F, C_R, and C_{air} are the drag coefficients for the water-ship friction, wave-making, and wind resistance, respectively, and they are assumed to be constant.

In equation (2.6), the average ship speed is determined by $T(1 - t_d) + R_{ship}$, and the oscillation of ship speed is primarily caused by the wave excitation term F [73, 74]. In our work, the first-order wave excitation is considered, while the second-order drift force due to waves is ignored. The first-order wave excitation has little effect on the average speed of the ship motion, but it will introduce fluctuating components to the ship motion, which is essential to our model. The second-order wave force can add resistance to the ship; however, the force is very small in low sea state, and neglecting its effects will not change the nature of the problem in our study. The regular wave model is used here to demonstrate the effectiveness of the proposed method. Irregular wave models could represent more realistic sea conditions, and will be investigated in future work.

The model structure and dynamic equations presented in this chapter are rather

Table 2.1: Ship parameters

Description	Parameter	Value
Ship length	L_{ship}	$190m$
Ship breadth	B_{ship}	$28.4m$
Ship draft	H	$15.8m$
Ship Mass	m	$20000ton$
Added-mass	m_x	$28755ton$
Propeller diameter	D	$5.6m$
Number of propeller blades	Z	4
Propeller pitch ratio	$Pitch/D$	0.702
Expanded blade-area ratio	A_e/A_o	0.5445
Reynolds number	R_n	2×10^6
Thrust deduction coefficient	t_d	0.2
Wetted area	S	$12297m^2$
Advance facing area in the air	A_T	$675.2m^2$
Water resistance coefficients	$C_F + C_R$	0.0043
Air resistance coefficient	C_{air}	0.8

generic. For this study, however, we use an electric cargo ship as the example, whose design is documented in detail in [75], and whose key parameters are shown in Table 2.1.

For this ship and propeller combination, large fluctuations are observed in the power and thrust due to propeller rotational motion and regular wave encounters. Particularly in rough sea conditions (e.g., sea state 6), the propeller will be in-and-out-of-water, causing large and asymmetric fluctuations. A sample result of the model response, in both the time domain and frequency domain, is shown in Figure 2.3, where the torque and power responses of the model in two sea states (sea state 4 and sea state 6) are shown side-by-side. The propeller and ship dynamic model is used to capture the power load fluctuations in the propulsion system, and provides the power demand (P_{FL}) for the HESS. In Chapters IV - VI, the load fluctuations are assumed to be known. In Chapter VII, a more realistic case is taken into consideration, where the load fluctuations are unknown and the parameters of the model presented above have uncertainties.

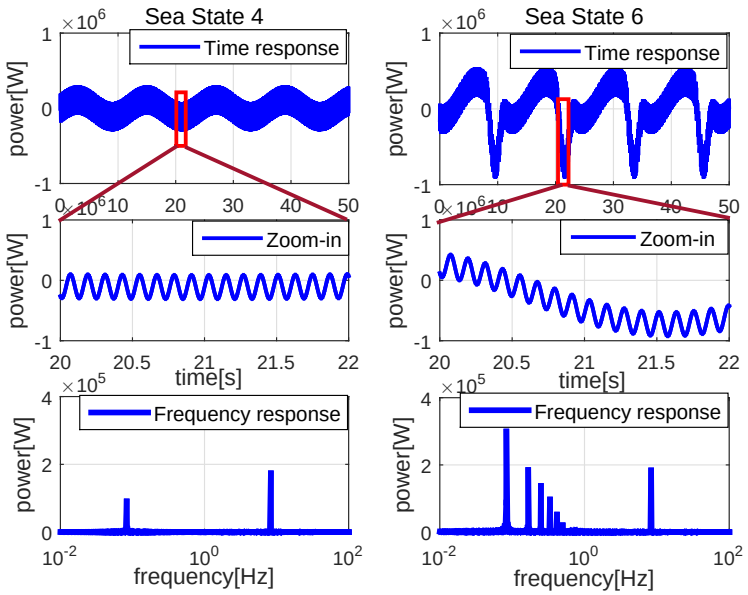

Figure 2.3: Load power fluctuations (top plots), zoomed-in fluctuations (middle plots), and their frequency spectrums (bottom plots).

2.2 Hybrid Energy Storage System Model

Batteries, ultra-capacitors (UCs), and flywheels are energy storage systems with different characteristics in terms of their energy and power densities: batteries provide high energy density, while UCs have high power density; flywheels offer an intermediate solution. An HESS can therefore combine their complementary features and offer superior power and energy density over a single type of energy storage. Furthermore, UCs or flywheels allow the battery to reduce its high power operation and thus extend its life.

For the HESS model, we define the states as the state of charge (SOC) of the battery, UC and flywheel, and the control variables as the battery and UC currents

(I_B and I_{UC}) and flywheel torque (T_{FW}):

$$x = \begin{bmatrix} x_B \\ x_{UC} \\ x_{FW} \end{bmatrix} = \begin{bmatrix} SOC_B \\ SOC_{UC} \\ SOC_{FW} \end{bmatrix}, \; u = \begin{bmatrix} u_B \\ u_{UC} \\ u_{FW} \end{bmatrix} = \begin{bmatrix} I_B \\ I_{UC} \\ T_{FW} \end{bmatrix}. \tag{2.9}$$

The SOC of the battery is defined as the electric charge available relative to the maximum capacity, namely $SOC_B = \frac{Q_{battery}}{Q_B} \times 100\%$, where $Q_{battery}$ and Q_B in amp-hours(Ah) are the current and maximum capacity of the battery, respectively. The SOC of the ultra-capacitor is defined as $SOC_{UC} = \frac{V_{UC}}{V_{max}} \times 100\%$, where V_{UC} and V_{max} are the voltage and maximum voltage of the ultra-capacitors. The SOC of the flywheel is defined in terms of its rotational speed [39], namely $SOC_{FW} = \frac{\omega}{\omega_{max}} \times 100\%$, where ω and ω_{max} are the flywheel current and maximum speed, respectively. The HESS model is described as follows:

$$\begin{aligned} \dot{x}_B =& \frac{-u_B}{3600 Q_B}, \\ \dot{x}_{UC} =& \frac{-u_{UC}}{V_{max} C_{UC}}, \\ \dot{x}_{FW} =& \frac{-b}{\omega_{max} J_{FW}} x_{FW} - \frac{u_{FW}}{\omega_{max} J_{FW}}, \end{aligned} \tag{2.10}$$

where C_{UC} is the capacitance of the ultra-capacitor, and b and J_{FW} are the friction coefficient and inertia of the flywheel. Note that using battery and UC currents and flywheel torque as the control variables allows us to derive a linear model for HESS in the form of (2.10). The terminal power of these ESDs are obtained as follows:

$$\begin{aligned} P_B =& N_B \times (V_{OC} u_B - R_B u_B^2), \\ P_{UC} =& N_{UC} \times (V_{max} x_{UC} u_{UC} - R_{UC} u_{UC}^2), \\ P_{FW} =& N_{FW} \times \left[\omega_{max} x_{FW} u_{FW} - \frac{3}{2} R_s \left(\frac{u_{FW}}{\frac{3}{4} p_{PM} \Lambda_{FW}} \right)^2 - b(\omega_{max} x_{FW})^2 \right], \end{aligned} \tag{2.11}$$

Table 2.2: Hybrid energy storage parameters.

Description	Parameter	Value
Open-circuit voltage of one battery module	V_{OC}	$128V$
Internal resistance of one battery module	R_B	$64m\Omega$
Maximum speed of one FW module	ω_{max}	$36750rmp$
Stator resistance of one FW module	R_s	$6m\Omega$
Inertia of one FW module	J_{FW}	$0.6546kgm^2$
Capacitance of one UC module	C_{UC}	$63F$
Maximum voltage of one UC module	V_{max}	$125V$
Internal resistance of one UC module	R_{UC}	$8.6m\Omega$

where N_B, N_{FW} and N_{UC} are the numbers of battery, flywheel and ultra-capacitor modules, respectively; V_{OC} and R_B are the open-circuit voltage and internal resistance of a battery module; R_s, p_{PM} and Λ_{FW} are the stator resistance, the number of poles and the permanent magnet flux of a flywheel module, respectively; and R_{UC} is the internal resistance of a ultra-capacitor module. The parameters of B/FW and B/UC HESS configurations are shown in Table 2.2. The SOC of the battery is controlled to be within 20%-90%, and the open-circuit voltage is assumed to be constant in this range. For dynamic applications, as the standby losses of the battery [76] and the ultra-capacitor [77] can be ignored, only conductive losses are considered in the battery and ultra-capacitor models. However, the standby loss of the high-speed flywheel, due to the spinning of its rotor, is one of its main losses that cannot be ignored [78]. The conductive losses of the battery, flywheel and ultra-capacitor are $R_B u_B^2$, $\frac{3}{2}R_s\left(\frac{u_{FW}}{\frac{3}{4}p_{PM}\Lambda_{FW}}\right)^2$ and $R_{UC}u_{UC}^2$, respectively, and $b(\omega_{max}x_{FW})^2$ is the spinning loss of the flywheel, including core losses and windage losses.

Sea state 4 is defined as the nominal condition in our design. The HESS sizing in this dissertation is based on an energy and power requirement analysis at sea state 4, shown in Table 2.3, where the maximum absolute power in one cycle, and energy stored or drawn in one half-cycle, are listed. According to this requirement and the frequency characteristics of the load power, the sizes of the energy storage are selected and shown in Table 2.4, where the assumed operating conditions are: $I_B = 150A$, $SOC_B = 80\%$, $SOC_{FW} = 80\%$, $SOC_{UC} = 80\%$, $P_{FW} = 80\% \times P_{FW_{max}}$

Table 2.3: Requirement based on sea state 4

	Low Frequency	High Frequency	Total
Maximum Power	114KW	194KW	308KW
Energy Storage	121Wh	2.05Wh	123Wh

Table 2.4: HESS configuration and size selection.

	B only	UC only	FW only	B/FW	B/UC
N_B	18	0	0	6	6
N_{UC}	0	14	0	0	9
N_{FW}	0	0	5	3	0
Peak Power (KW)	346	336	360	331	331
Energy Storage (KWh)	184.32	1.23	4.31	69.2	62.23
Weight (Kg)	2520	910	1020	1452	1425
Volume (m^3)	1.71	1.14	1.01	1.18	1.3

and $P_{UC} = 80\% \times P_{UC_{max}}$.

2.3 DC Bus Dynamic Model

A simplified representation of the DC bus dynamics is shown in Figure 2.4. Since the currents of HESS are defined as the control variable, the DC bus dynamics based on the current flow is expressed as follows:

$$\dot{x}_{DC} = \dot{V}_{DC} = \frac{I_{in}}{C_{Bus}}, \tag{2.12}$$

where V_{DC} is the DC bus voltage, C_{Bus} is the DC bus capacitance, $I_{in} = (P_{Gen} + P_{HESS} - P_M)/V_{DC}$ is the current flowing into the bus capacitor, P_{Gen} is the electrical output power of the generators, P_{HESS} is the HESS output power, and P_M is the electrical input power of the induction motor.

2.4 Electric Power Generation and Propulsion Motor Model

The electric power generation system includes diesel-generator sets and their associated rectifiers. The diesel engine is used as the prime mover (PM), and is connected

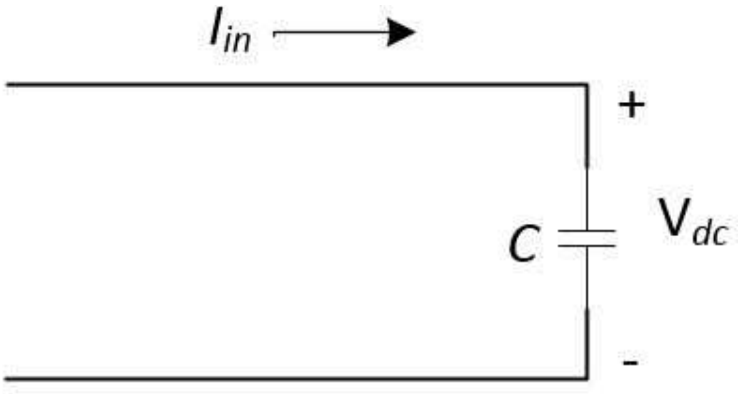

Figure 2.4: DC bus dynamic representation.

to the synchronous field-winding generator to generate AC power. The rectifier converts the AC power into DC power. A speed regulator is used to control the diesel engine so as to keep the generator at the reference speed. A diagram of the electric power generation is shown in Figure 2.5. In order to develop a control-oriented model, a linearized average model of the electric power generation system is developed in this section. The field-winding voltage of the generator is defined as the control variable u_G, and the DC output current of the rectifier is defined as the state variable x_G. The desired DC bus voltage is assumed as the reference value when linearizing the power generation system. As shown in Figure 2.6, the first-order linearized model captures the underlying dynamics of the generator and the rectifier with sufficient accuracy. Therefore, the electric power generation system can be described as:

$$\dot{x}_G = \frac{-1}{\tau_{PG}} x_G + \frac{G_{PG}}{\tau_{PG}} u_G, \tag{2.13}$$

where τ_{PG} and G_{PG} are the time constant and DC gain of the linearized generator set model, respectively.

For the propulsion motor, the control variable u_M is the torque command T_M, and the state variable x_M is the shaft rotational speed ω. The motor shaft dynamics can be described in the following:

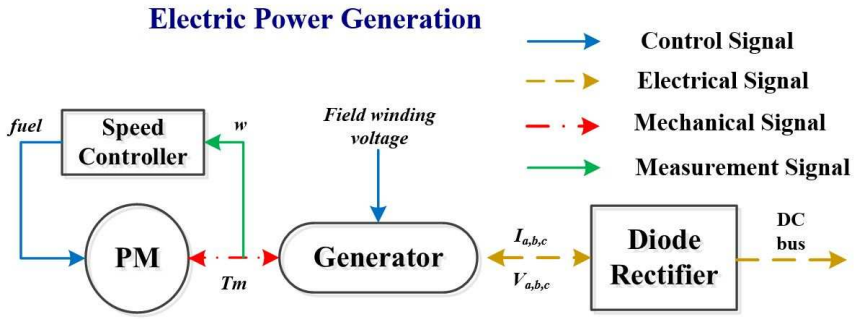

Figure 2.5: Model structure of electric power generation system.

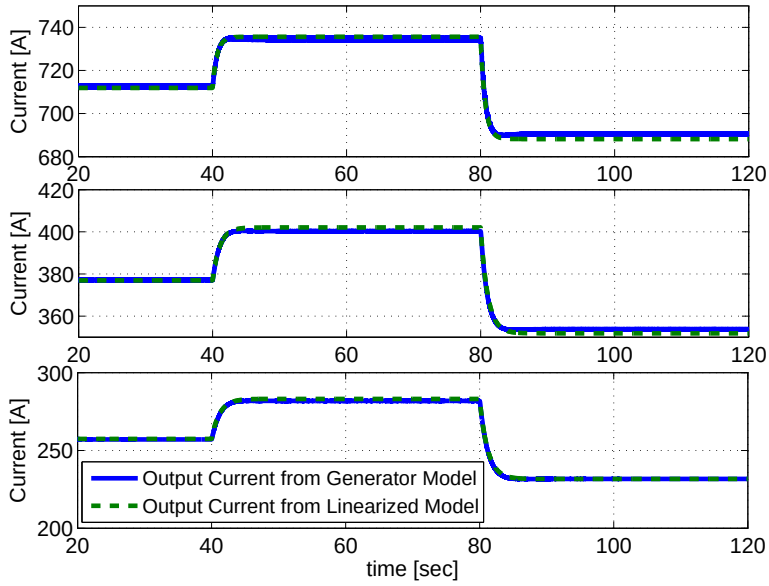

Figure 2.6: Linearized model responses of the generator and the diode rectifier at three different operating points.

$$\dot{x}_M = \frac{-\beta_M}{H} x_M + \frac{1}{H} u_M - \frac{1}{H} T_{Load}, \tag{2.14}$$

where β_M is the viscous damping coefficient of the motor and propeller, H is the total inertia, and T_{Load} is the propulsion load torque.

2.5 Summary

In this chapter, the control- and optimization-oriented models are developed to capture the key dynamics of the shipboard electric propulsion system in order to provide an essential tool for feasibility analysis and system design. The models developed in this dissertation include the propeller and ship dynamic model, hybrid energy storage models, the diesel engine and generator set model, the electrical motor model and the DC bus dynamic model. The propeller and ship dynamic model captures both high- and low-frequency fluctuations on the propeller.

CHAPTER III

A Low-Voltage Test-bed for Electric Ship Propulsion Systems with Hybrid Energy Storage

Electric propulsion systems with HESS are of interest for future ship electrification. In order to experimentally validate power and energy management strategies for electric drive systems with HESS, the Michigan Power and Energy Lab (MPEL) has constructed the Advanced Electric Drive with Hybrid Energy Storage (AED-HES) test-bed, which includes a system-level controller that can simultaneously control all of the power electronic converters interfacing with the HESS and other system components. This chapter presents the development of this test-bed. The preliminary experiments aims to mitigate the effects of power fluctuations on the DC bus. The experimental results demonstrate the capabilities of the MPEL AED-HES test-bed in control implementation and system integration for electric drive systems with HESS.

3.1 MPEL AED-HES Test-bed

In order to provide a flexible hardware environment for the testing and validation of control algorithms for electric propulsion systems with HESS, the Advanced Electric Drive with AED-HES test-bed has been constructed in MPEL. The AED-HES is developed based on the schematic shown in Figure 3.1. Two 3-phase AC power

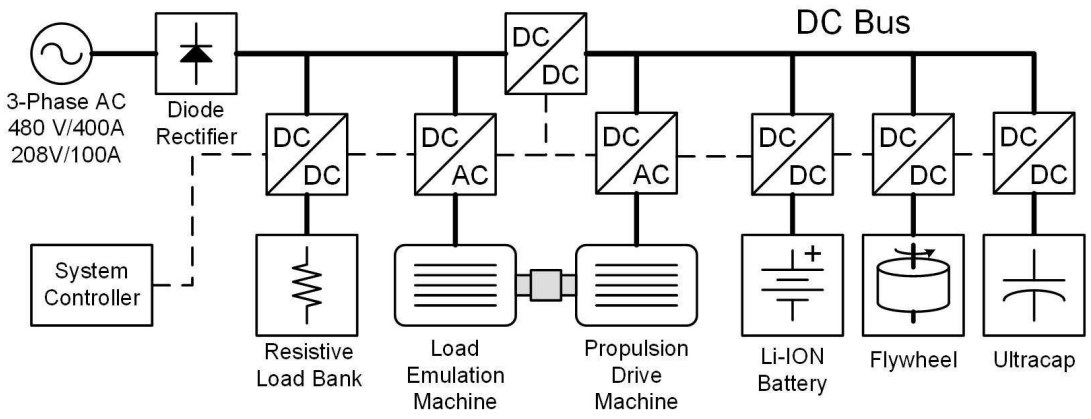

Figure 3.1: Electrical schematic of the MPEL test-bed.

sources (480VAC/400A and 208VAC/100A) are available to be used as the external power source, which is converted by a diode rectifier and a DC/DC converter to provide a DC bus for experiments at various power levels. Two electric machines are connected at the shaft; one corresponds to the propulsion electric machine, and the other represents the propeller load. Li-Ion batteries, ultra-capacitors and a flywheel are integrated with the DC bus using DC/DC converters in order to provide energy cycling to address the load fluctuations in the propulsion system.

The test-bed photo is shown in Figure 3.2. In the test-bed, the power electronic converters, which serve as actuators in directing the power flow to and from various components of the test-bed, are controlled by a central micro-controller. To reduce cost and development time, the test-bed is constructed largely from commercially-available hardware. Currently, a pair of induction machines, as well as a pair of permanent magnet synchronous machines, are available for testing. This configuration allows us to easily mimic realistic load profiles while recycling a large portion of the power absorbed by the load machine. The HESS, integrated via power electronic converters to the DC bus of the test-bed, provide complementary "reservoirs" for energy which may be used to compensate disturbances caused by load fluctuations. My contribution to the test-bed development is the system controller and energy

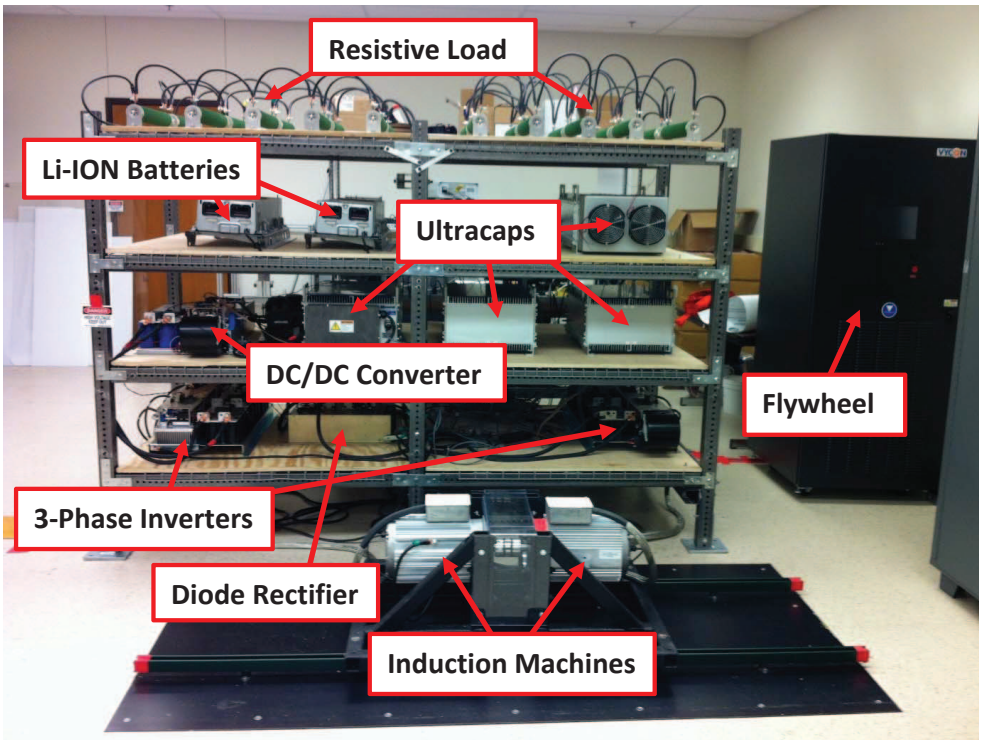

Figure 3.2: MPEL AED-HES test-bed.

storages as well as their DC/DC converters.

3.1.1 System Controller

To enable rapid prototyping of advance control algorithms for electric drives and energy cycling, the AED-HES test-bed utilizes software and hardware solutions from Mathworks® and Speedgoat®. Control algorithms are tested numerically in Matlab/Simulink on models of the system, and then implemented for experimental validation on a Speedgoat® real-time target machine through automatic generation of C-code from Simulink® controller models. Specifications for the Speedgoat® system controller are provided in Table 3.1. Utilizing a single controller for both high- and low-level control not only simplifies the development process, but also helps reduce the effects of noise, as the switching of the power electronic transistors and the sampling of the analog-to-digital converters are synchronized such that sampling occurs in between switching events, avoiding the pick-up of electromagnetic interference.

Table 3.1: Manufacturer specifications for system controller.

System Controller	
Manufacturer:	Speedgoat®
Processor:	Intel Core i5-680 3.6 GHz
Main drive:	320GB SATA Hard Disk
Memory:	DDR3 4096 MB
Serial ports:	4×RS232
Software:	Simulink Real-Time®
PWM outputs:	18
Quadrature decoding inputs:	2
Digital inputs/outputs:	4
Analog-to-digital inputs:	16 in differential mode
Controller area network (CAN):	1
Ethernet communication block:	1

3.1.2 Electric Machines and Power Electronic Inverters

The test-bed consists of two pairs of electric machines, with identical specifications, which are mechanically coupled at the shaft and powered by variable frequency drives utilizing power electronic inverters. The "Propulsion Drive Machine" in Figure 3.1 represents to the ship propulsion drive (electric machine and variable speed drive) depicted in Figure 1.5, while the "Load Emulation Machine" is controlled in a way that mimics the hydrodynamic load fluctuations encountered in the ship propulsion system. Machines are sized for light-duty EV/HEV applications, and their specifications are listed in Table 3.2.

The three-phase power electronic inverters used to drive the electric machines, manufactured by Applied Power Systems® (part no. IAP600T120H-01), utilize paralleled Insulated-Gate Bipolar Transistors (IGBTs) to yield a 600 ampere maximum phase current. The inverters, which use forced-air cooling, accept PWM signals from the centralized controller via fiber-optic cables and provide analog feedback signals

Table 3.2: Manufacturer specifications for electric machines.

PMSM	
Manufacturer:	UQM Technologies®
Rotor Type:	Surface Mount
No. Phases:	3
Max. Cont. Power:	85 kW
Peak Power:	145 kW
Peak Torque:	400 N-m
Max. Speed:	8000 RPM
Peak Efficiency:	94 %
Induction Machine	
Manufacturer:	Azure Dynamics®
Rotor Type:	Squirrel Cage
No. Phases:	3
Max. Cont. Power:	20 kW
Peak Power:	47 kW
Peak Torque:	92 N-m
Max. Speed:	12000 RPM
Peak Efficiency:	87%

for bus voltage, temperature, and phase current measurements, as well as a digital fault-status signal.

3.1.3 Energy Storage

As mentioned earlier, the (hybrid) energy storage available in our test-bed consists of a lithium ion battery pack, an ultra-capacitor bank, and a flywheel, which provide energy cycling capability at various complementary time scales. The battery pack and flywheel are custom solutions, while the ultra-capacitors are commercially available. As depicted in Figure 3.1, each energy storage element interfaces with the DC bus via a DC/DC converter (Buck or Boost converters, as applicable), which control the

flow of power into and out of each element.

3.1.3.1 Flywheel

The flywheel is custom built by Vycon®, as shown in Figure 3.3, to store and supply energy to the power network. Energy is stored mechanically in the inertia of the high-speed flywheel, which is mechanically coupled to an electric machine to convert electrical energy to mechanical energy (i.e., motoring operation) and vice versa (i.e., generating operation). The flywheel unit includes a frictionless magnetic bearing for rotor support, a motor/generator, a high strength steel hub as rotor, and a vacuum containment housing. A long-life rotary-vane oil-filled vacuum pump is used to evacuate the flywheel chamber, virtually eliminating windage losses. The flywheel specifications are listed in Table 3.3.

Table 3.3: Manufacturer specifications for flywheel.

Flywheel	
Manufacturer:	Vycon®
Maximum charge power:	90 kW
Maximum discharge power:	54 kW
Rotational speed:	10000 RPM - 36750 RPM
Hub inertia:	0.618 kgm^2
DC voltage:	400 V-600 V
Efficiency:	99.4% at peak power

3.1.3.2 Battery System

A Lithium-Iron-Phosphate battery chemistry has been selected for its high energy density and superior thermal and chemical stability. The battery system is custom built out of commercially-available components. While the resulting battery system is not as compact as commercial packs for automotive applications, it does have the

Figure 3.3: Flywheel module of MPEL test-bed.

distinct advantage of providing flexibility. Currently, the battery consists of four 36V, 100 Ahr modules, as shown in Figure 3.4, which can be connected in series to provide a pack voltage of up to 144 V. The individual cells have bolted interconnections via copper bus bar, and a Battery Management System (BMS) from Flux Power® utilizes a distributed architecture, where every BMS module manages 4 cells via passive (resistive shunting) cell balancing. The Battery Control Module (BCM) measures battery current to compute the State-Of-Charge (SOC) of the pack in addition to monitoring cell voltages and thermal feedback from the individual BMS's via a CAN-bus network. In the event of a problem (over/under-voltage cell or over-temperature cell), the BCM will open contactor relays to prevent damage to the battery system.

3.1.3.3 Ultra-capacitors

The test-bed has four 63 farad / 125 volt ultra-capacitors from Maxwell Technologies®, as shown in Figure 3.5, which can be connected in series/parallel combinations to suit testing needs. The modules provide analog feedback measurements of temperature

Table 3.4: Specifications for the battery system.

Li-ION Battery	
Manufacturer:	Flux Power®(BMS) & Winston®(cells)
Voltage limits (max/min):	3.9 V/ 2.5 V
Max. continuous current:	3C
Capacity:	100 AHr
DC voltage:	36-144 V (in 36 V increments)
Communication Interface:	CAN bus

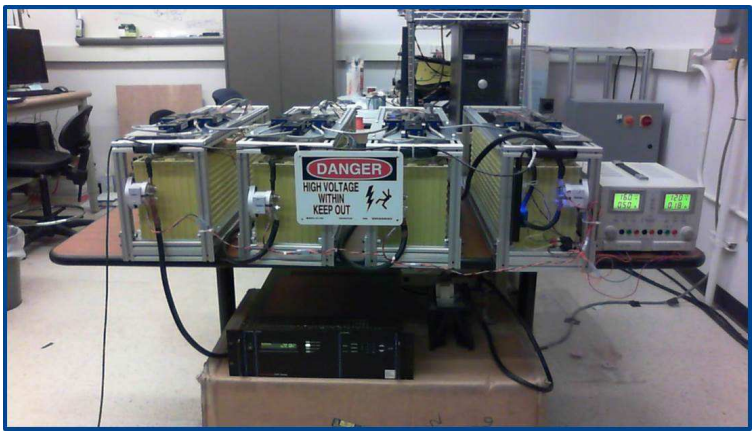

Figure 3.4: Battery module of MPEL test-bed.

and voltage, and interface with the DC bus via a current-regulated power electronic converter. Manufacturer specifications for the ultra-capacitors are provided in Table 3.5.

Table 3.5: Specifications for the ultra-capacitors.

Ultra-capacitor	
Manufacturer:	Maxwell Technologies®
Rated Capacitance:	63 F
Rated Voltage:	125 V
Max. continuous current:	240 A at 40°C
Max. equivalent series resistance:	18 mΩ

Figure 3.5: UC module of MPEL test-bed.

3.2 Energy Cycling Capability of Battery and Ultra-capacitor

In this chapter, two sets of experimental results will be presented. The first experiment demonstrates the energy cycling capabilities when using batteries and ultra-capacitors, and provides experimental validation for baseline control strategies to mitigate multi-frequency load fluctuations. The second experiment shows the energy cycling capability when using the flywheel and ultra-capacitors together in the AED-HES test-bed.

The experimental setup for the first experiment is shown in Figure 3.6. Power from the battery and ultra-capacitor modules is used to isolate the power fluctuations from the DC bus, and the resistive load bank emulates the fluctuating load power, as shown in Figure 3.7. In this experiment, the 480 VAC power source is converted to a 670V DC power source by a three-phase diode rectifier, and then a DC/DC converter is used to buck this voltage down to the desired DC bus voltage of 240V.

The effect of the load fluctuations on the DC bus without regulation is shown in Figure 3.8. Due to the relatively slow dynamic of the battery, the bus voltage regulation using batteries alone is only effective in reducing the low frequency disturbance. In order to eliminate the high frequency disturbance, bus voltage regulation using the ultra-capacitor is introduced to assist the battery modules. To exploit the hybrid configuration of ESDs, two independent voltage regulators using batteries and

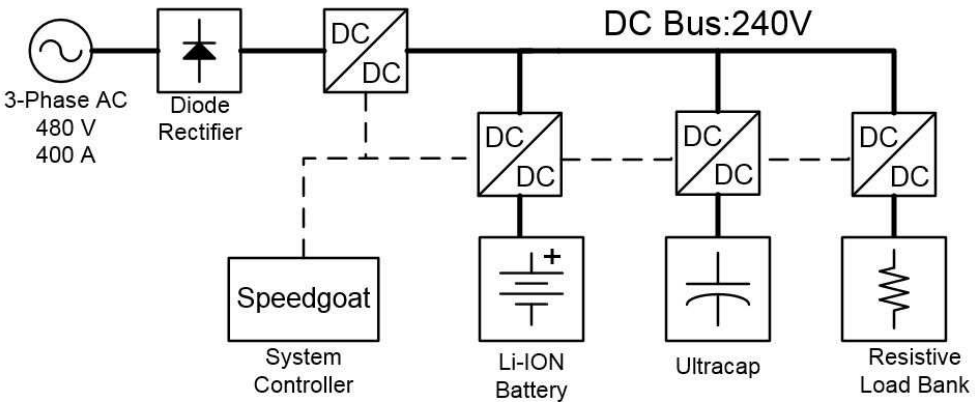

Figure 3.6: Experimental setup for the energy cycling test using batteries and ultra-capacitors.

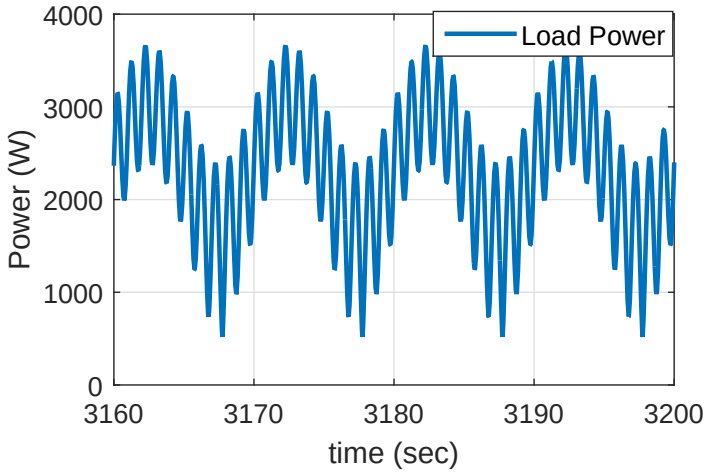

Figure 3.7: Multi-frequency load power fluctuations generated by the resistive load bank.

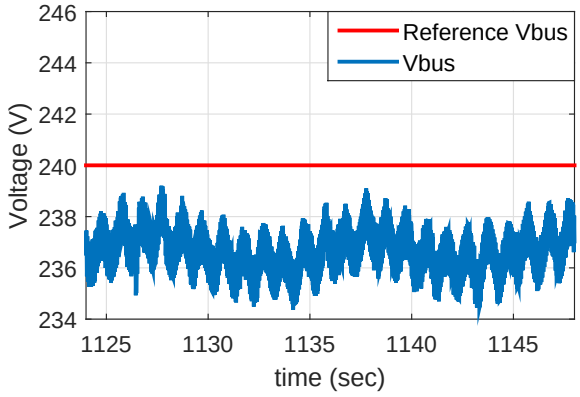

Figure 3.8: DC bus voltage without HESS bus voltage regulators.

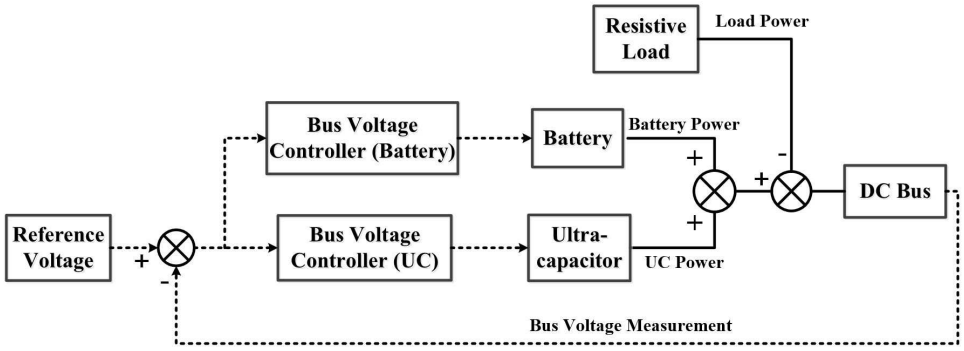

Figure 3.9: Schematic of the independent bus voltage regulation control using batteries and ultra-capacitors.

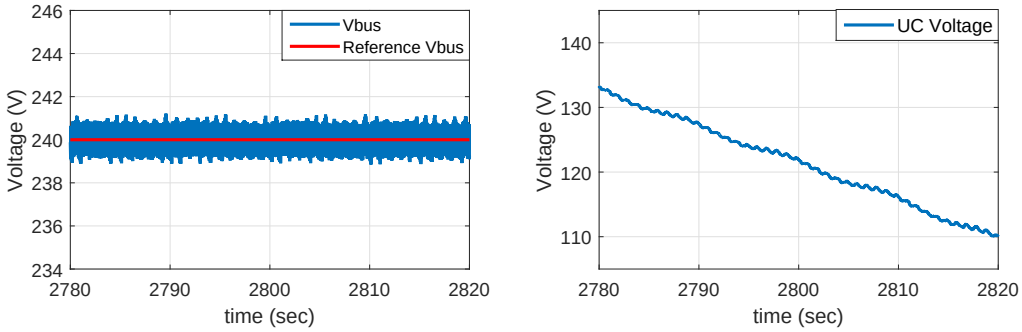

Figure 3.10: DC bus voltage with independent bus voltage regulators using batteries and ultra-capacitors: (a) bus voltage (left) and (b) UC voltage (right).

ultra-capacitors, respectively, are implemented, as shown in Figure 3.9, and the desired DC bus voltage is achieved, as shown in Figure 3.10(a). Note that the solid line represents the electric power and the dashed line represents the control and feedback signals. However, regulating the bus voltage using two independent voltage regulators causes a significant drop in ultra-capacitor voltage (shown in Figure 3.10(b)), leading to large output current and requiring frequent recharging.

A filter-based control strategy is demonstrated in the next experimental test. The schematic of the filter-based control strategy is shown in Figure 3.11, where the battery compensates the low-frequency load fluctuations, and the ultra-capacitor compensates the high-frequency fluctuations. To deal with uncertainties in the load information, a bus voltage regulator is integrated with the feedforward portion of

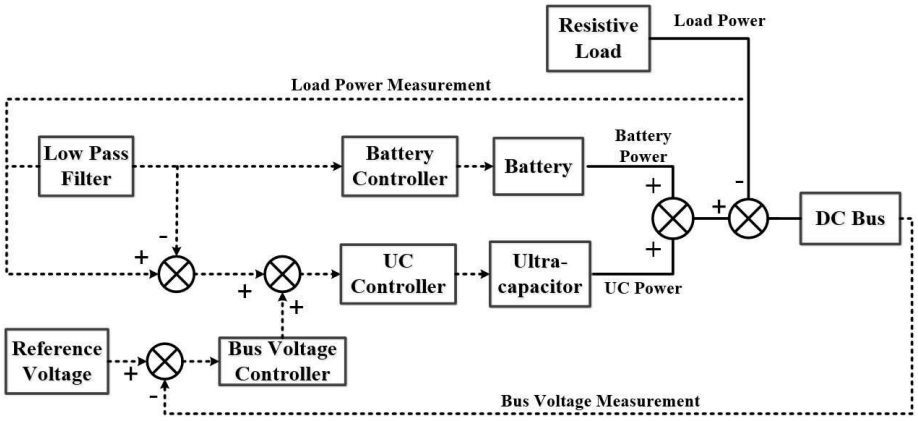

Figure 3.11: Schematic of the filter-based control using batteries and ultra-capacitors.

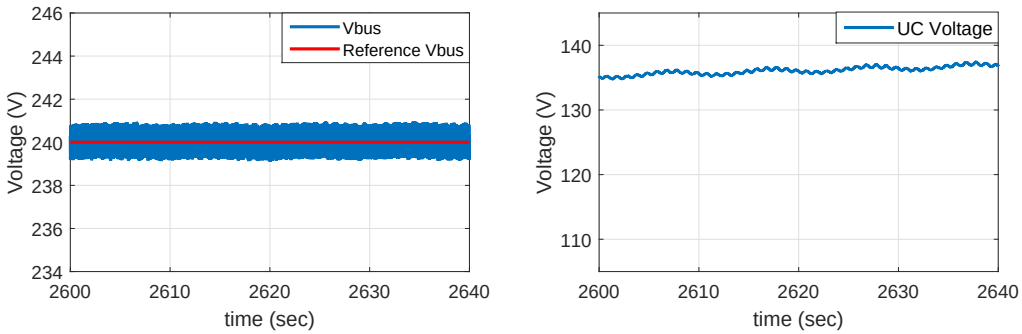

Figure 3.12: DC bus voltage with filter-based control using batteries and ultra-capacitors: (a) bus voltage (left) and (b) UC voltage (right).

the ultra-capacitor controller. The DC bus voltage regulation performance and the ultra-capacitor voltage change are shown in Figure 3.12(a) and (b), respectively. Note that the only load power in this experiment is from the load resistive bank, which represents the load fluctuations. Because the batteries and ultra-capacitors isolate the load fluctuations from the DC bus, the power from the AC power source is almost zero. Furthermore, the ultra-capacitor voltage change is reduced to 1.88V with the filter-based baseline control.

These two baseline control strategies demonstrate the energy cycling capability of the batteries and ultra-capacitors. It is clear from the experimental results for the baseline control strategies that coordinated control strategies are needed to maximize the benefits of using HESS.

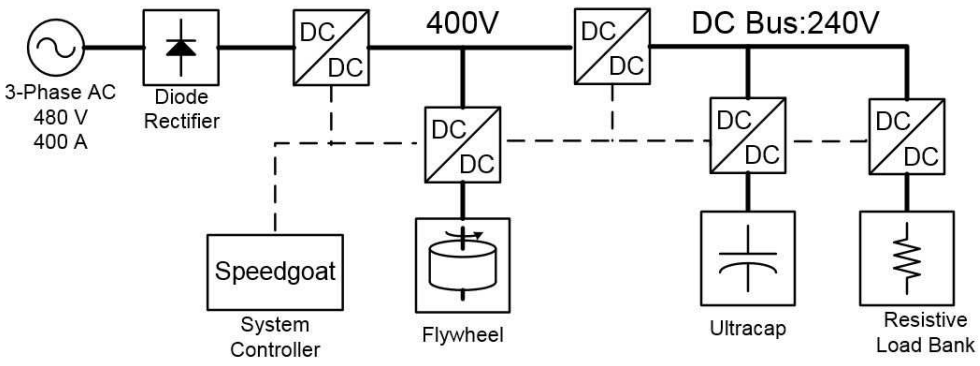

Figure 3.13: Experimental setup for the energy cycling test using the flywheel and ultra-capacitors.

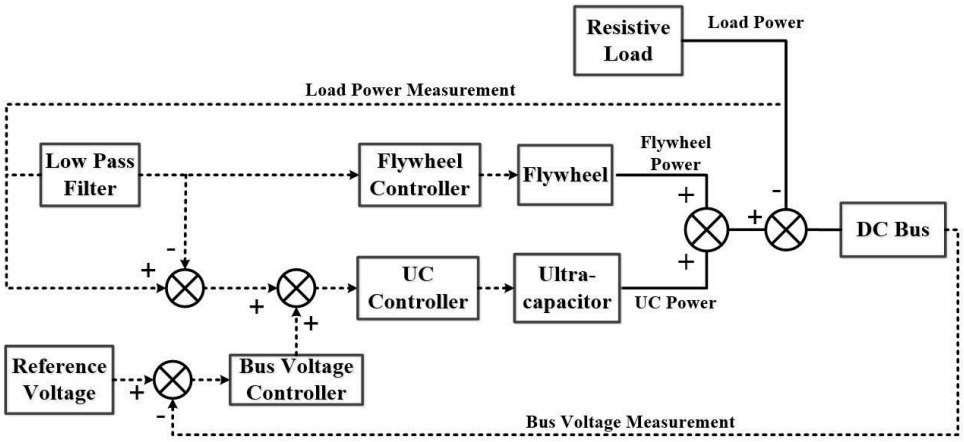

Figure 3.14: Schematic of the filter-based control using the flywheel and ultra-capacitors.

3.3 Energy Cycling Capability of Flywheel and Ultra-capacitor

The energy cycling capability of the HESS configuration consisting of the flywheel and ultra-capacitors is demonstrated in the second experiment, where the flywheel is used to compensate the low-frequency load fluctuations and the ultra-capacitors address the high-frequency fluctuations. In this experiment, the rectified 480 VAC power source is bucked down to 400 V, which is the nominal voltage of the flywheel. The load fluctuation is again generated by the load resistor bank. The corresponding experimental setup developed for this test, and the schematic of the control strategy, are shown in Figures 3.13 and 3.14, respectively. Results are given in Figure 3.15,

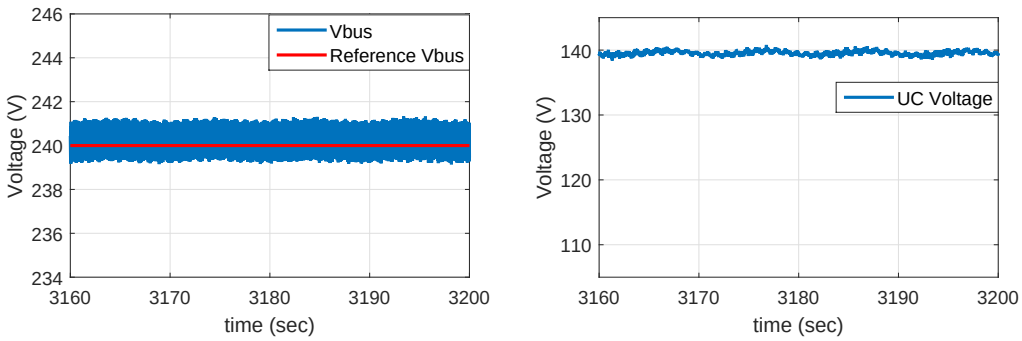

Figure 3.15: DC bus voltage with filter-based control using the flywheel and ultra-capacitors: (a) bus voltage (left) and (b) UC voltage (right).

which demonstrate the effectiveness of the flywheel and ultra-capacitors to compensate the load fluctuations and to regulate the DC bus voltage at the desired value.

These experimental tests not only demonstrate the energy cycling capability of the AED-HES test-bed, but also illustrate the importance of the control strategy.

3.4 Summary

This chapter presents the development and experimental demonstration of the AED-HES test-bed for electric ship propulsion systems at the University of Michigan Power and Energy Lab. A system-level controller, electric machines, high-power converters, and energy storage devices (batteries, UCs, and flywheel) are integrated in the AED-HES test-bed. The AED-HES test-bed facilitates efforts to address load fluctuations in propulsion systems, and can be used as an essential tool to evaluate modeling and control solutions. Two experiments with different energy storage devices are performed to demonstrate the energy cycling capability of AED-HES testbed. The experiential validation of advanced control approaches will be presented in Chapter VIII.

CHAPTER IV

Hybrid Energy Storage Configuration Evaluation: Battery with Flywheel vs. Battery with Ultracapacitor

This chapter investigates the feasibility and effectiveness of introducing a hybrid energy storage system (HESS) to an electric propulsion system for mitigating load power fluctuation effects on a shipboard network. The potential of Battery with Ultracapacitor (B/UC) and Battery with Flywheel (B/FW) HESS in counteracting load fluctuations is formulated as a multi-objective optimization problem (MOP). Two main objectives are power-fluctuation compensation and HESS loss minimization. Since these objectives conflict with each other in the sense that effective compensation of fluctuations will lead to HESS losses, the weighted-sum method is used to convert this MOP into a single-objective problem. Global optimal solutions are obtained using dynamic programming (DP) by exploiting the periodicity of the load. These global optimal solutions form the basis of a comparative study of B/FW and B/UC HESS, where the Pareto fronts of these two technologies at different sea state (SS) conditions are derived. The analysis aims to provide insights into the advantages and limitations of each HESS solution. To enable real-time application and achieve desired performance, a model predictive control (MPC) strategy is developed. In this

MPC formulation, a state of charge (SOC) reference is used to address the limitations imposed by short predictive horizons.

4.1 Performance Evaluation of B/FW And B/UC HESS Configurations

4.1.1 Problem Formulation

In this study, the control strategies of HESS are designed to achieve two objectives: one is to minimize the power tracking error, measured by the root mean square (RMS) error for power fluctuation mitigation, and the other is to reduce HESS losses to improve energy efficiency:

$$J_1 = \sum_{k=0}^{N_T} (P_{FL}(k) - P_{HESS}(k))^2, \tag{4.1}$$

$$J_2 = \sum_{k=0}^{N_T} (P_{HESS_{Loss}}), \tag{4.2}$$

where $N_T = [(t_T - t_0)/T_s]$, with $[\cdot]$ being the integer rounding of $\cdot$, t_0 and t_T are the initial and final values of the time period being investigated, T_s is the sampling time, P_{FL} is the load power fluctuation from the propeller and ship dynamics model, P_{HESS} is the power generated by HESS to compensate the load fluctuations, and $P_{HESS_{Loss}}$ is the HESS losses. Note that the RMS tracking error can be expressed as $\sqrt{J_1/N_T}$. Since N_T is constant, minimizing J_1 is equivalent to minimizing the RMS tracking error.

Because J_1 and J_2 compete in the sense that reducing the tracking error would cause increased HESS losses and vice versa, the weighted-sum method, which converts the multi-objective optimization problem (MOP) to a single-objective optimization problem, is used to find the non-dominated solutions (i.e., Pareto front) in this problem. The problem formulation of B/FW is expressed as follows. Minimize:

$$
\begin{aligned}
&J_{HESS_{B/FW}}(x(k),u(k)) \\
&= \sum_{k=0}^{N_T}(1-\lambda)(P_{FL}(k)-P_B(k)-P_{FW}(k))^2 \\
&\quad + \lambda\left[N_B R_B u_B^2(k) + N_{FW}\left(b(\omega_{max}x_{FW}(k))^2 + \frac{3}{2}R_s\left(\frac{u_{FW}(k)}{\frac{3}{4}p_{PM}\Lambda_{FW}}\right)^2\right)\right],
\end{aligned}
\tag{4.3}
$$

subject to the constraints:

$$
\begin{aligned}
20\% \le x_B \le 90\%, \\
30\% \le x_{FW} \le 99\%, \\
-200A \le u_B \le 200A, \\
-40Nm \le u_{FW} \le 40Nm, \\
-90KW \le u_{FW}x_{FW}\omega_{max} \le 90KW,
\end{aligned}
\tag{4.4}
$$

$$
\begin{aligned}
\begin{bmatrix} x_B(k+1) \\ x_{FW}(k+1) \end{bmatrix} &= \begin{bmatrix} 1 & 0 \\ 0 & 1-\frac{bT_s}{\omega_{max}J_{FW}} \end{bmatrix}\begin{bmatrix} x_B(k) \\ x_{FW}(k) \end{bmatrix} \\
&+ \begin{bmatrix} \frac{T_s}{3600Q_B} & 0 \\ 0 & \frac{T_s}{\omega_{max}J_{FW}} \end{bmatrix}\begin{bmatrix} u_B(k) \\ u_{FW}(k) \end{bmatrix},
\end{aligned}
\tag{4.5}
$$

while the problem formulation for the B/UC HESS is given by:

$$
\begin{aligned}
J_{HESS_{B/UC}}(x(k),u(k)) &= \sum_{k=0}^{N_T}(1-\lambda)(P_{FL}(k)-P_B(k)-P_{UC}(k))^2 \\
&\quad + \lambda(N_B R_B u_B^2(k) + N_{UC}R_{UC}u_{UC}^2(k)),
\end{aligned}
\tag{4.6}
$$

subject to the constraints:

$$\begin{aligned} 20\% \leq x_B \leq 90\%, \\ 30\% \leq x_{UC} \leq 99\%, \\ -200A \leq u_B \leq 200A, \\ -240A \leq u_{UC} \leq 240A, \end{aligned} \tag{4.7}$$

$$\begin{aligned} \begin{bmatrix} x_B(k+1) \\ x_{UC}(k+1) \end{bmatrix} = & \begin{bmatrix} 1 & 0 \\ 0 & 1 \end{bmatrix} \begin{bmatrix} x_B(k) \\ x_{UC}(k) \end{bmatrix} \\ & + \begin{bmatrix} \frac{T_s}{3600 Q_B} & 0 \\ 0 & \frac{T_s}{V_{max} C_{UC}} \end{bmatrix} \begin{bmatrix} u_B(k) \\ u_{UC}(k) \end{bmatrix}, \end{aligned} \tag{4.8}$$

where $\lambda \in [0, 1]$ is a weighting factor that allows us to put different relative emphasis on each attribute to investigate the performance trade-off.

4.1.2 Performance Evaluation

In order to evaluate the feasibility and effectiveness of the B/FW HESS, we perform a comparative study to determine the advantages and disadvantages of B/FW and B/UC HESS configurations. In this case study, the sampling time for the control update is chosen as 0.02 sec, which is properly matched with the underlying system dynamics. We define the time interval that the HESS can be used as the energy buffer for the electric propulsion system without requiring charging or discharging from external power sources (such as the diesel generator) as the self-sustained operation period. A longer self-sustained operation could offer more flexible charging or discharging for the HESS, therefore leading to better efficiency. The self-sustained operation time is chosen to be 30 minutes, over which the resulting performance is evaluated in terms of the following two metrics that are closely related to the aforementioned objectives:

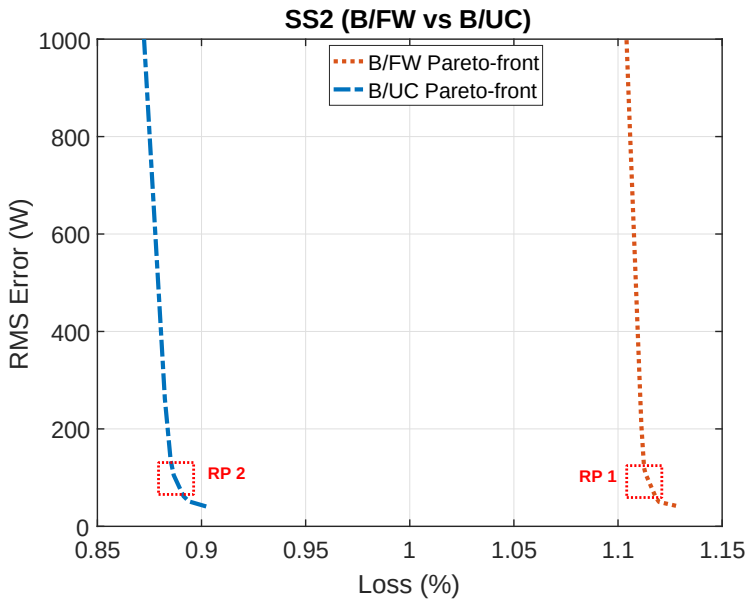

Figure 4.1: Pareto-fronts of B/FW and B/UC HESS at sea state 2.

1. RMS tracking error: $\sqrt{J_1/N_T}$;

2. HESS losses: $Loss\% = \frac{J_2}{\sum_{k=0}^{N_T} P_{Demand}(k)} \times 100\%$.

The weighting factor λ allows us to put a different relative emphasis on each attribute to investigate the performance trade-off. The global optimal solutions of B/FW and B/UC MOPs are obtained by dynamic programming (DP). The Pareto-fronts of these two configurations, which represent the best achievable performance for the system with B/FW HESS and B/UC HESS, are shown in Figures 4.1-4.3. The Pareto fronts provide insight into the effectiveness of HESS and the trade-off between the tracking RMS error and the HESS losses. The key observations are summarized in the following remarks:

Remark 4.1 (Performance trade-off features): The tracking performance can be improved over a wide range at little cost of system efficiency for low and medium sea states (sea states 2 and 4). This feature can be observed for both B/FW and B/UC HESS solutions. Furthermore, the general trends and Pareto front shapes are the same for both HESS configurations at all sea states. In terms of managing the

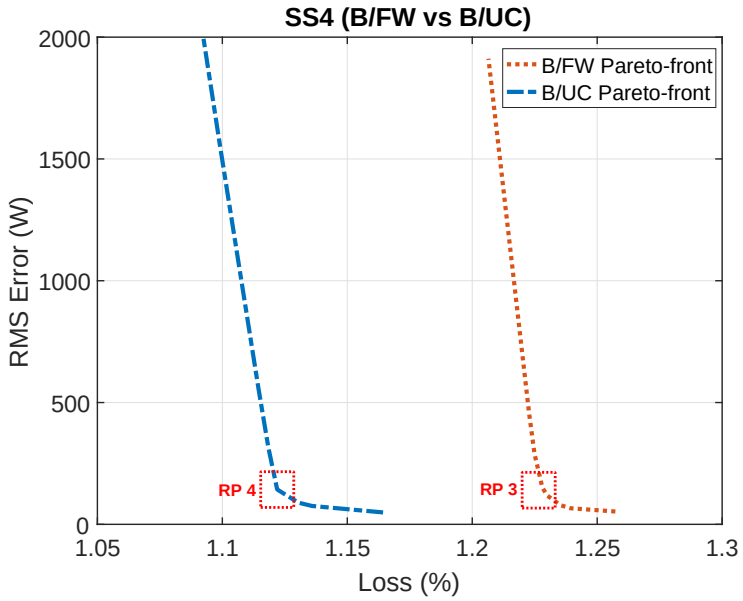

Figure 4.2: Pareto-fronts of B/FW and B/UC HESS at sea state 4.

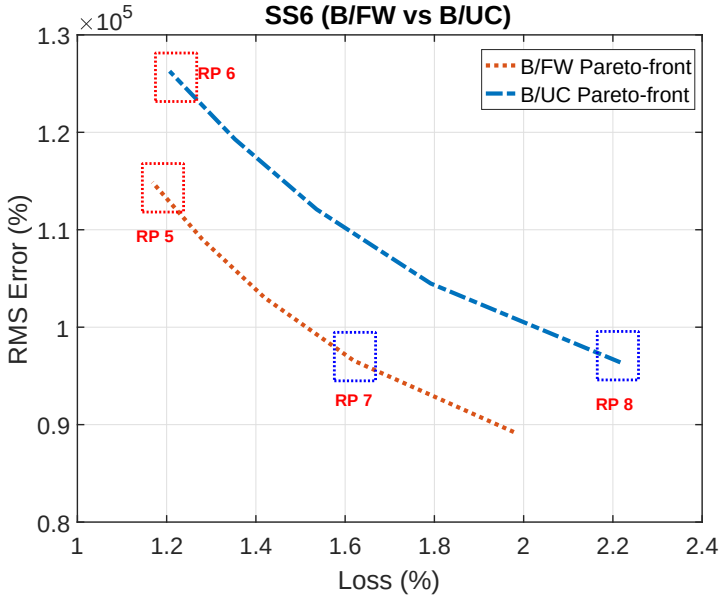

Figure 4.3: Pareto-fronts of B/FW and B/UC HESS at sea state 6.

trade-off, they both have the same features and issues.

Remark 4.2 (B/FW vs. B/UC): As shown in Figures 4.1-4.3, the B/FW HESS is able to achieve superior performance at sea state 6. However, at sea states 2 and 4, the B/UC HESS achieves better performance than B/FW HESS, but the difference between B/FW HESS losses and B/UC HESS losses at sea state 2 (around 0.22%)

is about twice as large as that at sea state 4 (around 0.11%). Note that the load power fluctuations at sea state 2 are smaller than those at sea state 4. The analysis indicates that B/FW HESS is more suitable for the high sea state, while the B/UC HESS has performance advantages at low sea states.

To reveal more details of the HESS performance, several representative points (RP) are highlighted in Figures 4.1-4.3 for further analysis. As shown in Figures 4.1-4.2, those points reflect the best trade-off between two objectives and they are closest to the "utopia" points (J_{1min}, J_{2min}). Therefore, RP1-RP4 are the design points analyzed here. The RMS tracking errors of these design points, i.e., RP1-RP4, are almost the same at the same sea state. RP5-RP8 are the points with comparable performance in one of the attributes at sea state 6. Besides the two main objectives in Figures 4.1-4.3, several other metrics are used for evaluating these solutions as shown in Table 4.1:

Table 4.1: Performance metrics.

$I_{B_{RMS}}$	Battery currents measured by the rms (root mean square) value.
$I_{B_{Peak}}$	Battery currents measured by the maximum absolute value.
$T_{I_{B_{1.5C}}}\%$	The time spent charging/discharging the battery with high currents: the percentage of high current operation ($\lvert I_B \rvert \geq 1.5C$).
$Loss_B\%$	Battery conduction loss: $Loss_B\% = \frac{\sum_{k=0}^{N_T}(Power_{B-loss}(k))}{\sum_{k=0}^{N_T} P_{Demand}(k)} \times 100\%$.
$Loss_{UC}\%$	Ultra-capacitor conduction loss: $Loss_{UC}\% = \frac{\sum_{k=0}^{N_T}(Power_{UC-loss}(k))}{\sum_{k=0}^{N_T} P_{Demand}(k)} \times 100\%$.
$Loss_{FW_{Rs}}\%$	Flywheel conduction loss: $Loss_{FW_{Rs}}\% = \frac{\sum_{k=0}^{N_T}(Power_{FW_{Rs}-loss}(k))}{\sum_{k=0}^{N_T} P_{Demand}(k)} \times 100\%$.
$Loss_{FW_f}\%$	Flywheel spinning loss: $Loss_{FW_f}\% = \frac{\sum_{k=0}^{N_T}(Power_{FW_f-loss}(k))}{\sum_{k=0}^{N_T} P_{Demand}(k)} \times 100\%$.

The metrics $I_{B_{RMS}}$, $I_{B_{Peak}}$ and $I_{B_{1.5C}}\%$ are used to evaluate the battery usage, as they have high impact on the battery life; the power losses of each energy storage as well as the losses due to different mechanisms in the flywheel provide insight into the operation of HESS. The key observations about the reference points are summarized in the following remarks:

Table 4.2: Performance comparison of the selected design points.

	RP1	RP2	RP3	RP4	RP5	RP6	RP7	RP8
Sea State	2	2	4	4	6	6	6	6
$I_{B_{RMS}}$	12.13A	17.33A	16.02A	21.51A	51.59A	55.86A	74.96A	95.62A
$I_{B_{Peak}}$	31.48A	52.85A	72.00A	82.00A	200A	200A	200A	200A
$T_{I_{B_{1.5C}}}$%	0	0	0	0	3.67%	4%	8.50%	19.0%
$Loss_B$%	0.05%	0.09%	0.07%	0.13%	0.39%	0.46%	0.82%	1.34%
$Loss_{UC}$%	NA	0.80%	NA	0.99%	NA	0.75%	NA	0.88%
$Loss_{FW_{R_s}}$%	0.53%	NA	0.48%	NA	0.35%	NA	0.36%	NA
$Loss_{FW_f}$%	0.54%	NA	0.67%	NA	0.43%	NA	0.44%	NA

Remark 4.3 (Battery usage): B/FW HESS is more 'friendly' to batteries with smaller $I_{B_{RMS}}$, $I_{B_{Peak}}$, and less time spent at high-current operation $T_{I_{B_{1.5C}}}$%, as shown in Table 4.2. At sea state 2, $I_{B_{RMS}}$ and $I_{B_{Peak}}$ of the B/UC HESS are almost twice as large as those of B/FW HESS. At sea state 4, the B/FW HESS requires less $I_{B_{RMS}}$ and $I_{B_{Peak}}$ than B/UC to achieve almost the same tracking error. At sea state 6, RP5 and RP6 have almost the same HESS losses, but RP5 (B/FW) achieves much smaller power tracking RMS error. B/FW HESS requires less battery usage and high-current operation, while achieving improved power tracking performance. For RP7 and RP8, the battery high-current operation for B/UC HESS is even more than twice that of the B/FW.

Remark 4.4 (Loss analysis): At sea state 2, even though both the battery RMS and peak current with B/FW are less than those with B/UC, the loss of B/FW is larger than that of B/UC. The reason for this is that the standby loss of the flywheel, namely the spinning loss (including core losses and windage losses), is significant at the low sea state. In particular, the battery needs to discharge more to compensate the spinning losses of the flywheel in order to keep the flywheel working at its optimal speed. Therefore, the drag coefficient is the key design parameter of the flywheel, especially for a high-speed flywheel. At high sea state, the spinning loss of the flywheel is not the main issue of the B/FW HESS configuration. The high power demand of the low-frequency load fluctuation requires the HESS to provide or absorb the maximum power for several seconds. The flywheel working in its high speed range sustains for

a longer period of time to generate or absorb the maximum power when compared to the ultra-capacitor. Therefore, as shown in Table 4.2 and Figure 4.3, B/FW can outperform B/UC in terms of improved tracking performance, reduced HESS losses, and extended battery life cycle. Note that some flywheel motor/generators have much lower spinning core loss (e.g., synchronous reluctance machines), but have lower power density and full-load efficiency.

Remark 4.5 (Sensitivity to battery aging): It has been widely reported that batteries degrade over their life cycle, as the battery capacity will decrease and the battery resistance will increase [79]. A sensitivity study is performed to provide insights into the impact of the battery state of health (SOH) on the proposed HESS solutions. In this study, SOH is characterized by battery capacity reduction and resistance increase. As shown in Figure 4.4, the increased battery resistance has a more significant impact on the proposed solutions compared to the decreased battery capacity. The HESS works as an energy buffer instead of an energy source, as the generator sets provide the average power for the electric propulsion system. Due to the high energy density of the battery, the battery SOC variation within the self-sustained time is very small. Although the degraded capacity can increase the SOC variation, the battery open circuit voltage $V_{OC}(x_1)$ is in general insensitive to this small SOC variation. Therefore, the impact of the decreased capacity is relatively small. The impact of increased battery resistance on the B/UC HESS at sea states 2 and 4 is larger than it is on the B/FW HESS. As discussed in the previous remarks, the spinning losses of the flywheel is dominant in B/FW HESS at low sea state, as shown in Table 4.2, whereas the battery resistance, which affects the battery loss, has less of an effect. However, at high sea state, due to the high-power fluctuations, the battery losses become more significant even in the B/FW configuration. Therefore, the sensitivity to battery resistance is noticeable for both B/FW and B/UC HESS.

The MOP formulated here can be used to evaluate the effectiveness of different HESS configurations and analyze their advantages and limitations. However, the solution of the MOP cannot be used for real-time applications. It is an open-loop optimization without feedback. Furthermore, this optimization problem has a very long horizon in the sense that 90,000 steps are involved when the minimum self-sustained operation time of HESS is chosen to be 30 minutes. This requires a long computational time and large memory, which makes it computationally prohibitive to solve in real time, and leads to the MPC formulation discussed in the next section.

4.2 Receding Horizon Control for Real-Time Power Management

In this section, the receding-horizon approach is applied to develop a real-time energy management scheme. To capture the dynamics of HESS and address the associated operation constraints, MPC emerges as a natural choice. The general MPC problem, which minimizes a cost function subject to constraints within the predictive horizon, can be mathematically expressed as:

$$J = \Phi(x(t+N)) + \sum_{k=t}^{t+N-1} L(x(k), u(k)), \tag{4.9}$$

subject to:

$$x(k+1) = f(x(k), u(k)),\ x(t) = x_0, \tag{4.10}$$

$$C(x(k), u(k)) \leq 0, \tag{4.11}$$

where $\Phi(x(t+N))$ and $L(x(k), u(k))$ are the terminal and instantaneous cost functions, N is the time window over which the cost will be evaluated, $x(k)$ and $u(k)$ are the instantaneous values of the states ($x \in \Re^2$) and controls ($u \in \Re^2$) at time k, respectively, $C(x(k), u(k))$ represents the inequality constraints, and t represents the

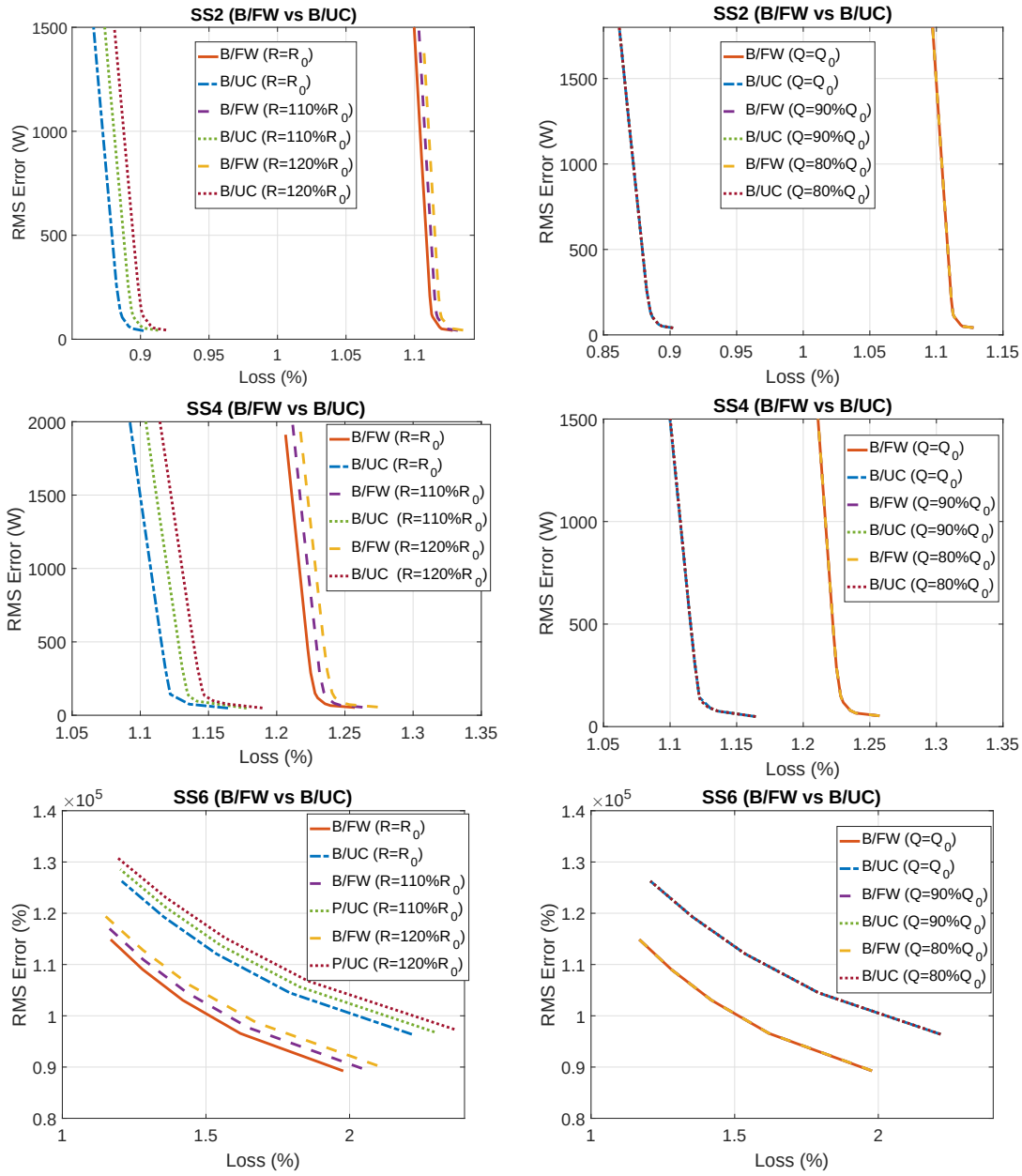

Figure 4.4: Pareto-fronts of B/FW and B/UC HESS at sea states 2,4 and 6 with different battery state of health.

current sample time. By minimizing (4.9) subject to (4.10) and (4.11), an optimized control sequence $u^*(t)$, $u^*(t+1)$, ..., $u^*(t+N-1)$ can be obtained. The standard receding horizon MPC then applies the first element of the sequence as the control action before moving to the next sample, when new measurements are collected and the optimization is repeated with new initial conditions [80]-[81].

The cost function in MPC is formulated based on the MOP by using the weighted-sum method. We discretize the system model developed in Chapter II with sampling time T_s. No terminal cost is incorporated in this MPC formulation. Therefore, the MPC formulation of B/FW is defined as:

$$J_{HESS_{B/FW}} = \sum_{k=t}^{t+N-1} L_{HESS_{B/FW}}(x(k), u(k)), \tag{4.12}$$

where

$$\begin{aligned} & L_{HESS_{B/FW}}(x(k), u(k)) \\ & = (1-\lambda)(P_{FL}(k) - P_B(k) - P_{FW}(k))^2 \\ & + \lambda \left[N_B R_B u_B^2(k) + N_{FW} \left(b(\omega_{max} x_{FW}(k))^2 + \frac{3}{2} R_s \left(\frac{u_{FW}(k)}{\frac{3}{4} p_{PM} \Lambda_{FW}} \right)^2 \right) \right], \end{aligned} \tag{4.13}$$

subject to the constraints (4.4) and (4.5), where $\lambda \in [0, 1]$ is the weighting factor that allows us to put different relative emphasis on each attribute to investigate the performance trade-off.

The short-horizon MPC, however, cannot incorporate the long-term perspectives of operation. As a result, we observed that the SOC of the flywheel drops quickly. As it decreases, delivering the same output power requires larger torque, thereby leading to significantly increased losses and power tracking error, as shown in Figure 4.5.

To keep the flywheel working in a high-efficiency range without having to extend the MPC predictive horizon, we analyzed the DP results to help us find mechanisms to assure long-term system efficiency. The representative point RP3 as shown in Figure 4.2 is used as a benchmark in this section. As shown in Figure 4.6, the B/FW HESS operation can be divided into three phases: transient, sustaining, and final. Given different initial SOCs of the flywheel, it converges to the same SOC range, which is the high-efficiency range for B/FW HESS, during the transient interval. When the B/FW HESS is operating during the sustaining interval, the battery will keep the

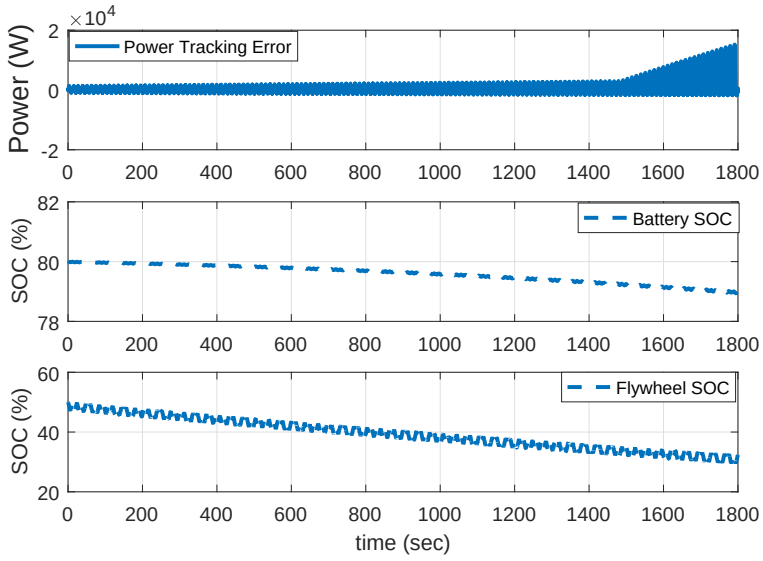

Figure 4.5: B/FW HESS performance at sea state 4 without any penalty on the speed of FW.

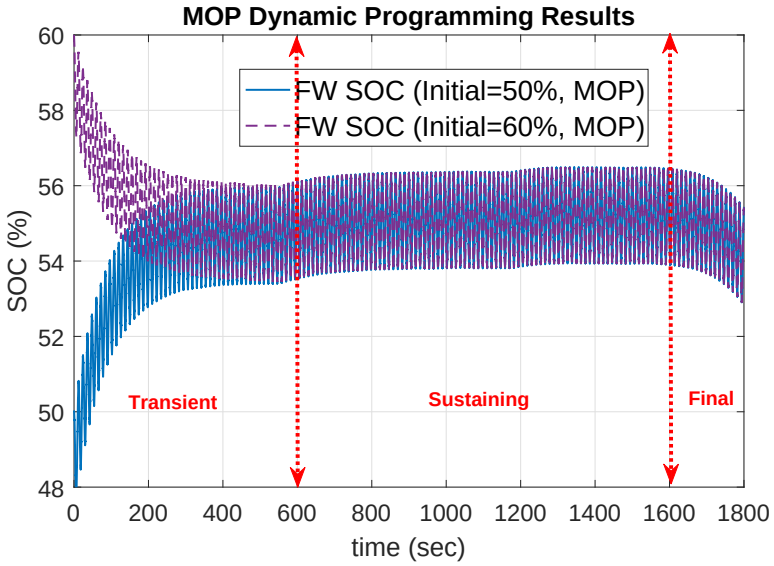

Figure 4.6: The flywheel SOC of MOP dynamic programming solutions with different initial SOCs.

flywheel SOC in its high-efficiency range to minimize the cost in (4.3). During the final interval, the battery is not required to maintain the flywheel SOC, and so the flywheel will be used as much as possible. In order to maximize the benefits of B/FW HESS, a long self-sustained time is preferred, which requires that the flywheel works in its high-efficiency SOC range. This observation motivates us to add another term

into the cost function with a penalty on the SOC deviations from the optimal settings (4.3):

$$\gamma_{FW_{SOC}}(x_{FW}(k) - SOC_{FW_d})^2, \tag{4.14}$$

The cost function used in the MPC optimization formulation then has the form:

$$\begin{aligned}
&L_{HESS_{B/FW}}(x(k), u(k)) \\
&= (1-\lambda)(P_{FL}(k) - P_B(k) - P_{FW}(k))^2 \\
&+ \lambda \left[N_B R_B u_B^2(k) + N_{FW} \left(b(\omega_{max} x_{FW}(k))^2 + \frac{3}{2} R_s \left(\frac{u_{FW}(k)}{\frac{3}{4} p_{PM} \Lambda_{FW}} \right)^2 \right) \right] \\
&+ \gamma_{FW_{SOC}}(x_{FW}(k) - SOC_{FW_d})^2;
\end{aligned} \tag{4.15}$$

Increasing γ initially improves the performance, but further increases in γ beyond a certain value will lead to deteriorated performance. The reason is that, when initially increasing γ, the flywheel can operate around its optimal SOC, leading to improved efficiency. However, if γ is too large, then the flywheel is forced to operate close to its optimal SOC with small variations, which leaves most of the compensation function on the batteries. That makes the HESS function essentially a battery energy storage system, thereby losing the advantage of the hybrid configuration. By varying γ, we are able to obtain the best achievable solution. In this study, γ is tuned off-line. Note that how to obtain the optimal reference SOC is an open question, and will be explored in future work.

The performance of the proposed MPC energy management strategy and DP is shown in Figure 4.7. As shown in the zoom-in plots of Figure 4.7, the flywheel SOC under the proposed MPC can achieve the same trajectory as DP during the sustaining interval. The battery output current and flywheel output torque of MPC and DP are also almost the same, thereby achieving almost equivalent performance.

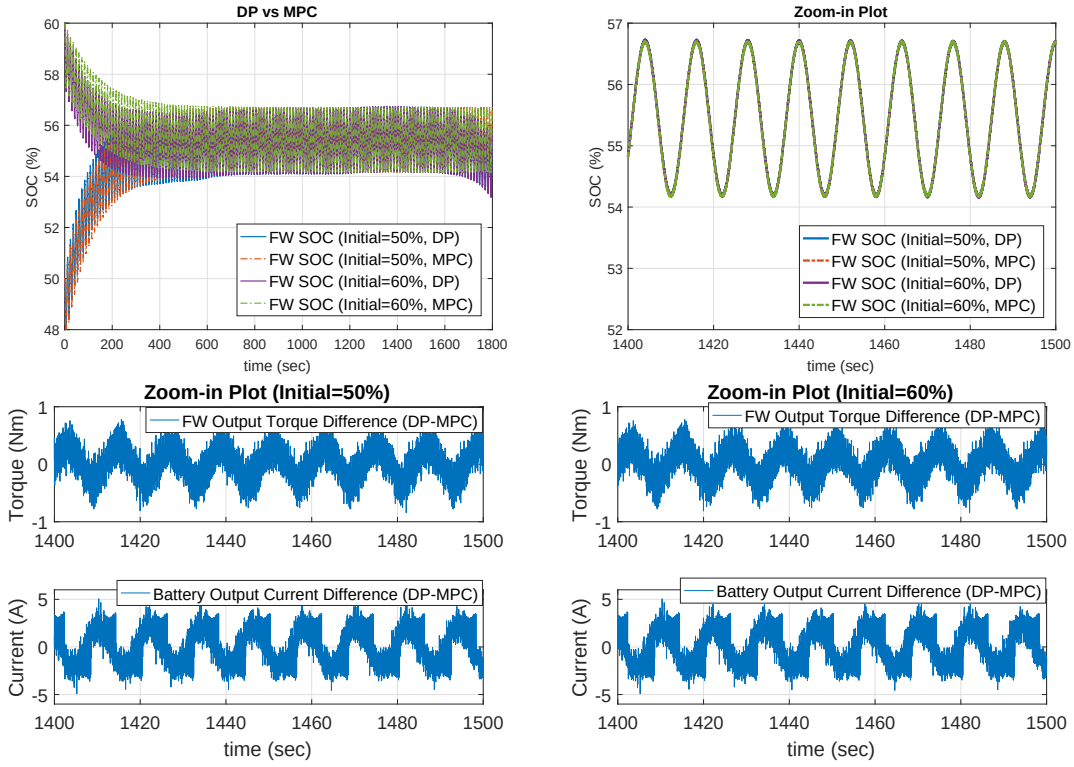

Figure 4.7: The performance comparison: MPC vs. DP.

The performance metrics in Table 4.1 and the two main objectives, i.e., RMS tracking error (RMS Error) and HESS losses ($Loss\%$), are used to evaluate the performance of the proposed MPC and DP with different initial flywheel SOC. The initial SOC of the battery is $x_B(t) = 80\%$. The first group is defined as "DP (50%)" and "MPC (50%)", i.e., the initial SOC of the flywheel is $x_{FW}(t) = 50\%$, and the second one is defined as "DP (60%)" and "MPC (60%)", i.e., the initial SOC of the flywheel is $x_{FW}(t) = 60\%$. For different initial SOCs, γ is fixed. The best performance metrics are in blue, and the worst are in red. As shown in Table 4.3, the performance of MPC is close to that of DP. The DP global optimal solution achieves better performance in terms of two main objectives in the cost function, i.e., "$Loss\%$" and "RMS Error". MPC achieves smaller peak current ($I_{B_{Peak}}$) and less battery usage ($I_{B_{RMS}}$) (which are not in the cost function), leading to reduced battery losses and extended battery life. Note that the differences between MPC and DP are relatively small. This case study demonstrates

Table 4.3: Performance comparison of the proposed MPC and DP.

	DP (50%)	MPC (50%)	DP (60%)	MPC (60%)
$I_{B_{RMS}}$	16.75A	16.25A	15.57A	14.81A
$I_{B_{Peak}}$	101A	101A	66.48A	60.4A
$I_{B_{1.5C}}\%$	0	0	0	0
$Loss_B\%$	0.08%	0.08%	0.07%	0.06%
$Loss_{FW_{Rs}}\%$	0.48%	0.49%	0.48%	0.48%
$Loss_{FW_f}\%$	0.67%	0.67%	0.67%	0.69%
Loss%	1.23%	1.24%	1.22%	1.23%
RMS Error	153.39W	197.54W	148.57W	179.63W

the effectiveness of the proposed MPC in terms of power-fluctuation compensation, HESS energy saving, and reduction of the battery usage; in particular, high-current operation.

The proposed MPC can be easily and effectively extended to the B/UC HESS solution. As shown in Figure 4.8, without the SOC penalty of UC, the short-horizon MPC is not able to maintain the UC operating in its high SOC range, because the benefit of maintaining it is too small in the short term and is therefore ignored in the optimization. As a result, the SOC of the UC drops quickly. As it decreases, the delivery of the same output power requires a larger current, thereby leading to significantly increased losses and power tracking error.

Therefore, to keep the UC working in a high efficiency range, another penalty on the UC SOC is considered for B/UC HESS:

$$\gamma_{UC_{SOC}}(x_{UC}(k) - SOC_{UC_d})^2, \tag{4.16}$$

With this SOC penalty, the UC supplies or absorbs as much power as possible, and the battery charges the UC to maintain its operation in a high SOC range. The effectiveness of this $\gamma_{UC_{SOC}}$ penalty is demonstrated by Figure 4.9.

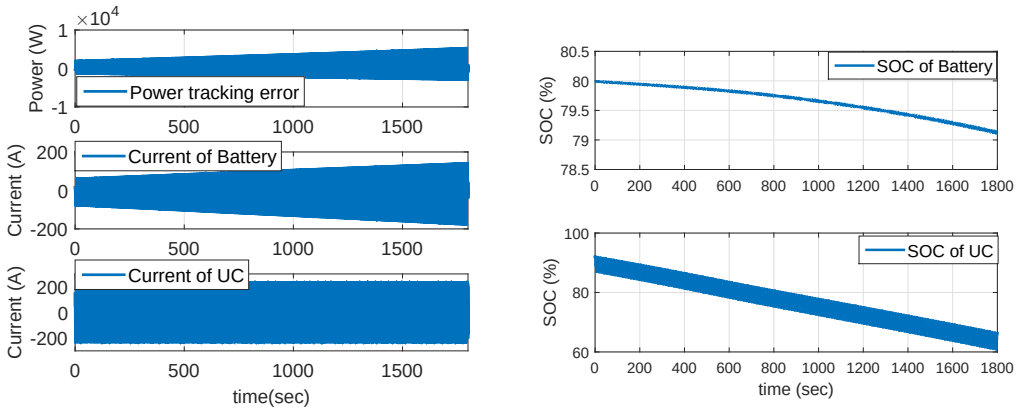

Figure 4.8: MPC (N=20, without UC SOC penalty) performance at sea state 4.

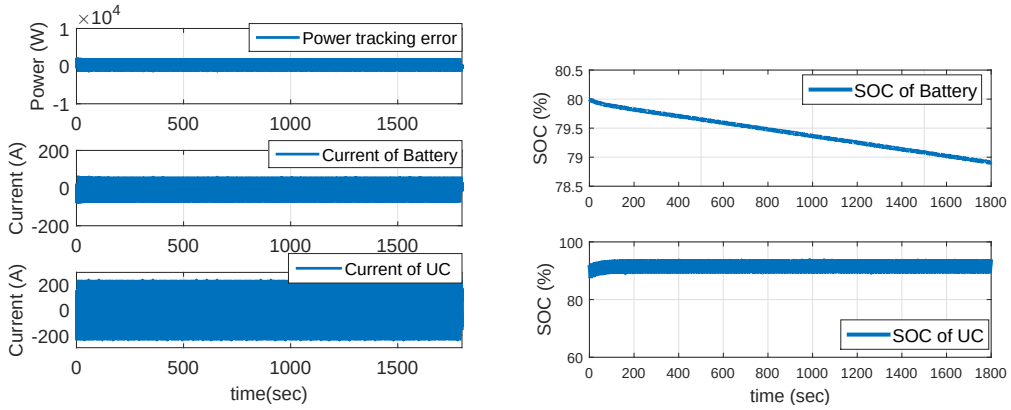

Figure 4.9: MPC (N=20, with UC SOC penalty) performance at sea state 4.

4.3 Summary

This chapter investigates the feasibility and effectiveness of different HESS configurations, namely batteries combined with flywheels and batteries combined with UCs, to mitigate load fluctuations. A comparative study is performed to provide insights into advantages and limitations of each configuration. A multi-objective optimization problem (MOP) is formulated to minimize the power tracking error and HESS losses. The best achievable solutions, namely Pareto fronts, are obtained by using dynamic programming. The comparison results indicate that the B/FW HESS configuration outperforms B/UC HESS at high sea state in terms of power fluctuation compensation and HESS efficiency. However, the spinning loss of the B/FW

HESS configuration will cause more losses at low sea state, which makes B/UC HESS configuration more suitable in these conditions. Furthermore, B/FW HESS is more "friendly" to batteries in terms of less battery usage, reduced peak current, and less high-current operation for batteries.

In this chapter, in order to enable the real-time implementation, a model predictive control algorithm is formulated to minimize the tracking RMS error and HESS losses for B/FW HESS. In order to overcome the limitations caused by the short predictive horizon of MPC, an additional penalty on the flywheel SOC is introduced to keep it working in the high-efficiency operation range. The comparison results of MPC and MOP demonstrate the effectiveness of the proposed MPC in terms of power-fluctuation compensation, HESS energy saving, and reduction of the battery usage and high-current operation. The proposed MPC can be easily and effectively extended to B/UC HESS in the way that an additional penalty on the SOC of UC is required.

CHAPTER V

Control Strategies Evaluation: Coordinated Control vs. Pre-filtered Control

In this chapter, we consider an HESS consisting of batteries and ultra-capacitors, and explore two control strategies with different levels of coordination among the HESS elements. The first approach decomposes the power command that is needed to counteract the fluctuation according to frequency range, and then controls the battery packs and ultra-capacitor banks independently. This approach will be referred to as control with pre-filtering (PF) in this chapter. In this case, the charging/discharging of the two components in HESS are optimized separately so that the ultra-capacitors handle high-frequency fluctuations, while the batteries handle low-frequency variations. The other approach, referred to as coordinated control (CC), treats the batteries and ultra-capacitors as a single entity and coordinates their charging/discharging to counteract the total load fluctuation through an optimization algorithm. The goal of this study is to quantify the performance difference and understand the critical roles of a control strategy in HESS implementation. In pursuing this goal, this study aims to provide insights into the trade-off between performance and control complexity. It should be noted that, while the PF leads to a relatively simple low-dimensional optimization problem, the CC is expected to offer improved performance. To characterize the performance of HESS, the performance of a single type of energy storage

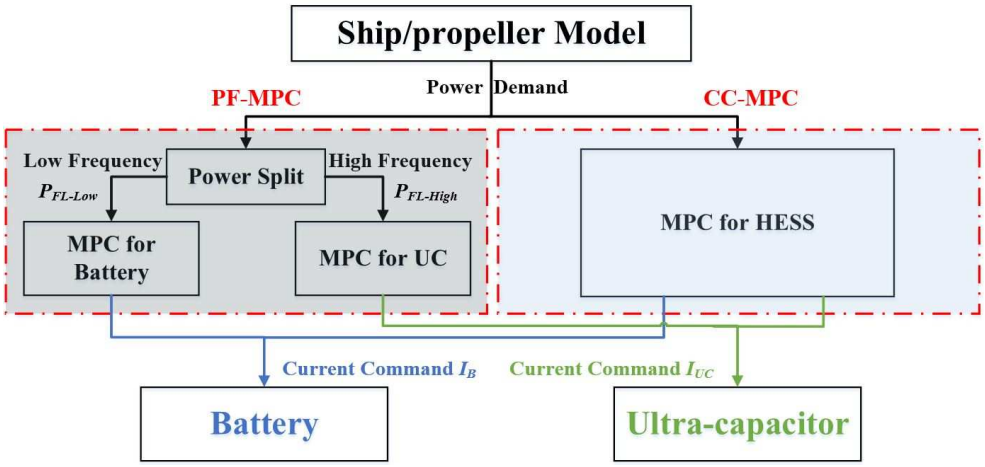

Figure 5.1: Control strategy diagram: left: PF-MPC, right: CC-MPC.

will be included in this study as a benchmark.

5.1 MPC Problem Formulation

In this section, we apply the receding-horizon approach to develop a real-time energy management scheme that incorporates feedback and is amenable for real-time computation. Given the nature of the energy storage system, as well as the operating constraints involved, MPC becomes the natural formulation. Because of the distinctive frequency components in the load power fluctuation P_{FL}, and the different dynamic responses of the battery and UC, two ways of structuring the MPC problem are considered, as illustrated in Figure 5.1. One is control with pre-filtering, where the charging/discharging of UC and battery modules are optimized such that the UC power P_{UC} counteracts high-frequency fluctuations $P_{FL-High}$ while the battery power P_B deals with low-frequency variations P_{FL-Low}. $P_{FL-High}$ and P_{FL-Low} refer to the high-and low-frequency components in P_{FL}, respectively. The other, referred to as coordinated control, coordinates the charging/discharging of the battery together with UC to optimize the power split between them to deal with the total power fluctuation. Similar to MOP, the uncertainties in P_{FL} are not taken into consideration.

The cost function in MPC is formulated based on the minimization of RMS tracking error and HESS losses. We discretize the system model developed in Chapter II with the sampling time T_s. No terminal cost is incorporated in this MPC formulation. As discussed in Chapter IV, the SOC penalty $\gamma_{UC_{SOC}}$ in Equation (4.16) can effectively improve the system performance by ensuring that the UC is operating in its high-efficiency range. Therefore, the specific variables and functions in the CC-MPC formulation are defined as:

$$J_{HESS} = \sum_{k=t}^{t+N-1} L_{HESS}(x(k), u(k)), \tag{5.1}$$

where,

$$\begin{aligned} L_{HESS}(x(k), u(k)) =& \lambda_{Tracking}(P_{FL}(k) - P_B(k) - P_{UC}(k))^2 \\ &+ \lambda_{Loss}(N_B R_B u_B^2(k) + N_{UC} R_{UC} u_{UC}^2(k)) \\ &+ \gamma_{UC_{SOC}}(x_{UC}(k) - SOC_{UC_d})^2; \end{aligned} \tag{5.2}$$

subject to the same constraints in Equations (4.7) and (4.8), and $u = [u_B, u_{UC}]$, where $\lambda_{Tracking}$, λ_{Loss}, and $\gamma_{UC_{SOC}}$ are the weights on power tracking error penalty, the energy loss penalty, and UC SOC charging penalty, respectively.

In the PF strategy, the batteries compensate low-frequency fluctuations and UCs compensate high-frequency fluctuations. As shown in Figure 2.3 of Chapter II, the high-frequency component in the load power fluctuation frequency spectrum is around 8Hz, while the low-frequency components are smaller than 1Hz. A second-order butterworth low-pass filter, whose cutoff frequency is set at 1Hz, is used to split the HESS power demand P_{FL} into high ($P_{FL-High}$) and low-frequency (P_{FL-Low}) components. Since both batteries and UCs are subject to constraints in (4.7), MPC will also be used in the PF strategy. The two separate MPC problems are defined for PF as:

MPC-B:

$$J_B = \sum_{k=t}^{t+N-1} L_B(x_B(k), u_B(k)), \tag{5.3}$$

where,

$$\begin{aligned} L_B(u_B(k)) =& \lambda_{Tracking}(P_{FL-Low}(k) - P_B(k))^2 \\ &+ \lambda_{Loss}(N_B R_B u_B^2(k)), \end{aligned} \tag{5.4}$$

subject to constraints related to battery in (4.7)-(4.8); and

MPC-UC:

$$J_{UC} = \sum_{k=t}^{t+N-1} L_{UC}(x_{UC}(k), u_{UC}(k)), \tag{5.5}$$

where,

$$\begin{aligned} L_{UC}(x_2(k), u_2(k)) =& \lambda_{Tracking}(P_{FL-High}(k) - P_{UC}(k))^2 \\ &+ \lambda_{Loss}(N_{UC} R_{UC} u_{UC}^2(k)) \\ &+ \gamma_{UC_{SOC}}(x_{UC}(k) - SOC_{UC_d})^2, \end{aligned} \tag{5.6}$$

also subject to constraints related to UC in (4.7)-(4.8).

To quantify the improvement in the HESS system performance, we also formulate the MPC problem for a system where only ultracapacitors are used. Because there is no battery to maintain the UC at a high SOC level, the penalty in Equation (4.16) is not included, which prevents the occurrence of an extremely large error on power tracking. Therefore, for the "UC only" configuration (UC-Only), the MPC problem is defined as:

$$J_{UCOnly} = \sum_{k=t}^{t+N-1} L_{UCOnly}(x(k), u(k)), \tag{5.7}$$

where,

$$\begin{aligned} L_{UCOnly}(x_{UC}(k), u_{UC}(k)) =& \lambda_{Tracking}(P_{FL}(k) - P_{UC}(k))^2 \\ &+ \lambda_{Loss}(N_{UC} R_{UC} u_{UC}^2(k)), \end{aligned} \tag{5.8}$$

subject to the constraints related to UC in (4.7) and (4.8).

Note that N_{UC} for the HESS configuration is 9, and for the "UC only" configuration, it is 14.

5.2 Performance Comparison and Results Analysis

With the models built in Chapter II and the HESS components determined above, we present a case study for quantifying the effects of different control strategies on the electric drive system with HESS. In the case study, the sampling time for the control update is chosen as 0.02 sec, which is properly matched with the underlying system dynamics. The self-sustained operation period is defined as the continuous time that the HESS can be used as the energy buffer for the electric propulsion system without requiring charging or discharging from external power sources (such as the diesel generator). This is determined to be 40 minutes for SS4 and 30 minutes for SS6. The generator will slowly charge the battery to the initial SOC after 40 minutes of continuous operation at SS4, and 30 minutes at SS6. The optimization problem is solved by sequential quadratic programming (SQP). The resulting performance is evaluated in terms of the following two metrics:

1. RMS tracking error: $\sqrt{J_1/N_T}$;
2. HESS losses: $Loss\% = \frac{J_2}{\sum_{k=0}^{N_T} P_{Demand}(k)} \times 100\%$.

Two case studies are performed in the following subsections. In the first case study, the rotational speed is assumed as constant, which means that the load torque is fully balanced by the motor torque. This gives us the worst-case scenario in terms of the mechanical power fluctuations being transferred to the electrical system. We focus on this worst case first since an attempt will be made to balance the motor torque given that 'the torque imbalance is responsible for the propeller wear and tear', as discussed in Section 5.5.5 of [20]. In the second case study, where the rotational speed is regulated by a PI controller, the filter effect of the propeller is considered.

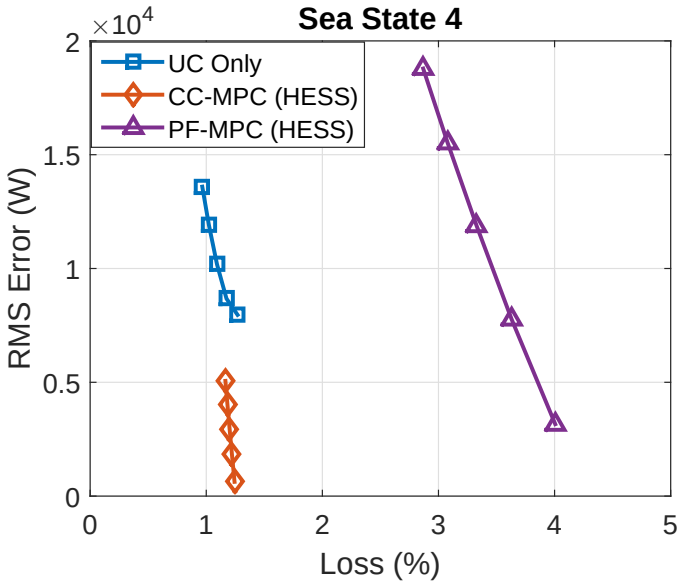

Figure 5.2: Pareto-fronts of UC-Only, CC-MPC and PF-MPC at sea state 4 (N=20).

5.2.1 Case I: Constant Propeller Rotational Speed

The weighting factors allow us to put different emphasis on each attribute to investigate the performance trade-off. By varying $\lambda_{Tracking}$, λ_{Loss} and $\gamma_{UC_{SOC}}$, the UC-Only (5.7), the PF-MPC (5.3)-(5.5) and the CC-MPC (5.1) problems are solved at sea states 4 and 6. The Pareto-fronts of these three solutions, which represent the best achievable system performance with HESS and only ultra-capacitors, are shown in Figures 5.2-5.3 with the predictive horizon $N = 20$. The results indicate that the CC-MPC has substantial advantages over the PF-MPC and UC-Only configurations in terms of mitigating the load power fluctuations and reducing losses at both sea states 4 and 6. Note that the constraints are not active in these simulation results. However, after a long self-sustained operation period, the SOC constraint of the battery will become active. MPC is able to guarantee the battery working within these constraints. If the performance is degraded, the HESS can be recharged before the battery reaches its constraints.

The key observations are summarized in the following remarks:

Remark 5.1: The Pareto-fronts give insight into the effectiveness of HESS with

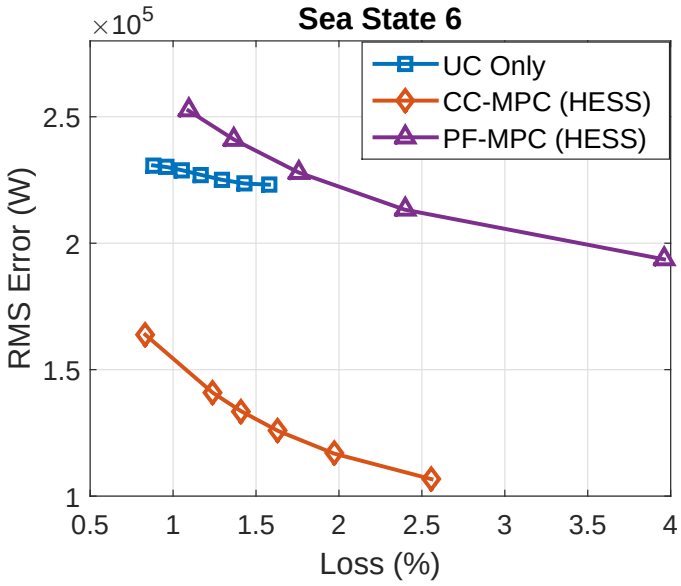

Figure 5.3: Pareto-fronts of UC-Only, CC-MPC and PF-MPC at sea state 6 (N=20).

MPC and the trade-off between the tracking RMS error and the HESS losses. As shown in Figures 5.2-5.3, the CC-MPC strategy has substantial advantages with regard to tracking error mitigation compared with the energy storage system with only ultra-capacitors. Furthermore, the CC-MPC strategy can reduce the tracking RMS error without significant increase in losses at sea states 4 and 6 compared with the PF-MPC strategy.

Remark 5.2: A proper control strategy is critical for capitalizing on the benefits of HESS. As can be seen from Figures 5.2 and 5.3, UC can do as well as (and even better than) the HESS if PF-MPC is used. Without proper coordination, the HESS does not have a convincing performance advantage.

Remark 5.3: Under coordinated control, the battery will properly charge the UC to keep it working in an efficient operating range to achieve a desired tracking performance with high efficiency, as shown in Figure 5.4 (a). In contrast, without coordination, the UC cannot assist the battery to reduce the losses, and the battery cannot properly charge the UC when needed, leading to a shortened self-sustained operation time and degraded performance, as shown in Figure 5.4 (b). Compared to

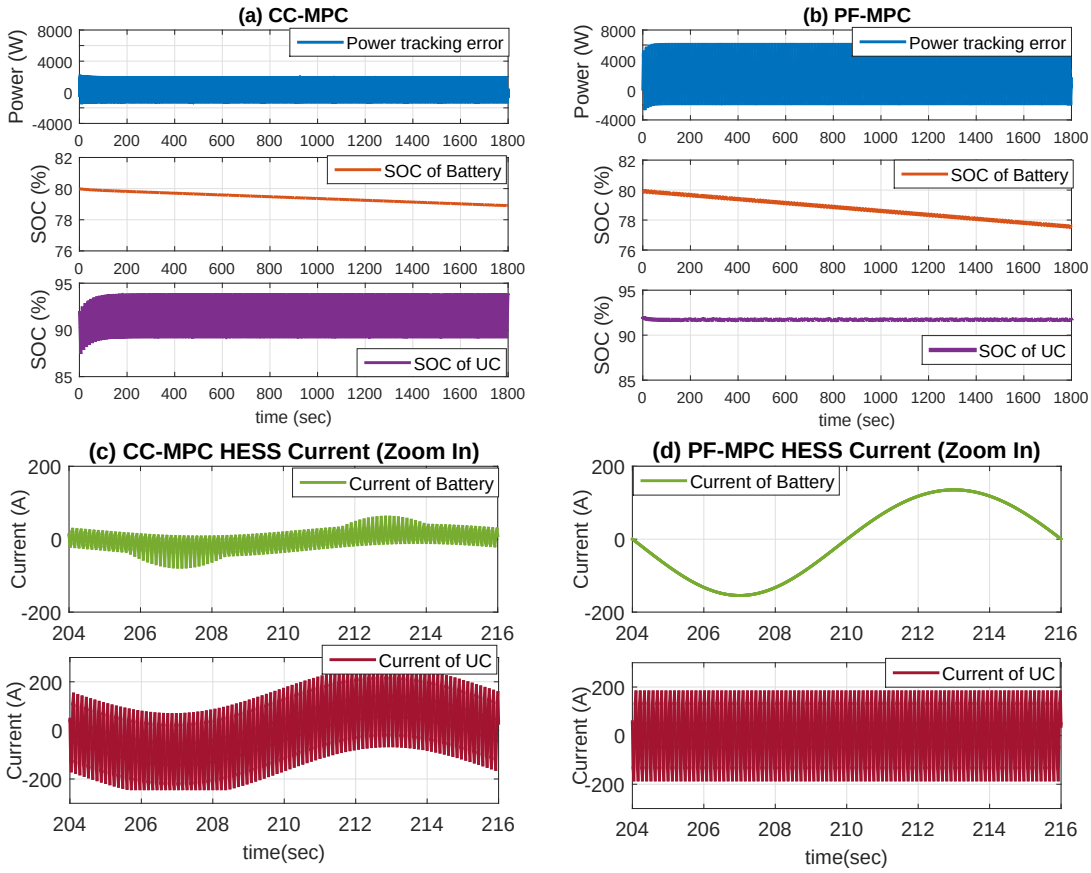

Figure 5.4: CC-MPC and PF-MPC performance at sea state 4.

the UC SOC result in Figure 5.4 (b), Figure 5.4 (a) shows a large variation of the SOC of the UC. This is because the UC in the CC-MPC compensates both high- and low-frequency fluctuations, but the UC in the PF-MPC compensates only high-frequency fluctuations. Therefore, the UC in the CC-MPC is used more efficiently than it is in the PF-MPC. Furthermore, the high-frequency fluctuations in the PF-MPC cannot be cancelled out or reduced to the level achieved by CC-MPC, as shown in Figure 5.4 (a), because of the penalty of the UC SOC in (5.6). Without this penalty, the UC SOC in PF-MPC will decrease quickly, and the tracking performance will deteriorate. Moreover, only when the UC is operating at high current levels will the batteries in the CC-MPC strategy start to work to assist in reducing the power tracking error and minimizing the losses, as shown in Figure 5.4 (c). With pre-filtering, however, the battery and UC can be working at cross purposes; namely, when one is charging the

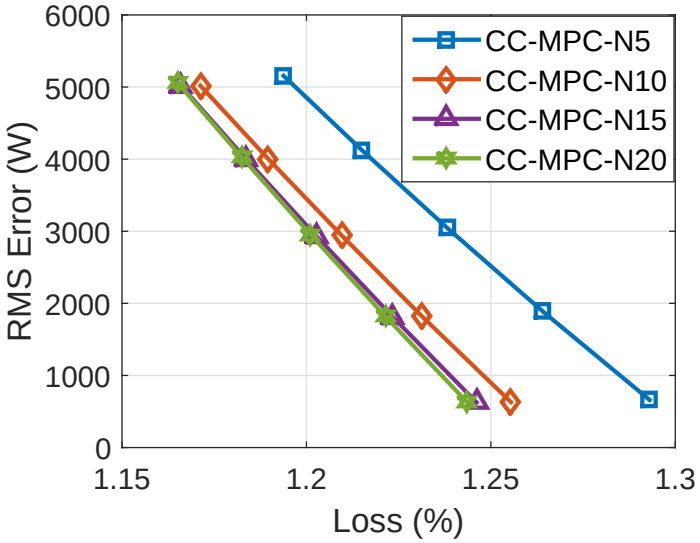

Figure 5.5: Sensitivity analysis of predictive horizon for CC-MPC at sea state 4.

other may be discharging. This causes additional losses and degrades power tracking performance, as shown in Figure 5.4 (d). Consequently, the overall energy consumed in the PF-MPC, as shown in Figure 5.4 (b), is much more than that in the CC-MPC shown in Figure 5.4 (a).

Remark 5.4: Extending the predictive horizon will generally improve performance, at the cost of increased computational complexity. To make the proposed solution feasible for real-time implementation, a short predictive horizon is used. A sensitivity analysis of the predictive horizon for CC-MPC is performed to gain insights into the trade-offs between these design attributes. As shown in Figures 5.5 and 5.6, the performance is relatively insensitive to the predictive horizon for this problem. Given that the required computation time depends on not only the algorithm but also the computation hardware, the work in this section does not directly prove real-time feasibility. Nevertheless, by providing evidence that a long prediction horizon is not needed for this problem, it provides strong support that an MPC-based solution can be practical. Moreover, this sensitivity analysis provides insight that can help designers manage the trade-off between performance and control complexity.

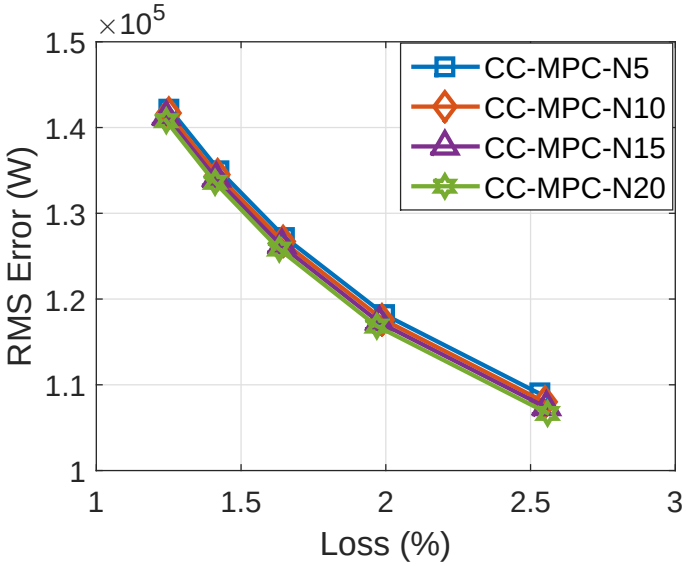

Figure 5.6: Sensitivity analysis of predictive horizon for CC-MPC at sea state 6.

5.2.2 Case II: Regulated Propeller Rotational Speed by a PI Controller

In order to consider the filter effect of the ship propeller, another case study is performed where the rotational speed of the propeller is regulated by a PI controller. The PI controller for the speed regulation is developed and tuned based on the algorithm given in Appendix B.1 in [19]: $K_P = \frac{1}{a}\frac{I_s}{T_{sum}}$ and $K_I = K_P/T_i$, where a=3 is a constant related to the damping ratio, $I_s = 4800kgm^2$ is the total propeller rotational inertia, $T_{sum} = 0.011sec$ is the lumped time constant of the motor and the shaft speed sensor filter, and $T_i = 0.1sec$ is the PID controller integral time constant. Since the high-frequency fluctuations are significantly filtered in Case II, batteries instead of ultra-capacitors are used as the single type of energy storage. The number of battery modules is set at 18, as shown in Table 2.4. This "battery only" configuration is defined as "B-Only" in this case study.

The Pareto-fronts of Case I and II are shown in Figure 5.7 and 5.8. The key observations are summarized in Remark 5.5.

Remark 5.5: As shown in Figure 5.7 and 5.8, the performance of PF-MPC in Case II is even worse than that in Case I. The reason for this can be explained

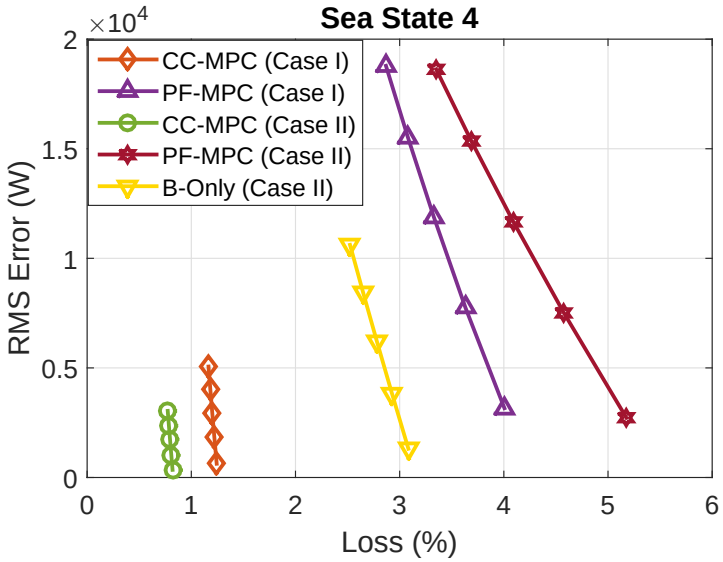

Figure 5.7: Pareto-fronts of Case I and II at sea state 4 (N=20).

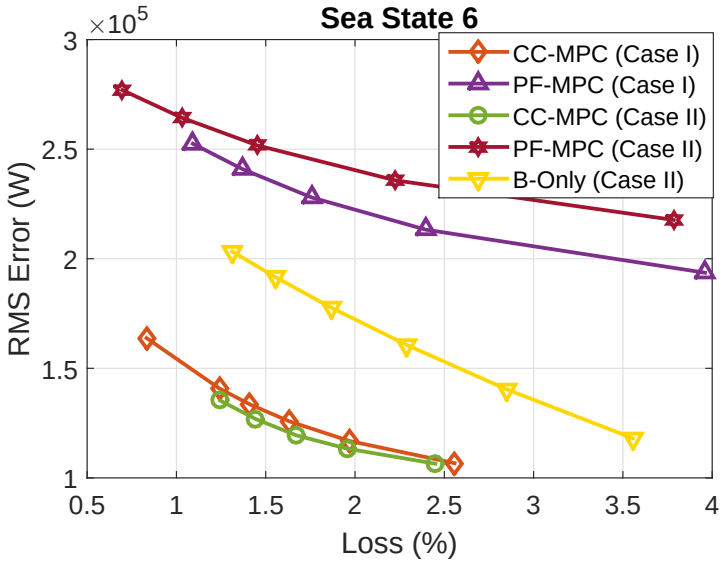

Figure 5.8: Pareto-fronts of Case I and II at sea state 6 (N=20).

as follows: The high-frequency power fluctuation in Case II is around 40% of that in Case I, due to the low-pass filter effect of the inertia and the speed controller in Case II. However, the low-frequency power fluctuations are almost the same, which means the battery losses $\sum_{k=0}^{N}(Power_{battery-loss}(k))$ are almost the same under the PF-MPC strategy. Because the losses of batteries are dominant among the total losses $\sum_{k=0}^{N}(Power_{battery-loss}(k) + Power_{UC-loss}(k))$, the performance metric

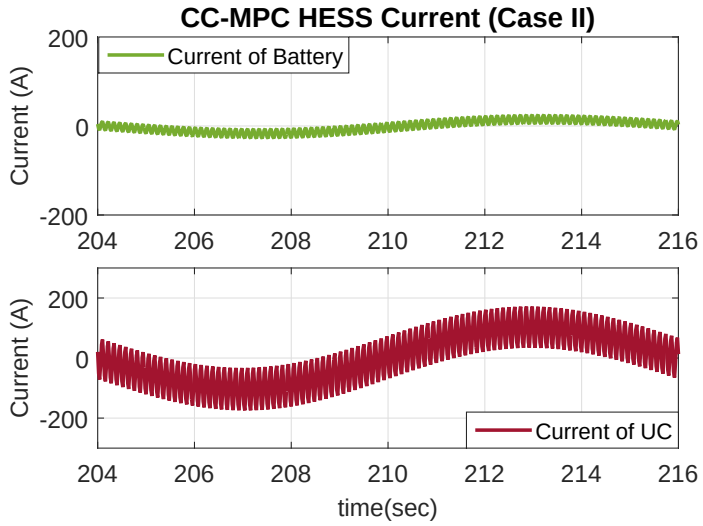

Figure 5.9: The HESS output currents of CC-MPC (Case II) at sea state 4.

$Loss\% = \frac{\sum_{k=0}^{N}(Power_{battery-loss}(k)+Power_{UC-loss}(k))}{\sum_{k=0}^{N}|P_{Demand}(k)|} \times 100\%$ gets worse as the total command power decreases. On the other hand, the performance of CC-MPC in Case II is better than that in Case I at sea states 4 and 6, as UCs with CC-MPC not only cancel out the high-frequency fluctuations but also help in dealing with the low-frequency fluctuations, as shown in Figure 5.9. As can be seen, the output currents of batteries and UCs are both reduced, as shown in Figure 5.9, compared to Figure 5.4(d), which indicates that the total HESS losses are significantly reduced and the battery life is extended. Compared to B-Only in Figure 5.7 and 5.8, CC-MPC outperforms B-Only at both sea states 4 and 6. This result provides the insight that, even though the high-frequency fluctuations are significantly filtered, with a proper strategy, UC is still essential to improve performance in terms of minimizing tracking error and losses. In summary, Case II also demonstrates the effectiveness of the proposed strategy CC-MPC under more realistic conditions.

5.3 Summary

In this chapter, control strategies with different levels of coordination among the HESS elements are studied, and the importance of the coordination is demonstrated. Due to the frequency characteristics of the power fluctuations, coordinated control (CC) and pre-filtering (PF) control strategies are investigated. A model predictive control is formulated based on the multi-objective optimization problem to minimize the tracking RMS error and HESS losses. A single type of energy storage is also studied to provide a benchmark in characterizing the performance of HESS. For the control strategy of HESS, two MPC-based strategies, CC-MPC and PF-MPC, are designed and evaluated. The comparison results indicate that the CC-MPC strategy outperforms the PF-MPC strategy in terms of power tracking, HESS efficiency, and self-sustained operation time. The sensitivity analysis of the predictive horizon for the coordinated control shows the feasibility of the MPC-based strategies for real-time applications. In summary, coordinated control is preferred to mitigate the shipboard load power fluctuations with HESS, given its superior performance and ability in trading off between achieving power tracking and reducing energy losses.

This study establishes a foundation for pushing HESS technology forward. The controllers of the generator sets, motor and other components in the electrical propulsion have not been taken into consideration in this chapter. The interaction analysis and energy management strategy design and evaluation for the HESS integrated with the existing electrical propulsion system will be presented in the next chapter.

CHAPTER VI

Energy Management Strategies for An Electric Ship Propulsion System with Hybrid Energy Storage

The integration and operation of a shipboard electrical propulsion system with HESS relies on well-configured HESS hardware and effective power/energy management strategies in order to mitigate the load power fluctuation effects and achieve the desired benefits of increased system efficiency, improved reliability, and reduced wear and tear. When the HESS is introduced into the existing shipboard electrical propulsion system, it will interact with the generator control systems. Without proper coordination, the HESS system and the generator control system could interfere with each other, thereby defeating the purposes of HESS. In [19], the widely used voltage regulator is applied to battery packs to regulate the DC bus voltage, in order to support the propulsion power. The PI controller is used in [41] for UC to deal with the pulse power load, leading to system efficiency improvement. In [49], the batteries and UC work with generators to follow the load profile and reduce fuel consumption. These control strategies are used to accommodate step or pulse changes in load power, which differ from the propulsion load fluctuations caused by the hydrodynamic interactions and wave excitations. To the best knowledge of the author, the special

challenges associated with the multi-frequency characteristics of the propulsion load fluctuations and HESS control, as well as the interactions between the HESS control and primary power generation control systems in dealing with dynamic load fluctuations, have not been well addressed. To address this problem, four control strategies are studied and analyzed in the first section.

In order to develop a proper control strategy, there are two ways to integrate a new HESS with the existing propulsion system. One is defined as a 'plug-in configuration', i.e., the new HESS controller works by itself without active coordination with the existing propulsion system. The other is defined as 'integrated configuration', in which a new integrated controller is developed for the whole propulsion system, including HESS, propulsion motor, and other power generation systems. In this chapter, energy management strategies for both plug-in and integrated configurations are studied and analyzed. The HESS studied in this chapter is based on the B/UC HESS in Chapter V; i.e., six battery modules and nine UC modules. Similar analysis can be extended to a battery with flywheel HESS.

6.1 Energy Management Strategies for the Plug-in Configuration

The HESS needs to work with existing control systems in the shipboard power network in order to achieve the expected benefits of efficiency and reliability improvement. To understand the benefits and limitations of different control designs, four strategies are investigated in this section, as described in Table 6.1. The general diagram of the system that embodies these different strategies is shown in Figure 6.1.

Table 6.1: Properties of control strategies.

Strategies	Properties
1. Baseline System (BL) without HESS	Generator control only, HESS is disconnected.
2. Motor Load Following (MLF) with HESS	HESS control is based on the motor load information, the bus voltage and motor power information is not used.
3. Bus Voltage Regulation (BVR) with HESS	HESS control is based on the bus voltage information, the information about the motor load and motor power is not used.
4. Coordinated Energy Management System (EMS) with HESS	HESS control is based on system information, including the bus voltage, generator output power, motor input power, and motor load power.

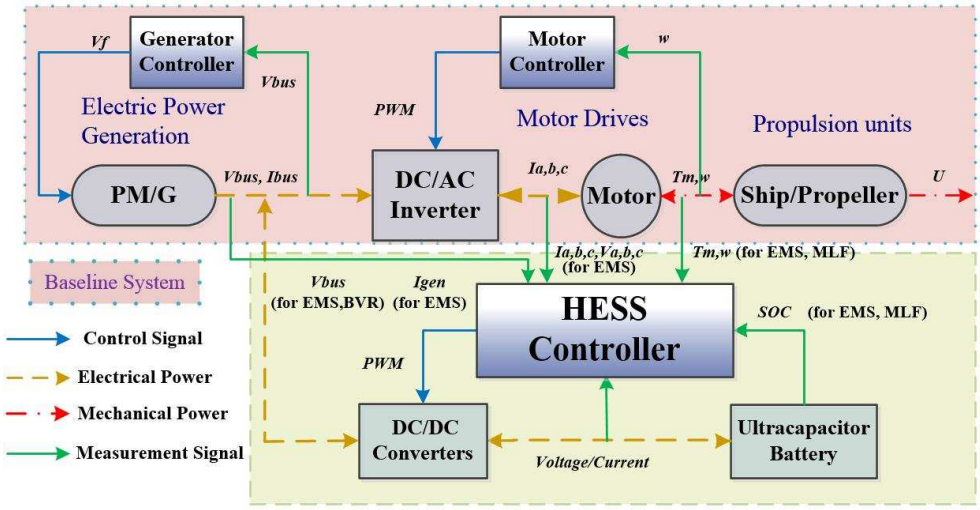

Figure 6.1: Schematic of the electric propulsion system with HESS control strategies for the comparative study.

6.1.1 Baseline Control System without HESS

In the baseline (BL) case, a propulsion motor is controlled by a load-following strategy, and a PI bus voltage regulator is used as the generator control. Without the HESS, the response of the baseline system serves as a benchmark to evaluate the benefits or drawbacks of the other strategies. The PI voltage regulator with anti-windup for the generator control has been successfully used in marine applications [19, 82]. In this section, the same PI voltage regulator for the generator control is used for the BL system, as well as for the other three control strategies, when evaluating

the performance of each strategy.

To simplify the control system, linearized models are developed around an operating point. The block diagram of the feedback system for BL is shown in Figure 6.2, where G_{Gen}, G_{Bus}, and G_{IM} are the transfer functions for the generator with its rectifier, DC bus, and induction motor with its drive, respectively. The current changes in the induction motor (IM) caused by the load fluctuation are treated as a disturbance on the bus. The overall system response, treating the desired bus voltage V_d and the load fluctuation LF as the external inputs and the bus voltage error $E_{DC} = V_d - x_{DC}$ as the performance variable, can be characterized as follows:

$$E_{DC} = \frac{1}{1 + G_{Gen}G_{Bus}} V_d + \frac{G_{IM}G_{Bus}}{1 + G_{Gen}G_{Bus}} LF. \tag{6.1}$$

The time response of the baseline system is shown in Figure 6.3. Note that all the simulation results presented herein are implemented at Sea State 4 and the average ship speed is 12.4 knots.

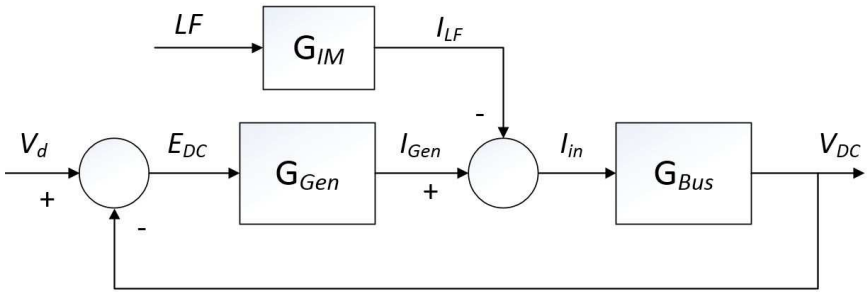

Figure 6.2: The block diagram of the feedback system with the baseline strategy.

6.1.2 Motor Load Following Control with HESS

The motor load-following (MLF) strategy for HESS has been explored in many power and energy applications, such as hybrid electric vehicles. This strategy often exploits a given load profile or a predictive model. In this section, it utilizes the motor load information to develop HESS energy management and achieve the optimal

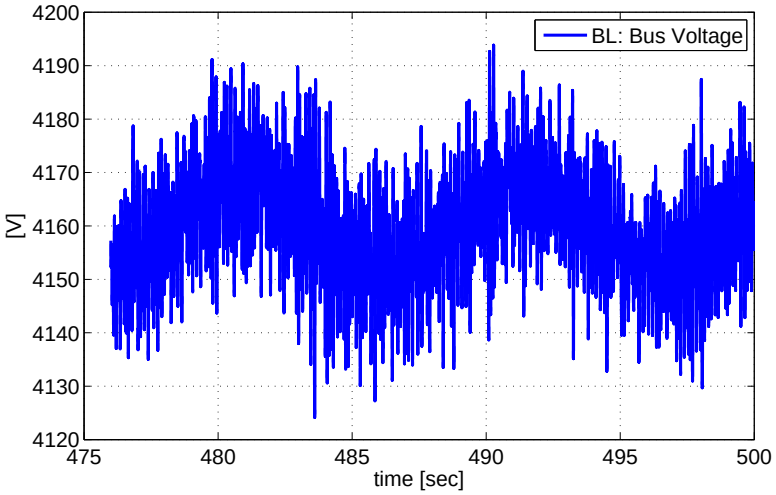

Figure 6.3: The bus voltage response with the baseline strategy at sea state 4.

performance. However, as shown in Figure 6.4, while HESS control reduces the low frequency content on the DC bus, it generates more high frequency fluctuations, leading to deteriorated performance. At a high sea state when the low frequency disturbance is dominant, as shown in Figure 2.3, this strategy could be effective. Unfortunately, at a low sea state it will result in a performance that is even worse than that of the baseline, due to the interaction and the lack of coordination between the voltage regulation loop and load following loop.

To understand and explain the responses shown in Figure 6.4, a model-based analysis is performed. To simplify the analysis, the HESS is assumed to follow the load fluctuation command without tracking error. The block diagram of the simplified feedback system for MLF is shown in Figure 6.5, whose bus error dynamics can be described by:

$$E_{DC} = \frac{1}{1 + G_{Gen}G_{Bus}} V_d + \frac{(G_{IM} - 1)G_{Bus}}{1 + G_{Gen}G_{Bus}} LF. \tag{6.2}$$

Compared with Equation (6.1), MLF does not influence the system sensitivity function, which represents the dynamic relationship from the command to the output

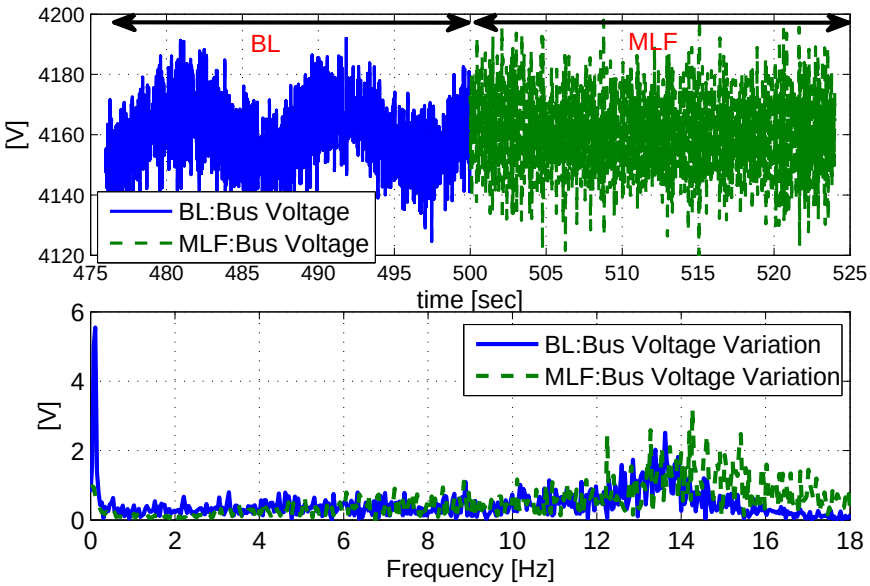

Figure 6.4: Performance comparison of BL and MLF: bus voltage response (top plots) and their frequency spectrums (bottom plots) at sea state 4.

error. However, the disturbance transfer function, namely from the load fluctuation to output error, differs from that of the BL strategy. As shown in Figure 6.6, the bus voltage variation is significantly reduced at low frequencies, compared to BL, but noticeably increased at high frequencies, which explains the dynamic behavior shown in Figure 6.4. The result can be attributed to the fact that this strategy does not take the motor dynamics and the generator dynamics into consideration in HESS energy management. It uses only the load information and ignores some system information (especially the DC bus information), and therefore works independently from the generator control.

6.1.3 Bus Voltage Regulation with HESS

Bus voltage regulation (BVR) is one of the most widely used control strategies for energy storage systems, especially in uninterruptible power supply (UPS) applications. It is a simple control architecture (voltage measurement and feedback) which aims to stabilize the bus voltage. When HESS is introduced, BVR is a natural choice

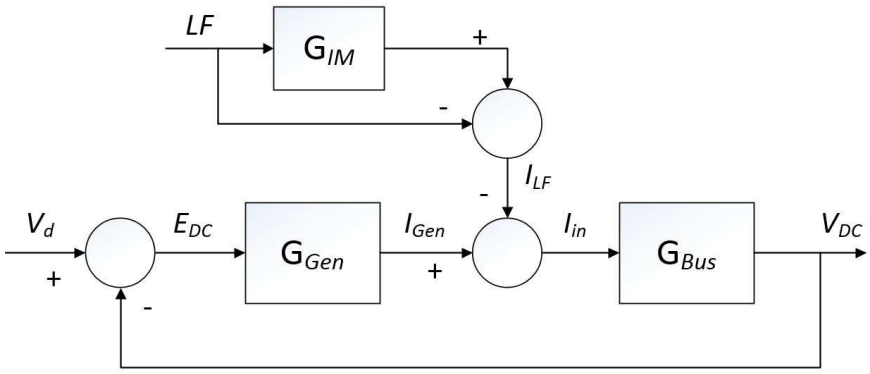

Figure 6.5: The block diagram of the feedback system with the MLF strategy.

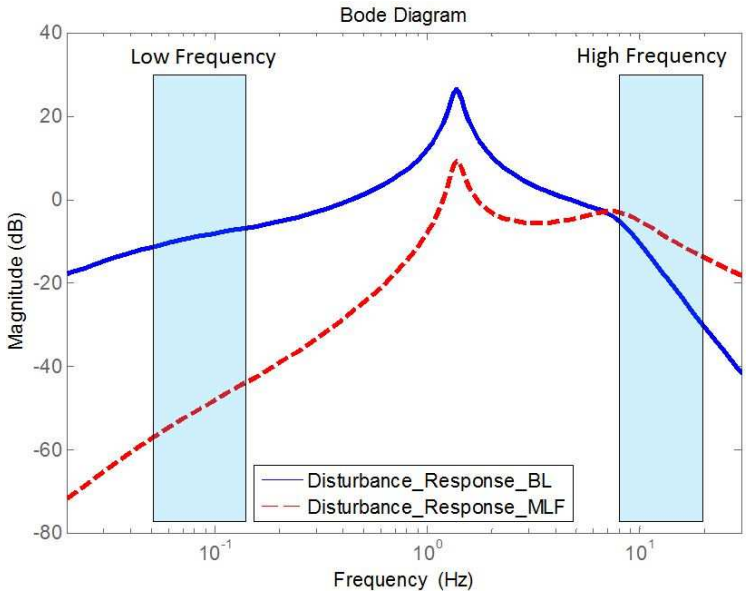

Figure 6.6: Bode plot of load fluctuation response ($LF \rightarrow E_{DC}$) by BL and MLF.

for controlling the energy storage to reduce the bus voltage fluctuation caused by power and thrust variations on the electric drive. Here two PI controllers are used for batteries and UCs, as expressed in the following:

$$I_B = (K_{P_b} + K_{I_b}/s) \times (V_d - x_{DC}),$$

$$I_{UC} = (K_{P_{uc}} + K_{I_{uc}}/s) \times (V_d - x_{DC}),$$

where $K_{P_b}, K_{I_b}, K_{P_{uc}}$ and $K_{I_{uc}}$ are the control parameters of batteries and UCs.

The BVR strategy implements bus voltage regulation on the generators and HESS.

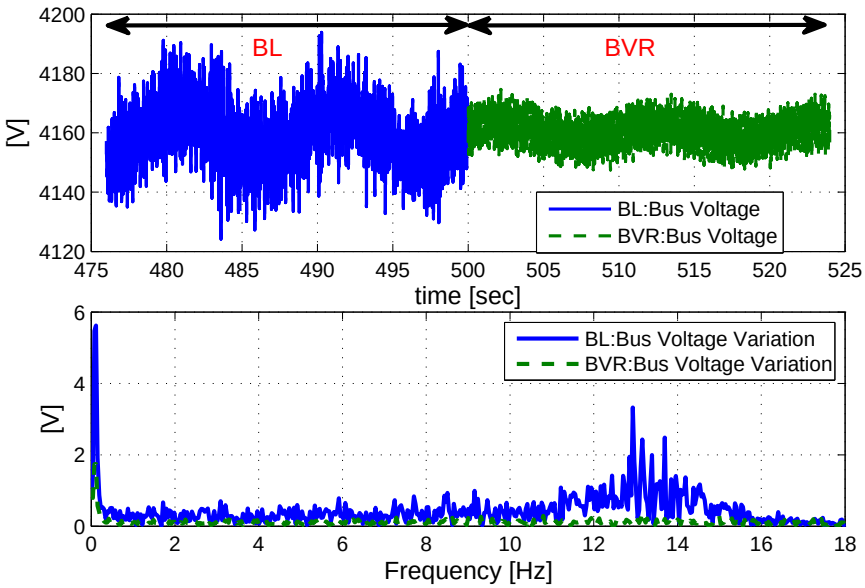

Figure 6.7: Performance comparison of BL and BVR: bus voltage response (top plots) and their frequency spectrums (bottom plots).

Compared to the baseline performance, the HESS introduces some benefits by reducing the DC bus voltage variations in both the low frequency and high frequency range, as shown in Figure 6.7.

To perform the interaction analysis of BVR, the block diagram of the feedback system for BVR is given in Figure 6.8, and the simplified system dynamic can be represented by:

$$\begin{aligned} E_{DC} =& \frac{1}{1+(G_{Gen}+G_{HESS})G_{Bus}} V_d \\ &+ \frac{G_{IM}G_{Bus}}{1+(G_{Gen}+G_{HESS})G_{Bus}} LF, \end{aligned} \tag{6.3}$$

where G_{HESS} represents the dynamics of HESS with PI controllers.

As shown in Figure 6.9, compared to the BL strategy, the load fluctuation effect in both the low frequency and high frequency range is reduced. Note that the generator and battery controls are additive, as shown in Figure 6.8. The current I_{DC} (sum of the currents from generator, I_{Gen}, and HESS, I_{HESS}) aims to mitigate the load

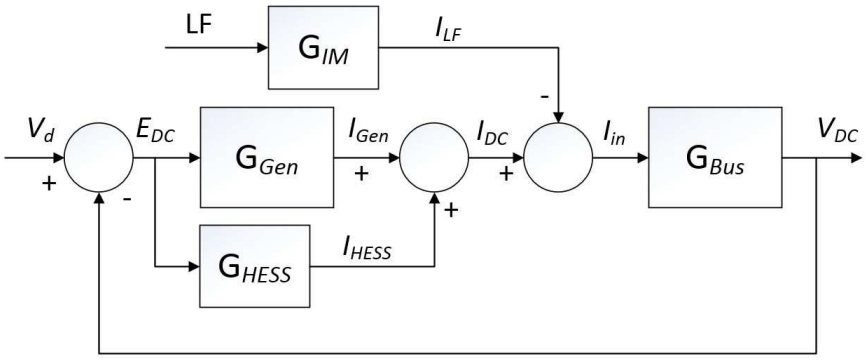

Figure 6.8: The block diagram of the feedback system for the BVR strategy.

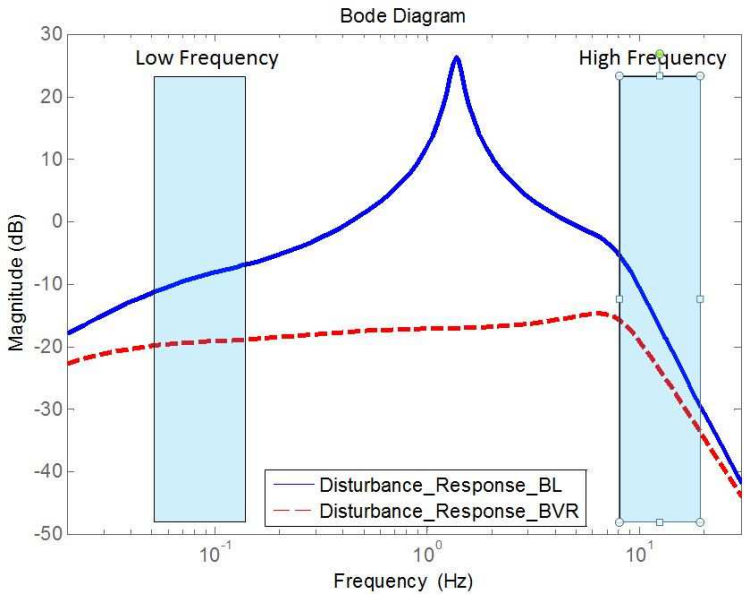

Figure 6.9: Bode plot of load fluctuation response ($LF \rightarrow E_{DC}$) by BL and BVR.

fluctuation current (I_{LF}) effect on the DC bus. Without proper coordination, I_{Gen} and I_{HESS} may cancel each other before dealing with the load fluctuation. This is indeed the case as highlighted in Figure 6.10, which shows that I_{Gen} and I_{HESS} are flowing in the opposite direction. These phenomena will result in unnecessarily high currents for both generators and HESS, leading to increased losses and reduced efficiency.

To summarize, the problem in MLF and BVR is that the HESS does not properly coordinate with other components and fails to take advantage of all system infor-

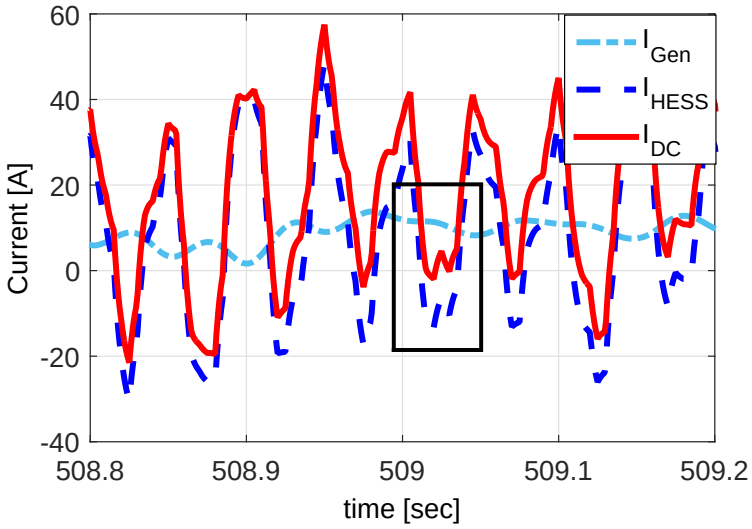

Figure 6.10: Undesirable interaction: fluctuating currents from the generator and battery pack for the system with BVR.

mation. Hence, to deal with the load fluctuation problem in electric ship propulsion system, a coordinated energy management strategy (EMS) is proposed in the following.

6.1.4 Coordinated HESS EMS

Optimization-based control is used for the proposed EMS to improve system efficiency and reliability. The optimization goals are to minimize the DC bus variation, power tracking error and HESS losses, and avoid the battery high current operation. Taking the induction motor dynamics into consideration, the power tracking command $P_{FL} = P_M - P_{DCM}$ is the fluctuation of the induction motor input power, where P_M is the motor input electrical power and P_{DCM} is the DC value of P_M, obtained by passing P_M through a low pass filter. The bus voltage defined by Equation (2.12) is introduced to the dynamic system equation and incorporated in optimization. The MPC formulation for this EMS takes the following specific form:

$$P(x_0): \min_{x:[t,t+N]\to R^n u:[t,t+N-1]\to R^m} J(x,u), \tag{6.4}$$

where:

$$J(x(t), u(t)) = \Phi(x(t+N)) + \sum_{k=t}^{t+N-1} L(x(k), u(k)), \tag{6.5}$$

$$\Phi(x(t+N)) = \lambda_{VDC}(V_d - x_{DC}(t+N))^2, \tag{6.6}$$

$$\begin{aligned} L(x(k), u(k)) =& \lambda_e(P_{FL}(k) - P_B(u_B(k)) - P_{UC}(x_{UC}(k), u_{UC}(k)))^2 \\ &+ \lambda_{HESS}(R_B u_B^2(k) + R_{UC} u_{UC}^2(k)) \\ &+ \lambda_{VDC}(V_d - x_{DC}(k))^2, \end{aligned} \tag{6.7}$$

subject to the constraints:

$$\begin{aligned} 20\% \leq x_B \leq 90\%, \\ 75\% \leq x_{UC} \leq 99\%, \\ -200A \leq u_B \leq 200A, \\ -240A \leq u_{UC} \leq 240A, \end{aligned} \tag{6.8}$$

$$\begin{aligned} x_B(k+1) =& x_B(k) - \frac{T_s}{3600 Q_B} u_B(k), \\ x_{UC}(k+1) =& x_{UC}(k) - \frac{T_s}{V_{max} C_{UC}} u_{UC}(k), \\ x_{DC}(k+1) =& x_{DC}(k) + \frac{T_s}{C_{Bus} x_{DC}(k)}(P_{Gen} - P_M) \\ &+ \frac{T_s}{C_{Bus} x_{DC}(k)}(P_B(u_B(k)) + P_{UC}(x_{UC}(k), u_{UC}(k))), \end{aligned} \tag{6.9}$$

where P_B and P_{UC} are the power generated by the battery and UC in Equation (2.11), λ_e is the power tracking error penalty, λ_{HESS} is the penalty for losses in the batteries and UCs, and λ_{VDC} is the penalty for DC bus voltage variation. Equation (6.9) is discretized from Equation (2.10) and (2.12) with a sampling time of T_s. The MPC solves the optimization problem in Equation (6.4) at each sampling time instance, implements the first element of the control sequence from the solution of Equation (6.4), and then moves on to the next sample time with a receding horizon.

The EMS strategy is developed using the system information, including the bus

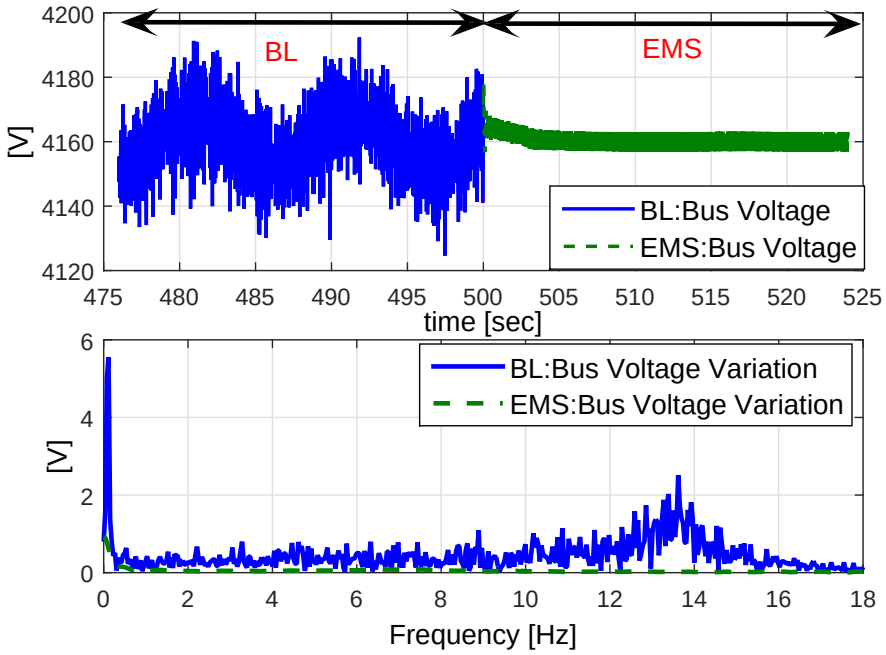

Figure 6.11: Performance comparison of BL and EMS: bus voltage response (top plots) and their frequency spectrums (bottom plots).

voltage, motor power, and ship propulsion load. This strategy is to minimize a cost function that includes the power tracking error, DC bus voltage variation and HESS electrical losses, subject to constraints of battery and ultra-capacitor SOC limits and charging/discharging limits. As shown in Figure 6.11, the EMS more effectively reduces the DC bus variation than the BL strategy does. Since the bus voltage error is significantly reduced by the EMS, the generator will provide almost constant power, which results in reduced fuel consumption.

6.1.5 Comparative Study and Simulation Results

To validate the interaction analysis and evaluate the different coordination strategies, a comparative study is performed for the four strategies using the simulation-oriented model. In order to quantify the performance of each strategy, the corresponding performances have been evaluated in terms of the following metrics:

1. DC bus voltage variations measured by rms and maximum absolute value.

Table 6.2: Performance comparison of different control strategies.

Sea State 2.				
	BL	MLF	BVR	EMS
Bus RMS Error	**8.401V**	**11.76V**	**4.33V**	**2.16V**
Bus Max Error	**28.91V**	**39.15V**	**9.07V**	**6.10V**
PM/G RMS	**23.18kW**	**27.65kW**	**8.01kW**	**4.14kW**
PM/G Max	**72.77kW**	**103.59kW**	**27.36kW**	**10.01kW**
HESS Loss%	N/A	**0.34%**	**0.79%**	**0.24%**
IB_{high}%	N/A	**0.0%**	**3.542%**	**0.0%**
Sea State 4 (nominal condition).				
	BL	MLF	BVR	EMS
Bus RMS Error	**10.89V**	**11.75V**	**4.74V**	**2.47V**
Bus Max Error	**37.28V**	**40.51V**	**14.24V**	**3.24V**
PM/G RMS	**31.75kW**	**27.14kW**	**10.83kW**	**4.69kW**
PM/G Max	**97.22KW**	**104.67kW**	**38.64kW**	**13.12kW**
HESS Loss%	N/A	**0.44%**	**0.87%**	**0.29%**
IB_{high}%	N/A	**0.146%**	**7.188%**	**0.0%**
Sea State 6.				
	BL	MLF	BVR	EMS
Bus RMS Error	**24.87V**	**12.67V**	**9.70V**	**4.75V**
Bus Max Error	**52.32V**	**42.53V**	**21.28V**	**7.68V**
PM/G RMS	**74.29kW**	**28.96kW**	**32.07kW**	**7.32kW**
PM/G Max	**197.26kW**	**138.53kW**	**188.61kW**	**51.21kW**
HESS Loss%	N/A	**1.51%**	**1.70%**	**1.18%**
IB_{high}%	N/A	**11.685%**	**38.771%**	**7.103%**

2. Diesel-generator power fluctuations measured by rms and maximum absolute value. The power fluctuations could cause additional fuel consumption and mechanical wear and tear.

3. Efficiency in terms of power losses in the electrical system due to energy cycling.

4. Battery "friendliness" in terms of the time spent charging/discharging the battery at high currents. Numerous research results show that fast charging/discharging can cause accelerated degradation in lithium battery systems [33]. We define IB_{high}% as the percentage of the high current operation ($I_{battery} \geq 150A$) over the total operation time.

A quantitative comparison of different strategies is summarized in Table 6.2 at three different sea states for a 24 second time frame. As can be seen, the results in

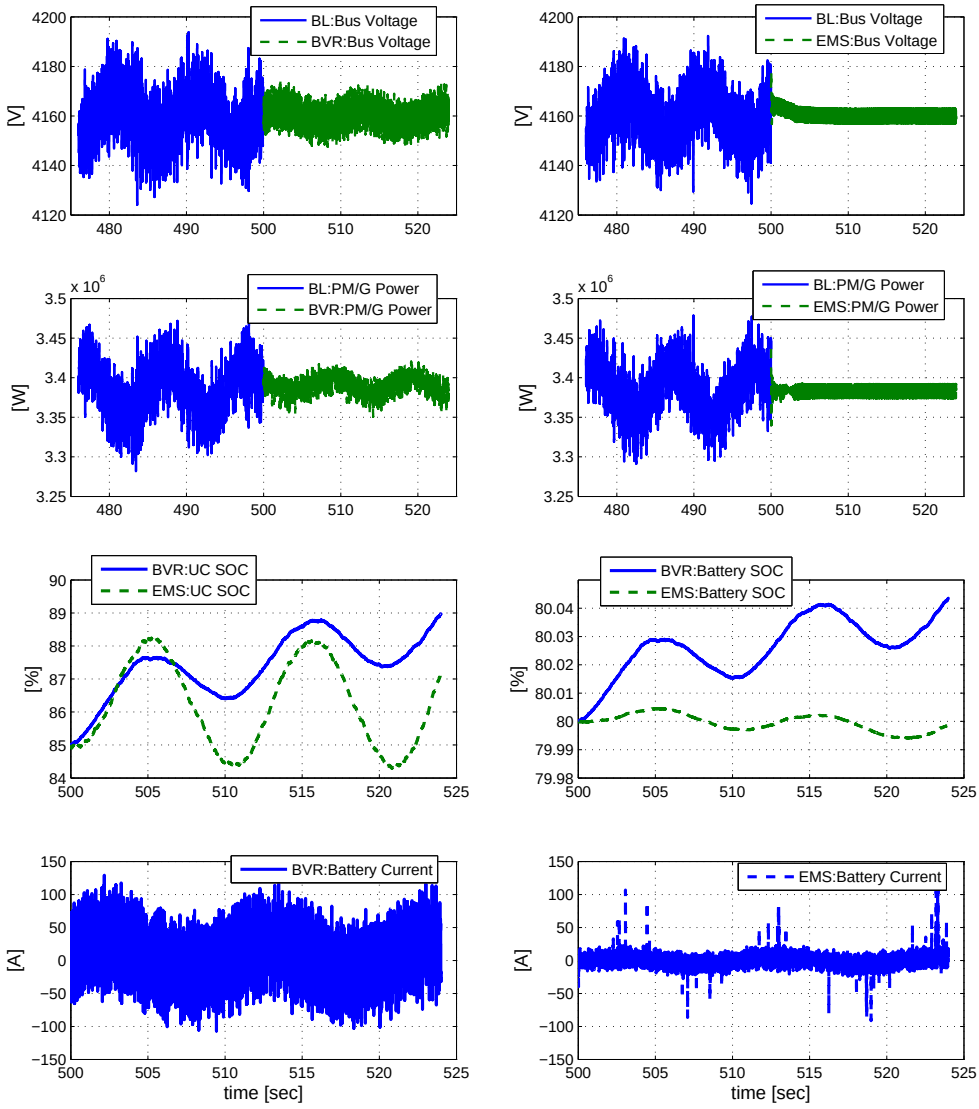

Figure 6.12: Performance comparison: BL, BVR and EMS.

Table 6.2 validate the interaction analysis discussed above. The performance from best to worst are colored in the following sequence: **blue**, **green**, **brown** and **red**.The MLF strategy achieves better performance at high sea states due to its effectiveness in reducing the low frequency variation. However, at the nominal and low sea states,

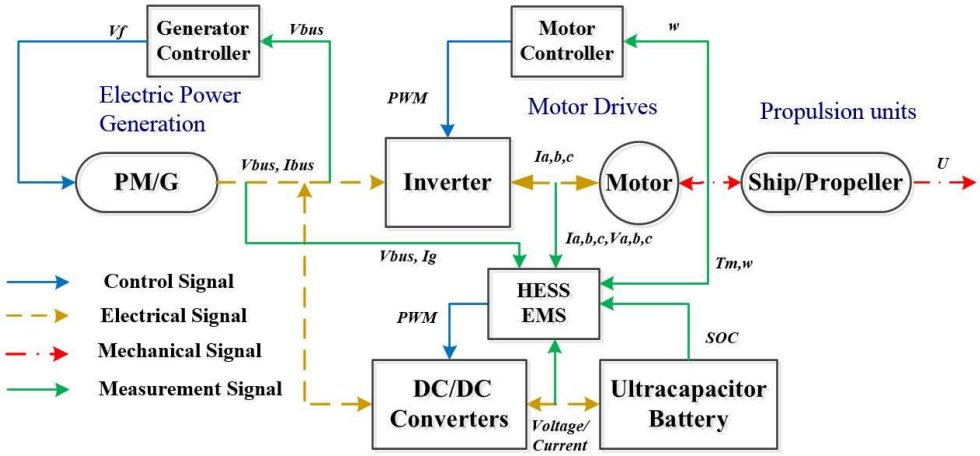

Figure 6.13: Schematic of HESS-EMS for the electric propulsion system with HESS.

MLF performs much worse than the BL strategy because of its problems in the high frequency range. The BVR strategy could better reduce some of the variations in the DC bus voltage and generator power compared with the BL strategy. However, due to the undesirable interaction with the generator, the BVR strategy incurs higher losses and is less "friendly" to the battery, as shown in Table 6.2 and Figure 6.12. Compared to the BVR case (see Figure 6.12), less SOC variations are observed for EMS. This translates into an extended self-sustained operation time. To summarize, the EMS achieves the best performance compared to other strategies in all the performance metrics considered at all sea states.

6.2 Energy Management Strategies for the Integrated Configuration

The EMS proposed in Section 6.1 incorporates information from the existing control system of the electric generation system and induction motor, and coordinates the operation of the batteries and ultra-capacitors. While this strategy has the advantage of being "add-on" and "plug-in" in the sense that it requires no changes to the existing control system of the generator sets and propulsion motor, it has no

authority to affect the generator and motor operation. This means that it is limited in dealing with system interactions. Because of these limitations, large torque and bus voltage variations have been observed in dynamic operation (such as pulse power loads [41]-[43]), which force the HESS to operate at its limits.

This section proposes a new integrated EMS to encompass the controls of the primary power sources and propulsion motor in addition to the HESS, to allow judicious coordination that can achieve desired performance. The new integrated EMS aims to increase system efficiency, enhance reliability, reduce mechanical wear and tear, and improve load-following capability by eliminating unintended and adverse interactions among the subsystems, especially in the dynamic load-following conditions. The model-based analysis and simulation demonstrate the benefits, as well as the potential cost, associated with the integrated EMS with system-level full-scale coordination. The HESS EMS with HESS-level coordination presented in last section is included to serve as a benchmark for the evaluation of the integrated EMS. This benchmark is referred to as an HESS energy management strategy (HESS-EMS), because it is developed for HESS alone. The general diagram of the HESS-EMS system is shown in Figure 6.13. While HESS-EMS can deal with some interactions among subsystems, its effectiveness is limited because the actions it can take are limited by the energy storage components. Compared to the benchmark, a comparison study is performed using model predictive control to demonstrate the proposed integrated EMS benefits.

6.2.1 Integrated System-Level EMS

To overcome the limitations of HESS-EMS in coordinating the power systems connected to the shipboard micro-grid, The new EMS will integrate the generator sets, electric motor, and HESS. It will be referred to as the system energy management strategy (SYS-EMS), given that it breaks the boundaries of HESS and other subsys-

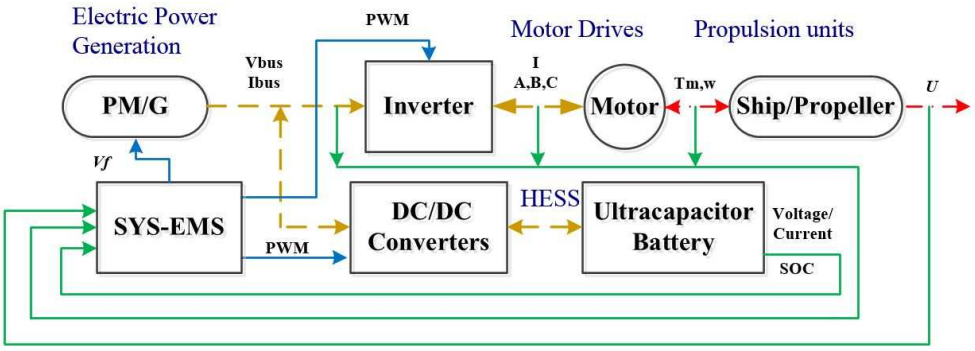

Figure 6.14: Schematic of SYS-EMS for the electric propulsion system with HESS.

tems. The general diagram of SYS-EMS is illustrated in Figure 6.14. In addition to minimizing power tracking error, HESS energy loss, and bus voltage variation as considered in HESS-EMS, the objectives of SYS-EMS include:

- keeping the motor shaft at its reference speed: $\min(\omega_d - x_M)$;
- making the electric power generator and induction motor operate near their most efficient operating points: $\min(P_{Gen}^{ref} - P_{Gen})$ and $\min(P_M^{ref} - P_M)$;
- reducing the generator output variations: $\min(x_G(k+1) - x_G(k))$;
- reducing mechanical wear and tear: $\min(u_M(k) - u_M(k-1))$;

where ω_d is the reference speed of the propulsion motor, and P_{Gen}^{ref} and P_M^{ref} are the reference powers of the generator sets and motor, respectively.

Therefore, the MPC formulation for SYS-EMS takes the following forms:

$$\Phi(x(N)) = \lambda_{VDC}(V_d - x_{DC}(N))^2 + \lambda_\omega(\omega_d - x_M(N))^2, \tag{6.10}$$

$$
\begin{aligned}
L(x(k),u(k)) =& \lambda_{VDC}(V_d - x_{DC}(k))^2 + \lambda_{\omega}(\omega_d - x_M(N))^2 \\
&+ \lambda_{P_{Gen}}(P_{Gen}^{ref} - x_{DC}(k)x_G(k))^2 \\
&+ \lambda_{P_M}(P_M^{ref} - x_M(k)u_M(k))^2 \\
&+ \lambda_{\Delta I_{PG}}(x_G(k+1) - x_G(k))^2 \\
&+ \lambda_{\Delta T_M}(u_M(k) - u_M(k-1))^2 \\
&+ \lambda_{HESS}(R_B u_B^2(k) + R_{UC} u_{UC}^2(k)),
\end{aligned}
\tag{6.11}
$$

subject to the inequality constraints:

$$
\begin{aligned}
20\% \leq x_B \leq 90\%, \\
75\% \leq x_{UC} \leq 99\%, \\
0 \leq x_G \leq 1000A, \\
0 \leq x_M \leq 160RPM, \\
-200A \leq u_B \leq 200A, \\
-240A \leq u_{UC} \leq 240A, \\
-10V \leq u_G \leq 10V, \\
-1.25 \times 10^6 Nm \leq u_M \leq 1.25 \times 10^6 Nm,
\end{aligned}
\tag{6.12}
$$

and the equality constrains:

$$\begin{aligned}
x_B(k+1) =& x_B(k) - \frac{T_s}{3600 Q_B} u_B(k), \\
x_{UC}(k+1) =& x_{UC}(k) - \frac{T_s}{V_{max} C_{UC}} u_{UC}(k), \\
x_{DC}(k+1) =& x_{DC}(k) + \frac{T_s}{C_{Bus} x_{DC}(k)} (P_B(u_B(k)) + P_{UC}(x_{UC}(k), u_{UC}(k)) \\
&+ \frac{T_s}{C_{Bus} x_{DC}(k)} (N_{Gen} x_{DC}(k) x_G(k) - x_M(k) u_M(k)/\eta_M), \\
x_G(k+1) =& x_G(k) + \frac{T_s}{\tau_{PG}} (-x_G(k) + G_{PG} u_G(k)), \\
x_M(k+1) =& x_M(k) + \frac{T_s}{H} (-\beta_M x_M(k) + u_M(k) - T_{Load}(k)),
\end{aligned} \tag{6.13}$$

where λ_ω, $\lambda_{P_{Gen}}$ and λ_{P_M} are the penalties of tracking performance of motor speed, generator power and motor power, respectively; $\lambda_{\Delta I_{PG}}$ and $\lambda_{\Delta T_M}$ are the penalties of the variations of generator output DC current and motor torque, respectively; $N_{Gen} = 2$ is the number of generator sets, and η_M is the efficiency of the motor.

The main differences and the potential impact on performance and complexity are discussed in the following remarks.

Remark 6.1: HESS-EMS is responsible for controlling the battery and UC charging/discharging, while SYS-EMS controls the entire electric propulsion system. HESS-EMS has no authority to control the generator or propulsion motor. As shown in Equations (6.10)-(6.11), comprehensive objectives, which consider the entire propulsion system performance, can be better formulated in SYS-EMS, leading to improved performance over HESS-EMS. This will be shown in the next subsection, especially when HESS is forced to operate at its limits.

Remark 6.2: Compared with SYS-EMS, HESS-EMS has the advantage of having a "plug-in" capability. When a new HESS is introduced into the existing electric ship propulsion system, HESS-EMS requires no change the existing control systems of the generator sets and propulsion motor. A further advantage of HESS-EMS is that it

has a lower computational cost than SYS-EMS.

6.2.2 Comparative Study and Simulation Results

To evaluate the proposed SYS-EMS and quantify the performance advantages introduced by system-level coordination, a comparative study is performed and the following key metrics are used for both HESS-EMS and SYS-EMS:

1. DC bus voltage variations measured by rms and maximum absolute value;
2. Motor speed variations measured by rms and maximum absolute value.
3. High frequency variations of propulsion motor torque measured by the maximum amplitude of the torque frequency spectrums in the high-frequency range (i.e., greater than 1Hz);
4. Efficiency in terms of power losses of HESS in the electrical system due to energy cycling;
5. Battery "friendliness" in terms of the time spent charging/discharging the battery with high currents.

As shown in Figure 6.15, both the HESS-EMS and SYS-EMS offer good regulation of the DC bus voltage. However, the SYS-EMS significantly reduces the torque variation with almost the same performance in motor speed tracking compared to HESS-EMS. Due to the multi-frequency characteristics of the load fluctuations, there is a trade-off among speed variation, torque variation, and power variation. Desired performance can be achieved in SYS-EMS by tuning the penalties in the cost function. When a large pulse load is applied, the coordination of the generator sets, propulsion motor, and HESS is able to address the dynamic operating conditions. As shown in Figure 6.16, when a 500KW pulse load of 1 second duration and 6 second period is applied, SYS-EMS uses all the subsystems, including the generator and propulsion

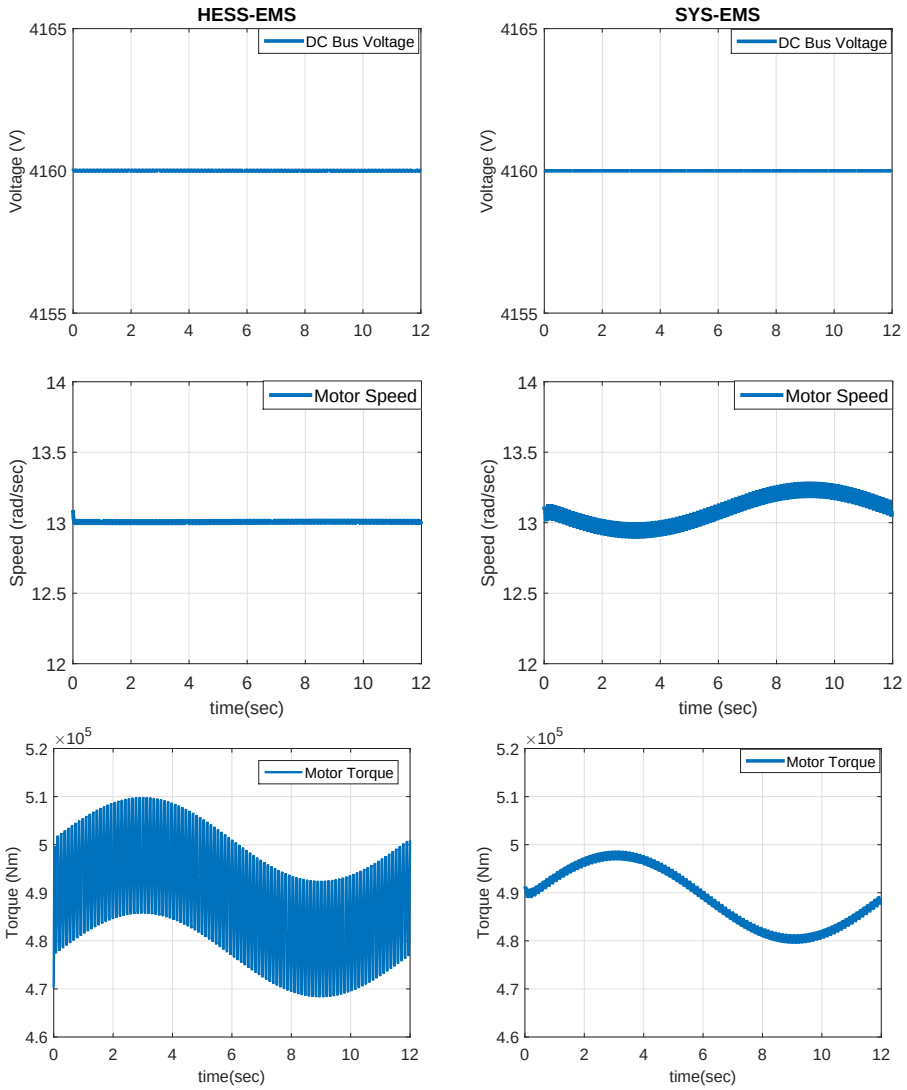

Figure 6.15: Performance of HESS-EMS and SYS-EMS at Sea State 4.

motor control, to maintain a stable DC bus voltage. Specifically, the power to the motor is reduced so that more power is directed to meet the large pulse load demand. This does lead to slightly reduced motor speed for a short time period, but it is inconsequential given the magnitude of the reduction. For HESS-EMS, since the motor control works independently, such control authority is not available and therefore large ripples occur on the DC bus, as shown in Figure 6.16.

The performance of HESS-EMS and SYS-EMS is summarized in Table 6.3. Based on the comparison study presented above, the key observations are summarized in

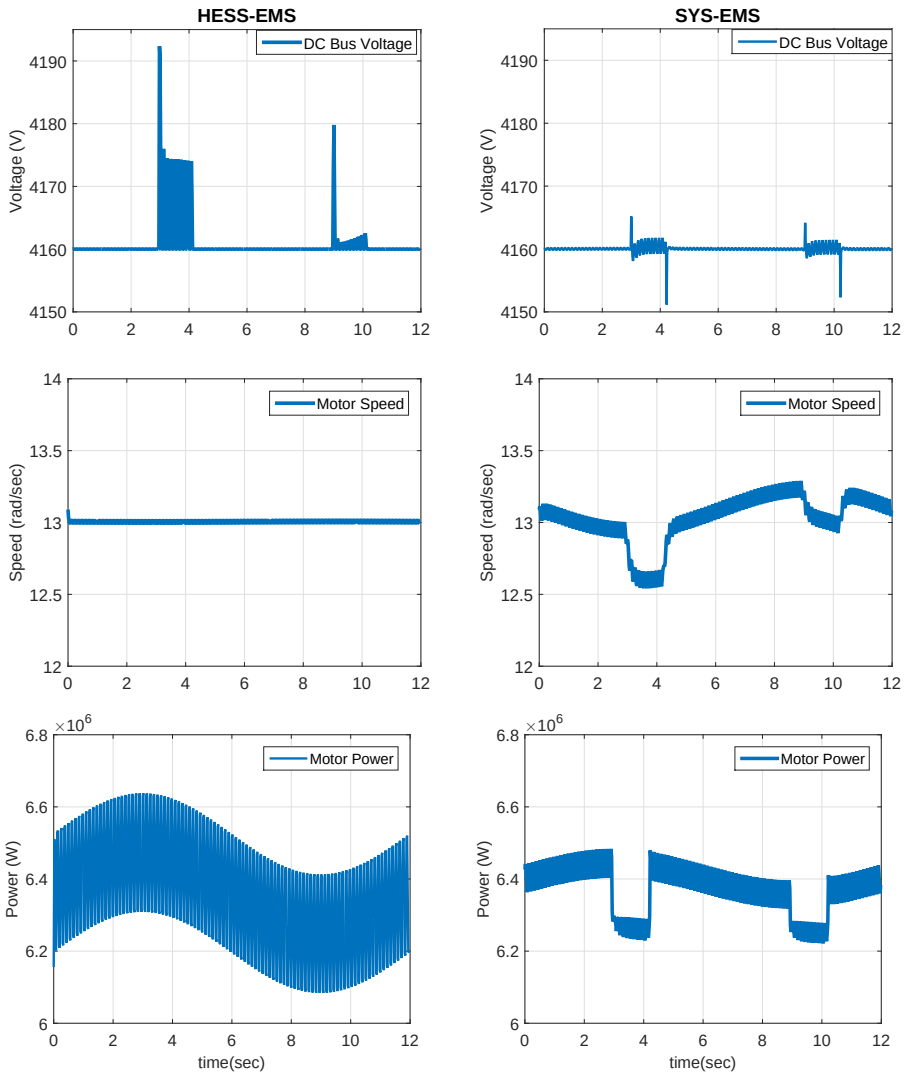

Figure 6.16: Performance of HESS-EMS and SYS-EMS with pulse power load at Sea State 4.

the following remarks.

Remark 6.3: Due the full coordination of the overall electric propulsion system, SYS-EMS has a significant advantage over HESS-EMS in terms of improving system efficiency, enhancing reliability, and reducing mechanical wear and tear. The generator sets and battery can properly charge the UC when it reaches its limits without generating large ripples on the DC bus. When the ship encounters large waves, the propulsion motor will coordinate with the generator sets and HESS to maintain a stable DC bus voltage. As shown in Figures 6.16, SYS-EMS is able to deal with

the load fluctuations and pulse power load simultaneously and achieve the desired performance.

Remark 6.4: The disadvantage of SYS-EMS compared to HESS-EMS is the high computational cost. Therefore, to implement SYS-EMS in real-time control applications, computationally-efficient optimization algorithms are needed.

The proposed two EMSs, namely HESS-EMS and SYS-EMS, effectively mitigate the propulsion load effect on the shipboard network, in terms of enhanced reliability, improved efficiency, reduced mechanical wear and tear. The study in this chapter assumes the propulsion load torque is known. However, in most marine applications, the propulsion load torque is immeasurable and unpredictable. In order to address this issue, the load torque estimation and prediction are studied in the next chapter.

6.3 Summary

In this chapter, two configurations are studied to integrate the new HESS with an existing propulsion system: a 'plug-in' configuration and an 'integrated' configuration. The trade-off between control simplicity, modularity and overall system performance is discussed. The 'plug-in' configuration provides a simple and modular control solution. The interaction of different control strategies for 'plug-in' configuration is analyzed. For the 'integrated' configuration, the integrated approach takes advantage of the predictive nature of MPC and allows the designers to judiciously coordinate the different entities of the shipboard network under constraints, thereby providing benefits to system performance. This 'integrated' strategy requires the information of propulsion-load torque, which will be studied in the next chapter.

Table 6.3: EMS performance comparison.

Sea State 4.
Operation time:1200 sec; without pulse power load

	HESS-EMS	SYS-EMS
Bus Voltage RMS Error	0.9148V	0.0005V
Bus Voltage Max Error	61.0588V	0.0015V
Motor Speed RMS Error	0.0851rad/sec	0.11rad/sec
Motor Speed Max Error	0.1004rad/sec	0.2017rad/sec
Motor Torque Variation	11.747KNm	0.799KNm
HESS Loss%	1.496%	0.3754%
IB_{high}%	0.7133%	0.0%

Sea State 6.
Operation time:1200 sec; without pulse power load

	HESS-EMS	SYS-EMS
Bus Voltage RMS Error	20.6632V	0.001V
Bus Voltage Max Error	159.1228V	0.0023V
Motor Speed RMS Error	0.0849rad/sec	0.3923rad/sec
Motor Speed Max Error	0.1036rad/sec	1.0686rad/sec
Motor Torque Variation	24.903KNm	0.83KNm
HESS Loss%	2.3391%	1.157%
IB_{high}%	5.7767%	0.0%

Sea State 4.
Operation time:12 sec; with 500KW pulse power load

	HESS-EMS	SYS-EMS
Bus Voltage RMS Error	3.1259V	0.7016V
Bus Voltage Max Error	32.3337V	8.83841V
Motor Speed RMS Error	0.0851rad/sec	0.2206rad/sec
Motor Speed Max Error	0.1004rad/sec	0.6536rad/sec
Motor Torque Variation	12.88KNm	0.96KNm
HESS Loss%	1.7602%	1.7543%
IB_{high}%	4.8333%	0.1667%

Sea State 6.
Operation time:12 sec; with 500KW pulse power load

	HESS-EMS	SYS-EMS
Bus Voltage RMS Error	3.1296V	0.6182V
Bus Voltage Max Error	28.169V	9.8445V
Motor Speed RMS Error	0.0849rad/sec	0.4301rad/sec
Motor Speed Max Error	0.1036rad/sec	0.8820rad/sec
Motor Torque Variation	12.86KNm	0.879KNm
HESS Loss%	2.3391%	1.3573%
IB_{high}%	5.7767%	0.1667%

CHAPTER VII

Load Torque Estimation and Prediction for An Electric Ship Propulsion System

In previous chapters, we have developed an integrated EMS using MPC to address the effects of the load fluctuations and achieve the desired performance. However, it is assumed that the propulsion-load torque is known and can be accurately predicted. In most marine applications, however, the propulsion-load torque is difficult to measure and includes multi-frequency fluctuations. Given the importance of the propulsion-load torque, this chapter focuses on its estimation and prediction for implementing MPC.

Load-torque estimation has been explored in a number of studies [19, 21, 22, 83, 84, 85]. In [19, 21, 22, 83], the load torque is assumed to be constant or slowly time-varying. For our problem, the load torque investigated here consists of multi-frequency fluctuation components. The disturbance observer or input observer (IO) approach presented in [84, 85], on the other hand, is not based on the assumption that the load torque is constant or slowly time-varying. Note that the input observer is also referred to as the disturbance observer in the literature, since the unknown input can be considered as a disturbance [86]. Despite the contributions of these works, the aforementioned approaches do not take advantage of the physical characteristics of the propulsion-load dynamics, especially the fast dynamics. Furthermore, those

approaches cannot be directly used to predict the future load torque, which is required for implementing MPC. Additional load predictive capabilities are therefore required.

In this chapter, we develop a model-based approach to estimate the propulsion-load torque for all-electric ships. Due to the complexity of the propulsion-load torque model, we first develop a simplified model which is able to capture the key dynamics. Because of uncertainties in the model parameters, parameter identification is used, leading to improved robustness of the control system. This model-based approach can be easily integrated with the MPC to formulate an adaptive load estimation/prediction with MPC (AMPC). In order to evaluate the proposed AMPC approach, the IO presented in [85] is used as an alternative technique to estimate the propeller-load torque. In this alternative control, linear prediction (LP) [87] is combined with IO to predict the future propulsion-load torque. A comparative study is performed to evaluate the effectiveness of the proposed AMPC in terms of minimizing the bus voltage variation, regulating the rotational speed, and reducing the high-frequency motor torque variation. The implications of accurate estimation and prediction are also illustrated and analyzed in this study.

Table 7.1: Control objectives and their mathematical expression.

Control objectives	Mathematical expression
System reliability	$min(V_d - x_{DC}(k))^2$
Thrust production	$min(\omega_d - x_M(k))^2$
System efficiency	$min(P_{Gen}^{ref} - x_{DC}(k)x_G(k))^2$
	$min(P_M^{ref} - x_M(k)u_M(k))^2$
	$min(R_B u_B^2(k) + R_{UC} u_{UC}^2(k))$
Wear-and-tear mitigation	$min(x_G(k+1) - x_G(k))^2$
	$min(u_M(k) - u_M(k-1))^2$
	$min(x_M(k+1) - x_M(k))^2$

7.1 Energy Management Strategy Formulation

7.1.1 AMPC Problem Formulation

In order to achieve enhanced system reliability, desired thrust production, improved system efficiency, and reduced wear and tear, the corresponding control objectives and their mathematical expressions are summarized in Table 7.1, where V_d is the desired bus voltage, ω_d is the desired reference speed of the propulsion motor, and P_{Gen}^{ref} and P_M^{ref} are the reference powers of the generator sets and motor, respectively.

Since the propulsion-load torque T_{Load} in (2.14) is difficult to measure for marine applications, estimation of T_{Load} is required. Furthermore, in order to implement MPC, prediction of T_{Load} in the MPC prediction windows is also required. To address the estimation and prediction of the propulsion-load torque, an adaptive load estimation/prediction with MPC is developed which minimizes a cost function subject to constraints within the prediction horizon. This can be mathematically expressed as follows:

$$P(x_0) : \min_{x:[t,t+N]\to R^5 u:[t,t+N-1]\to R^4} J(x, u, \hat{T}_{Load}) \tag{7.1}$$

where:

$$J(x, u, \hat{T}_{Load}) = \Phi(x(t+N)) + \sum_{k=t}^{t+N-1} L(x(k), u(k), \hat{T}_{Load}(k|t)), \tag{7.2}$$

subject to:

$$x(k+1) = f(x(k), u(k), \hat{T}_{Load}(k|t)), x(t) = x_0, \tag{7.3}$$

$$C(x(k), u(k)) \leq 0, \tag{7.4}$$

where $\Phi(x(N))$ and $L(x(k), u(k), \hat{T}_{Load}(k|t))$ are the terminal and instantaneous cost functions, N is the time window over which the cost will be evaluated, $C(x(k), u(k))$

represents the inequality constraints, t represents the current time, and $x(k)$, $u(k)$ are the instantaneous values of the states and inputs at time k, respectively. The instantaneous estimation of the propulsion-load torque is represented by $\hat{T}_{Load}(t|t)$, and $\hat{T}_{Load}(k|t)$ for $k = t+1, ..., t+N-1$ are the predictions of the load torque at time t.

According to the control objectives as shown in Table 7.1, the AMPC formulation takes the following form:

$$\Phi(x(N)) = \lambda_{VDC}(V_d - x_{DC}(N))^2 + \lambda_{\omega}(\omega_d - x_M(N))^2, \tag{7.5}$$

$$\begin{aligned} L(x(k), u(k), \hat{T}_{Load}(k|t)) =& \lambda_{VDC}(V_d - x_{DC}(k))^2 \\ &+ \lambda_{\omega}(\omega_d - x_M(k))^2 \\ &+ \lambda_{P_{Gen}}(P_{Gen}^{ref} - x_{DC}(k)x_G(k))^2 \\ &+ \lambda_{P_M}(P_M^{ref} - x_M(k)u_M(k))^2 \\ &+ \lambda_{HESS}(R_B u_B^2(k) + R_{UC} u_{UC}^2(k)) \\ &+ \lambda_{\Delta I_{PG}}(x_G(k+1) - x_G(k))^2 \\ &+ \lambda_{\Delta T_M}(u_M(k) - u_M(k-1))^2 \\ &+ \lambda_{\Delta\omega}(x_M(k+1) - x_M(k))^2, \end{aligned} \tag{7.6}$$

for all $k \in [t, t+N-1]$, subject to (6.12) and (6.13), where λ_{VDC}, λ_{ω}, $\lambda_{P_{Gen}}$, λ_{P_M}, λ_{HESS}, $\lambda_{\Delta I_{PG}}$, $\lambda_{\Delta T_M}$ and $\lambda_{\Delta\omega}$ are the weighting factors for the penalties of DC bus voltage variation, tracking performance of motor speed, generator and motor power, HESS losses, variations of generator output DC current, motor torque and motor speed, respectively. The estimation and prediction of propulsion load torque is addressed in the following section.

7.2 Propulsion-load Torque Estimation and Prediction

7.2.1 First Approach: Input Observer with Linear Prediction

In order to estimate the propulsion load torque, the input observer (IO) presented in [85] is used. The general propeller-motor dynamic is described by the following equation:

$$\dot{\omega} = \frac{T_M(t) - \beta_M \omega - T_{Load}(t)}{H}. \tag{7.7}$$

We define

$$\begin{aligned} u_L(t) &= T_{Load}(t)/H, \\ z_L(t) &= \frac{T_M(t) - \beta_M \omega(t)}{H}, \\ y_L(t) &= \omega(t) + \xi_L(t), \end{aligned} \tag{7.8}$$

where $\xi_L(t)$ is the measurement noise.

The unknown input $u_L(t)$ can be then estimated by the following equations [85]:

$$\begin{aligned} \hat{u}_L(t) &= \varepsilon_L(t) + \alpha_L y(t) + \phi_L(t), \\ \dot{\phi}_L &= -\alpha_L \phi_l - \alpha_L z_L, \\ \dot{\varepsilon}_L &= -\alpha_L \varepsilon_L - \alpha_L^2 y_L, \\ \hat{T}_{Load}(t) &= \hat{u}_L(t) H, \end{aligned} \tag{7.9}$$

where $\alpha_L > 0$ is the observer gain and the states of the observer are ϕ_L and ε_L.

Since the input observer cannot predict future load torque, linear prediction is used. Linear prediction incorporates the knowledge of the signal frequency spectrum (autocorrelation) to determine the linear prediction coefficients (LPCs). Only past data, which can be obtained from IO estimation results, is required for LP. To predict the load torque at time t+1, linear prediction is formulated as follows:

$$\hat{T}_{Load}(t+1|t) = \sum_{i=1}^{N_{LP}} \beta_{LP_i} \hat{T}_{Load}(t-i+1|t), \tag{7.10}$$

where N_{LP} is the prediction order, and β_{LP_i} $(i = 1, ..., N_{LP})$ are the linear prediction coefficients. The coefficients can be calculated using the Matlab function "lpc". The inputs of "lpc" are the past data and the desired prediction order. We then combine IO with LP. The algorithm can be easily implemented, as shown in Figure 7.2. However, there are several limitations of this approach, summarized in the following.

Remark 7.1: The gain α_L in (7.9) is the only parameter used to tune IO. Since the high-frequency fluctuation is at the propeller-blade frequency, i.e., around 8Hz, the minimum cut-off frequency is designed at 8Hz, leading to a minimum observer gain $\alpha_L = 50$. As shown in Figure 7.1, the phase shift at the cut-off frequency is about 45 degrees, which might significantly affect the estimation performance. In order to reduce the estimation error, the high-gain input observer is a reasonable choice if the noise can be ignored. However, noise is an issue under many conditions; the estimation performance of a high-gain observer, e.g. $\alpha_L = 400$, might be even worse than one using the minimum gain. The maximum observer gain is difficult to determine when the noise is random and unknown.

Remark 7.2: The predictive performance of LP highly depends on past data. The performance of IO directly affects LP. Furthermore, the predictive error could be accumulated as the predictive horizon extends. For example, predicting $\hat{T}_{Load}(t+2|t)$ requires the prediction value $\hat{T}_{Load}(t+1|t)$, which means the predictive error of $\hat{T}_{Load}(t+1|t)$ affects the prediction of $\hat{T}_{Load}(t+2|t)$.

Since only the general propeller-motor model (7.7) is used in this approach, the dynamics of the propeller load torque are not taken into consideration. In order to address the limitations discussed in Remarks 7.1 and 7.2, a model-based approach is required, leading to the adaptive load estimation/prediction with model predictive control discussed in the next section. The major challenge of this approach is the

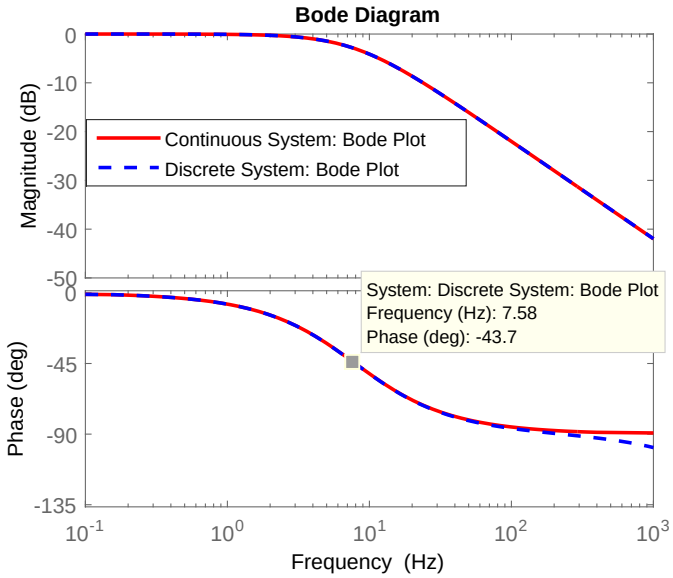

Figure 7.1: Bode plot of the input observer.

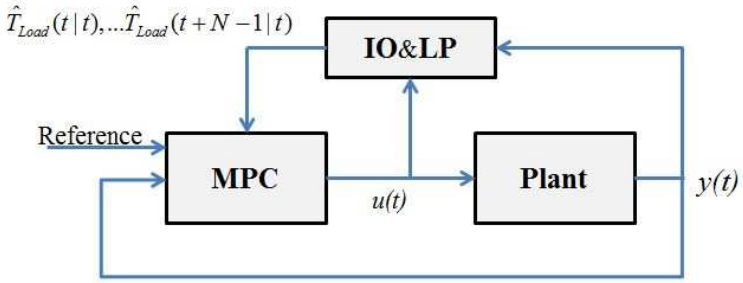

Figure 7.2: Schematic diagram of the first approach (IO-LP).

complexity of the load torque model (7.11). The focus of the next section is to develop a simplified model of (7.11), which is able to capture the key dynamics of the propeller-load torque.

7.2.2 Second Approach: Adaptive Load Estimation/Prediction with Model Predictive Control

Instead of using only the general propeller-motor model (7.7), this model can be augmented by the propeller-load torque model presented in Chapter II to provide additional useful information to estimate the load torque. This propulsion-load torque

model is expressed in the following:

$$\begin{aligned} T_{Load}(t) =& \operatorname{sgn}(n)\beta\rho n^2 D^5 f_{K_Q}\left(J_A, Pitch/D, A_e/A_o, Z, R_n\right) \\ =& \operatorname{sgn}(n)\beta\rho D^5\left(c_0 n^2 + c_1\frac{U(1-w)}{D}n\right) \\ &+ \operatorname{sgn}(n)\beta\rho D^5 c_2\left(\frac{U(1-w)}{D}\right)^2 \\ &+ \operatorname{sgn}(n)\beta\rho D^5 c_3\left(\frac{U(1-w)}{D}\right)^3\frac{1}{n}, \end{aligned} \tag{7.11}$$

where,

$$n = \omega/2\pi,$$

$$1 - w = M_0 - M_1 cos(4\theta),$$

θ is the angular position of one blade; c_i (i=0,1,2,3), M_0 and M_1 are unknown parameters; β is the loss factor; ρ is the density of water; D is the diameter of the propeller; and f_{K_Q} is the torque coefficient function. In f_{K_Q}, J_A is the advance coefficient; $Pitch/D$ is the pitch ratio; A_e/A_o is the expanded blade-area ratio, with A_e being the expanded blade area and A_o being the swept area; Z is the number of propeller blades; and R_n is the Reynolds number.

The parameters in (7.11) are usually fitted off-line. For example, parameters $c_{0,1,2,3}$ in the function f_{K_Q} are based on the fitted K_Q curves for the Wageningen B-Series Propellers [70] and the K_Q correction multiplier [71]. The multiplier in [71] is chosen to minimize the error in the range of the maximum efficiency. If the propeller is not operating in the range of maximum efficiency, the error could be significantly larger. Furthermore, the coefficients in f_{K_Q} can vary with the wear and tear of the propeller. As the operating environment changes, the parameters in the propeller-load model (7.11) can also change. Therefore, to use (7.11) for load torque estimation, online parameter identification is necessary.

In this detailed load model (7.11), six parameters $(c_0, c_1, c_2, c_3, M_0, M_1)$ are used in the nonlinear parametric model, making parameter estimation difficult. To facilitate

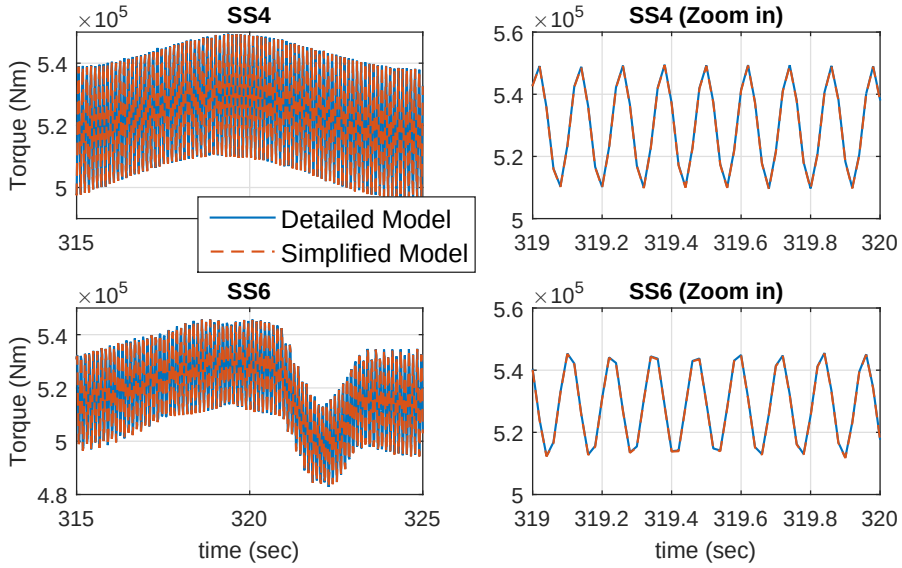

Figure 7.3: Outputs of the detailed and simplified propeller-load torque models at sea state 4 (top) and sea state 6 (bottom).

online parameter estimation, we propose the following simplified model (7.12), whose derivation is given in the Appendix (Section 7.5).

$$T_{Load} \approx \bar{C}_1 + \bar{C}_2 cos(4\theta) + \bar{C}_3(n - n_{ref}). \tag{7.12}$$

The output of the detailed propeller-load torque model and the simplified model (7.12) at sea states 4 and 6 are shown in Figure 7.3.

With the combination of (7.7) and (7.12), the new propeller-motor model is developed in the following:

$$\dot{\omega} = \frac{T_M(t) - \beta_M \omega - (\bar{C}_1 + \bar{C}_2 cos(4\theta) + \bar{C}_3 \Delta\omega/2\pi)}{H}. \tag{7.13}$$

For parameter estimation, a parametric model is defined as follows:

$$z_{par} = C_{par}^{*T} \phi_{par}, \tag{7.14}$$

where

$$z_{par} = \left\{ \frac{\lambda_{par}}{s + \lambda_{par}} \right\} \left(\dot{\omega} - \frac{1}{H}(T_M - \beta_M \omega) \right),$$

$$C^*_{par} = [\bar{C}_1 \;\; \bar{C}_2 \;\; \bar{C}_3]^T,$$

$$\phi_{par} = \left\{ \frac{-\lambda_{par}}{s + \lambda_{par}} \right\} [1 \;\; cos(4\theta) \;\; \Delta\omega/2\pi]^T,$$

λ_{par} is the filter gain, and $\{\cdot\}$ represents the dynamic operator of the filter, whose transfer function is $(\cdot)$. The filter is introduced to avoid taking numerical derivatives in estimation.

The normalized gradient algorithm is chosen as the adaptive law and presented in the following [88]:

$$C_{par}(t) = C_{par}(t-1) + \frac{T_s \Gamma \phi_{par}(t) \epsilon_{par}}{1 + \phi_{par}(t)^T \phi_{par}(t)},$$

where

$$\epsilon_{par} = z_{par}(t) - C_{par}(t-1)^T \phi_{par}(t),$$

and $\Gamma = \Gamma^T$ is a positive-definite matrix satisfying the criteria that the real part of its eigen-values are between $(0, 2/T_s)$, which affects how fast C_{par} updates.

The speed variation within the predictive horizon is assumed to be very small, i.e., $x_M(t+N-1) \approx x_M(t+N-2) \approx ... \approx x_M(t)$. This results in an estimation of the future propeller-blade position at time k as follows:

$$\theta(k) = \theta(t) + (k-t) T_s x_2(t). \quad (t \leq k \leq t+N-1)$$

Therefore, the schematic diagram of the proposed AMPC is shown in Figure 7.4, and the new propeller-motor dynamic is expressed in the following:

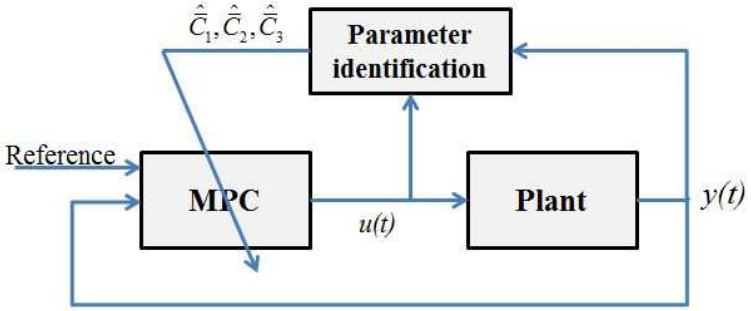

Figure 7.4: Schematic diagram of the AMPC controller.

Table 7.2: Performance metrics.

Performance	Mathematical expression
"Voltage Regulation"	$\sqrt{\frac{\sum_{k=0}^{N_T}(V_d - x_{DC}(k))^2}{N_T+1}}$
"Speed Regulation"	$\sqrt{\frac{\sum_{k=0}^{N_T}(\omega_d - x_M(k))^2}{N_T+1}}$
"Gen Power Tracking"	$\sqrt{\frac{\sum_{k=0}^{N_T}(P_{Gen}^{ref} - x_{DC}(k)x_G(k))^2}{N_T+1}}$
"Motor Power Tracking"	$\sqrt{\frac{\sum_{k=0}^{N_T}(P_M^{ref} - x_M(k)u_M(k))^2}{N_T+1}}$
"HESS Losses Reduction"	$\sqrt{\frac{\sum_{k=0}^{N_T}(R_B u_B^2(k) + R_{UC} u_{UC}^2(k))}{N_T+1}}$
"Gen Oscillation Reduction"	$\sqrt{\frac{\sum_{k=0}^{N_T}(x_G(k+1) - x_G(k))^2}{N_T+1}}$
"Torque Oscillation Reduction"	$\sqrt{\frac{\sum_{k=0}^{N_T}(u_M(k) - u_M(k-1))^2}{N_T+1}}$
"Speed Oscillation Reduction"	$\sqrt{\frac{\sum_{k=0}^{N_T}(x_M(k+1) - x_M(k))^2}{N_T+1}}$
"Total Cost"	$\sqrt{\frac{\sum_{k=0}^{N_T} L(x(k), u(k), T_{Load}(k))}{N_T+1}}$

$$
\begin{aligned}
x_M(k+1) =& x_M(k) - \frac{T_s \bar{C}_3}{2\pi H}(x_M(k) - \omega_d) \\
&+ \frac{T_s}{H}(u_M(k) - \beta_M x_M(k) - \bar{C}_1) \\
&- \frac{T_s}{H}\bar{C}_2 cos(4(\theta(t) + (k-t)T_s x_M(t))),
\end{aligned}
\tag{7.15}
$$

for all $k \in [t, t+N-1]$.

7.3 Performance Evaluation and Discussion

According to the control objectives, the performance metrics are presented in Table 7.2, where N_T equals $[(t_T - t_0)/T_s]$, with $[\cdot]$ representing integer rounding, t_0 and t_T are the initial and final values of the time period being investigated, and $L(x(k), u(k), T_{Load}(k))$ represents the cost function in Equation (7.6). In order to evaluate the proposed approaches to load torque estimation and prediction, the results obtained by six cases have been studied and analyzed in this section. These six cases are described in the following:

- Case 1 "Ideal": In this case, the detailed propulsion-load torque model (7.11) without any uncertainty is used to obtain the load torque. Nonlinear MPC uses the perfect model to predict the future load torque in its optimization. Because there is no uncertainty in this case, it is referred to as "Ideal".

- Case 2 "Frozen prediction": In this case, the instantaneous load torque is obtained from the load torque model (7.11) without any uncertainty. Compared to Case 1, the future load torque used in the MPC is assumed to be same as the instantaneous load torque, i.e., $T_{Load}(t+N-1|t) = T_{Load}(t+N-2|t) = ... = T_{Load}(t|t)$, so called "Frozen prediction".

- Case 3 "LP-Only": Different from Case 2, the future load torque in this case is predicted using LP. The true load torque is used as the instantaneous load torque.

- Case 4 "IO-Frozen prediction": In this case, the input observer is used, instead of the true load torque. The future load torque is assumed to be the same as the IO estimation.

- Case 5 "IO-LP": The first approach, i.e., IO combined with LP, is used in this case.

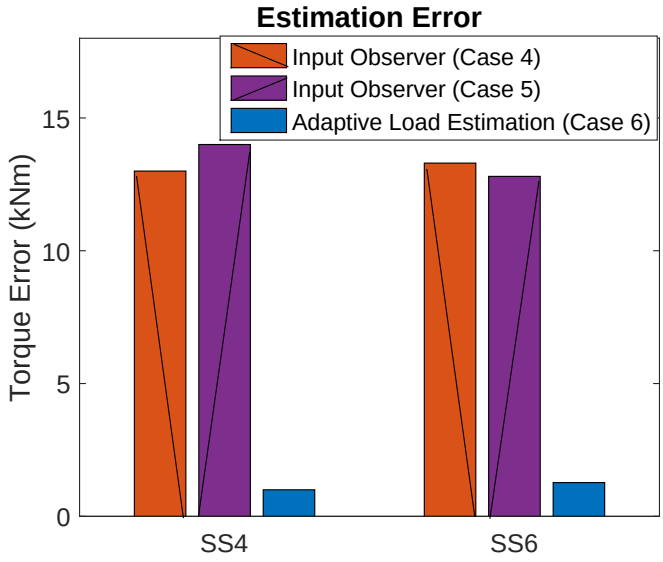

Figure 7.5: Estimation error of the adaptive load estimation and input observer.

- Case 6 "AMPC": This case is the proposed AMPC.

We first evaluate the estimation performance. Among these six cases, Cases 4, 5, and 6 require estimation of the load torque. As shown in Figure 7.5, adaptive load estimation has better estimation performance than the input observer. The reason is that more propeller-load information is taken into consideration in this adaptive approach.

The key performance metrics and results are presented in Table 7.3. The performance results of each case are normalized by Case 1. The smaller value represents the better performance. Note that the performance of Cases 2-6 from best to worst are colored in the following sequence: **blue**, **green**, **yellow**, **brown** and **red**. The degraded performance (%) is defined as the performance of Case 2 5 in Table 7.3 minus 1 (as all of the performance are normalized by Case 1), and then times 100%.

As can be seen in Table 7.3, the performance of Case 6 is the closest to Case 1. Case 1 uses the accurate detailed propeller-load model and takes its dynamics into consideration, leading to the best performance among all of the investigated cases. The "Total Cost" in the performance metrics represents the overall performance,

Table 7.3: Performance comparison.

Sea State 4.

Performance Metrics	Case 1	Case 2	Case 3	Case 4	Case 5	Case 6
"Voltage Regulation"	1	27.77	27.76	28.15	28.07	1.036
"Speed Regulation"	1	1.043	1.043	1.057	1.057	0.995
"Gen Power Tracking"	1	1.095	1.057	1.251	1.179	1.148
"Motor Power Tracking"	1	1.116	1.162	1.154	1.185	1.151
"HESS Losses Reduction"	1	1.185	1.189	1.247	1.227	1.184
"Gen Oscillation Reduction"	1	1.055	1.011	1.384	1.286	0.985
"Torque Oscillation Reduction"	1	2.803	1.792	3.067	2.609	2.172
"Speed Oscillation Reduction"	1	1.186	1.178	1.198	1.194	1.025
"Total Cost"	**1**	1.412	1.335	1.456	1.414	1.106

Sea State 6.

"Bus Regulation"	1	24.63	24.61	24.97	24.97	1.328
"Speed Regulation"	1	1.032	1.029	1.045	1.045	1.027
"Gen Power Tracking"	1	1.267	1.254	1.438	1.318	1.241
"Motor Power Tracking"	1	1.147	1.144	1.163	1.151	1.099
"HESS Losses Reduction"	1	1.166	1.174	1.189	1.197	1.194
"Gen Oscillation Reduction"	1	1.307	1.578	2.167	1.649	1.128
"Torque Oscillation Reduction"	1	2.206	1.590	2.376	2.178	1.230
"Speed Oscillation Reduction"	1	1.216	1.196	1.246	1.242	1.052
"Total Cost"	**1**	1.123	1.085	1.149	1.130	1.009

which takes all of the other metrics along with their priorities (i.e., their weighting factors) into consideration. According to "Total Cost", the performance from the best to the worst are Case 1 ("Ideal"), Case 6 ("AMPC"), Case 3 ("LP-Only"), Case 2 ("Frozen prediction"), Case 5 ("IO-LP"), and Case 4 ("IO-Frozen prediction") at both sea states 4 and 6. Based on the performance comparison, the key observations are presented in the following *Remarks*.

Remark 7.3 (Effects of load prediction): Cases 1, 2 and 3 all assume perfect load estimation at time t, but use different load predictions. Case 1 takes the load dynamics into consideration, and Case 3 uses the signal spectrum (correlation) information to predict future torque, while Case 2 uses none of these, leading to the worst performance of the three cases. The "Total Cost" performance degradation of Cases 2 and 3 compared to Case 1 is shown in Figure 7.6. Another comparative result can be shown between Cases 4 and 5. Both Cases 4 and 5 use the input observer to estimate $\hat{T}_{load}(t|t)$, but differ in the prediction scheme. The "Total Cost" degradation of Cases 4 and 5 compared to Case 1 is shown Figure 7.7. Note that the difference between

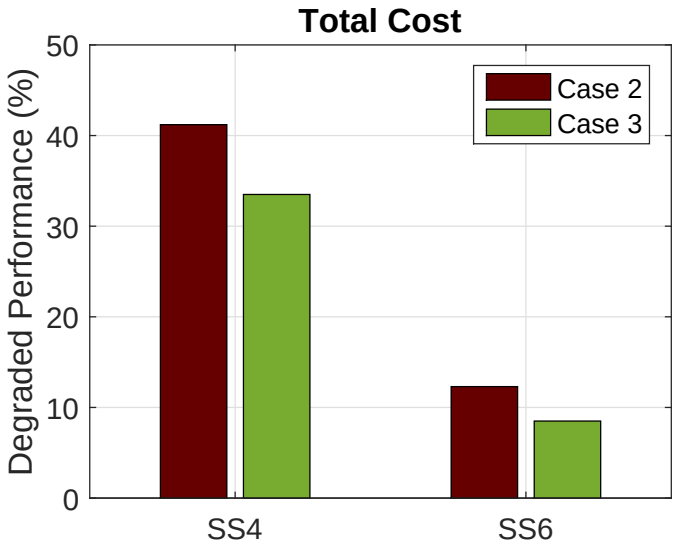

Figure 7.6: Cases 2 and 3 degraded "Total Cost" performance compared to Case 1.

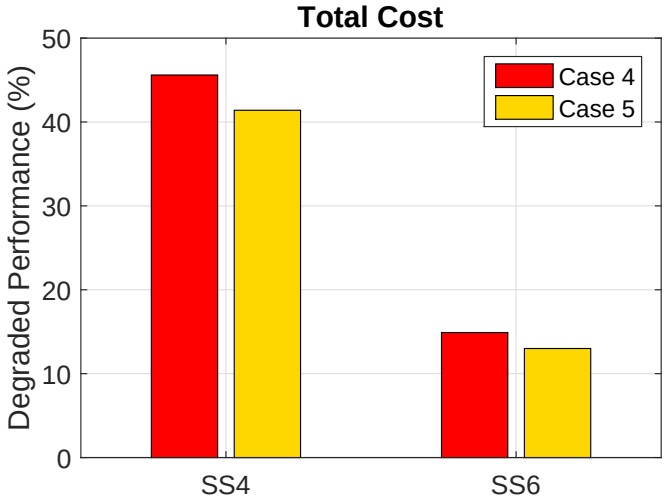

Figure 7.7: Cases 4 and 5 degraded "Total Cost" performance compared to Case 1.

Cases 4 and 5 is smaller than that between Cases 2 and 3, because the estimation error in Case 5 influences the prediction performance.

Remark 7.4 (Effects of load estimation): The difference between Case 2 and Case 4 is in the load torque estimation, where the former uses the accurate load torque model but the latter employs an IO to estimate the load torque. Case 2 outperforms Case 4 in most of the performance metrics. Their "Total Cost" performance is shown

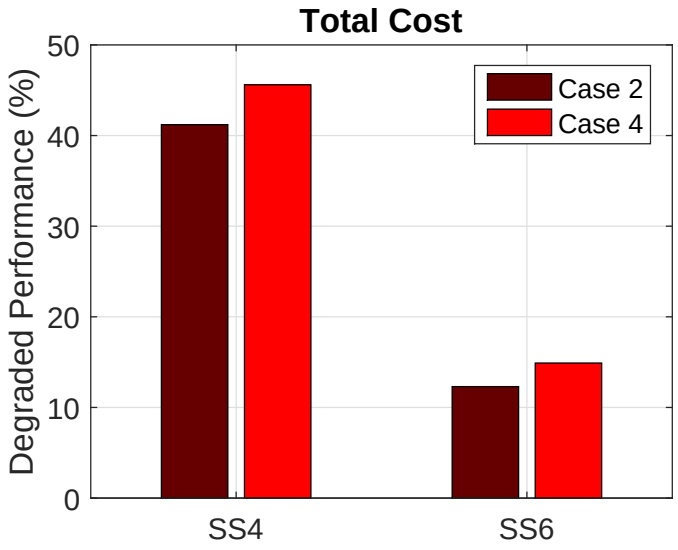

Figure 7.8: Cases 2 and 4 degraded "Total Cost" performance compared to Case 1.

in Figure 7.8. Similarly, Case 3 and Case 5 use the same prediction method, but have different load estimation. As shown in Figure 7.9, the difference between Cases 3 and 5 is larger than that between Cases 2 and 4. This is because the estimation affects not only the instantaneous information, but also the prediction in Cases 3 and 5. Case 1 has better performance than Case 6 as expected, due to the uncertainties in the dynamic model used for AMPC. These comparisons demonstrate that load torque estimation plays a key role in achieving good performance.

Remark 7.5 (Effects of data-based LP): Except for Cases 1 and 6, Case 3 has the best performance among the remaining 4 cases. Even though Case 3 only has the data-based load predictor, the prediction still contributes some benefits, especially with regard to reducing wear and tear. As shown in Figure 7.10, the metric "Torque Oscillation Reduction" demonstrates that Case 3 can achieve almost the same small motor torque variations as Case 6. Moreover, Case 3 outperforms Cases 2, 4 and 5 in terms of metrics "Gen Oscillation Reduction" and "Speed Oscillation Reduction", as shown in Table 7.3, further demonstrating the benefits of LP in performance metrics of reducing the wear and tear of the motor and generator sets. Compared to Case 3,

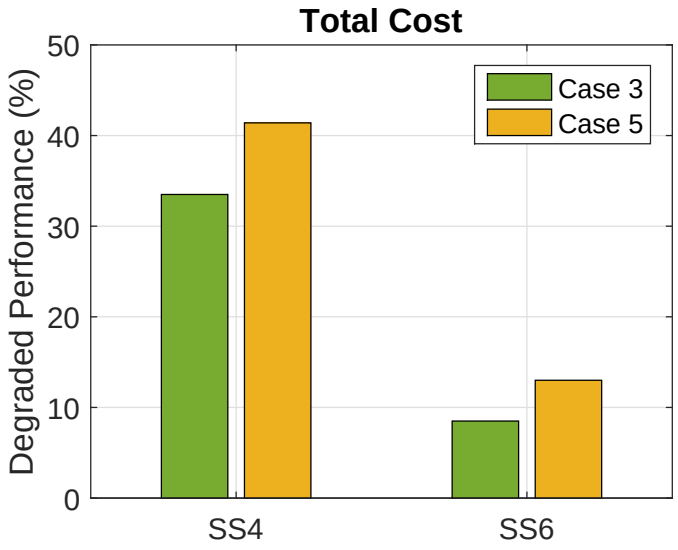

Figure 7.9: Cases 3 and 5 degraded "Total Cost" performance compared to Case 1.

Case 5 also uses LP to predict future torque. However, the estimation error of the input observer affects the prediction performance, as discussed in *Remark 7.2*. As can be seen, at sea state 4, Case 5 can achieve performance similar to Case 2. At sea state 6, the performance of Case 5 is worse than Case 2. This comparison illustrates that the load torque estimation is essential to improve the performance of data-based LP.

Remark 7.6 (Effects of adaptation): Case 6 is the only case that achieves competitive performance to Case 1. This is because only these two cases truly capture the load dynamics by using the propulsion-load torque model, thereby maintaining the motor and generator sets working around the reference points through coordination of subsystems. Without the ability to capture the load torque dynamics, however, other cases need the assistance of the motor and generator sets to mitigate the bus voltage variations, leading to degraded system efficiency and increased wear and tear. In order to evaluate the effects of adaptation, a comparative study is performed between Case 6 and Case 1 with 2% modeling errors (2%Err), where 2% modeling errors are added on c_0 and M_0 (which have the most significant effects in the propulsion-load

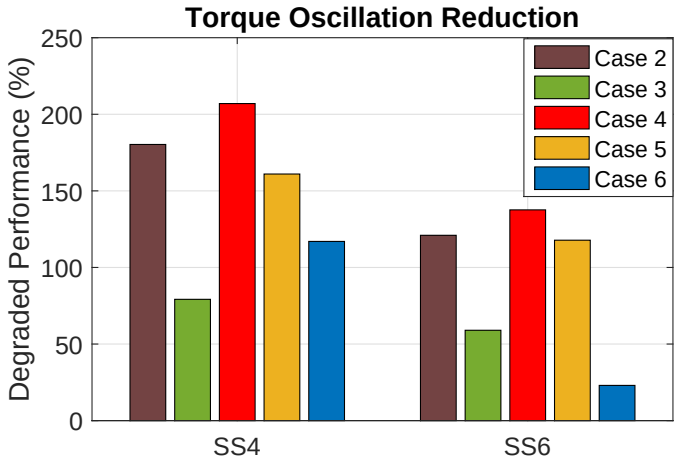

Figure 7.10: Cases 2-6 degraded "Torque Oscillation Reduction" performance compared to Case 1.

torque model). As shown in Table 7.4, these 2% modeling errors (without adaptation) can cause "Total Cost" 100% and 40% higher than Case 6 (with adaptation) at sea state 4 and 6, respectively. Moreover, the performance of 2%Err is even much worse than Case 5 (IO-Only). The key factors that renders favorable performance of AMPC are summarized in the following:

- The foundation of AMPC is a well-developed simplified model that captures the essential dynamics of the load torque. With accurate parameter identification, AMPC can predict the future load torque much better than LP.

- When the load torque dynamic model is integrated into the MPC controller, AMPC truly takes the load torque dynamic into consideration, resulting in the unique advantage of AMPC compared to the other 4 cases (Case 2, 3, 4 and 5).

Remark 7.7 (Effects of weighting factors): The weighting factors can undoubtedly influence the performance of the proposed AMPC. Each weighting factor λ assigns a relative priority to a performance aspect. As the main objectives, the system reliability and thrust production have the highest priority. The weighting factor can be tuned with emphasis being placed on different performance attributes, such as

Table 7.4: Performance comparison: Case 6 vs. Case 1 with 2% modeling error.

Performance Metrics	SS4		SS6	
	Case 6	2% ERR	Case 6	2% ERR
"Voltage Regulation"	**1.036**	**11.26**	**1.328**	**9.125**
"Speed Regulation"	**0.995**	**2.074**	**1.027**	**1.585**
"Gen Power Tracking"	**1.148**	**3.226**	**1.241**	**1.827**
"Motor Power Tracking"	**1.151**	**1.598**	**1.099**	**7.829**
"HESS Losses Reduction"	**1.184**	**3.438**	**1.194**	**1.502**
"Gen Oscillation Reduction"	**0.985**	**4.038**	**1.128**	**2.885**
"Torque Oscillation Reduction"	**2.172**	**1.467**	**1.230**	**1.155**
"Speed Oscillation Reduction"	**1.006**	**1.014**	**1.052**	**1.02**
"Total Cost"	**1.106**	**2.190**	**1.009**	**1.410**

Table 7.5: Performance comparison: weighting factor effects.

Sea State 4.

Performance Metrics	Case 6	*Test 1*	*Test 2*
"Voltage Regulation"	**1.036**	**1.040**	**7.882**
"Speed Regulation"	**0.995**	**1.210**	**1.168**
"Gen Power Tracking"	**1.148**	**1.064**	**6.634**
"Motor Power Tracking"	**1.151**	**1.0185**	**0.697**
"HESS Losses Reduction"	**1.184**	**1.023**	**0.553**
"Gen Oscillation Reduction"	**0.985**	**1.075**	**7.522**
"Torque Oscillation Reduction"	**2.172**	**0.271**	**3.928**
"Speed Oscillation Reduction"	**1.025**	**1.006**	**1.065**

Sea State 6.

"Bus Regulation"	**1.328**	**1.395**	**6.689**
"Speed Regulation"	**1.027**	**1.461**	**1.275**
"Gen Power Tracking"	**1.241**	**1.150**	**3.941**
"Motor Power Tracking"	**1.099**	**0.980**	**0.449**
"HESS Losses Reduction"	**1.194**	**1.017**	**0.390**
"Gen Oscillation Reduction"	**1.128**	**1.188**	**1.541**
"Torque Oscillation Reduction"	**1.230**	**0.418**	**1.314**
"Speed Oscillation Reduction"	**1.052**	**1.140**	**1.034**

reducing wear-and-tear and improving the efficiency of different subsystems. One metric can be improved by tuning its weighting factor, but other metrics could be negatively affected. Two tests are studied to demonstrate how the weighting factors affect the performance. These two tests are described in the following:

- *Test 1*: $10\lambda_{\Delta T_M}$ is used in this test to further reduce the motor torque oscillations.

- *Test 2*: $10\lambda_{HESS}$ is used with emphasis on improving the efficiency of HESS.

As shown in Table 7.5, the motor torque oscillation has been significantly reduced by increasing the weighting factor $\lambda_{\Delta T_M}$ in Test 1. As shown in Figures 7.11, there

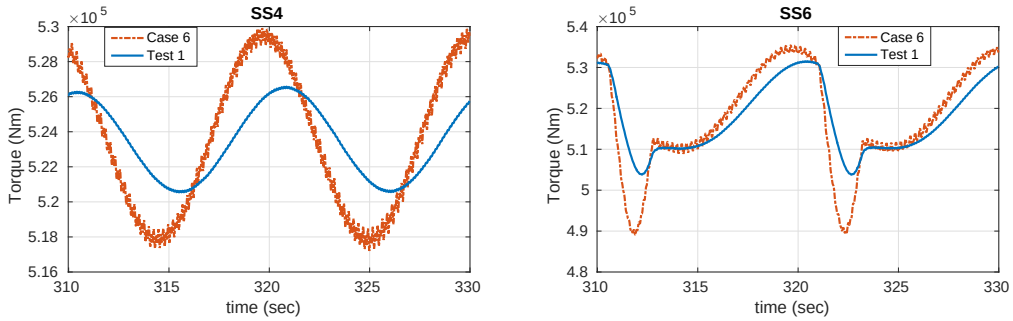

Figure 7.11: Torque comparison at sea states 4 and 6: Case 6 vs. Test 1.

is almost no motor torque oscillation in Test 1. Similarly, the losses of HESS are significantly reduced in Test 2. However, the high weighting factor λ_{HESS} forces the HESS to operate only at very low currents, leading to a loss of ability in isolating the load fluctuations from the DC bus. This causes negative effects on most of other performance metrics. Test 2 also provides the insights into the importance of HESS on mitigating the effect of the load fluctuations.

7.4 Summary

In this chapter, load torque estimation and prediction for implementing MPC-based energy management is addressed. This chapter develops a new energy management strategy, AMPC, to integrate power generation, electric motor, and hybrid energy storage control for electric ship propulsion systems in order to address the effects of propulsion-load fluctuations in the shipboard network. In order to evaluate the proposed AMPC, an alternative control is developed by integrating the input observer with linear prediction into the MPC strategy. Compared to the alternative approach, the proposed AMPC achieves much better performance in terms of improved system efficiency, enhanced reliability, improved thrust production, and reduced mechanical wear and tear. In addition to the alternative control, other cases are studied in this chapter to illustrate the importance of the load estimation and prediction.

7.5 Appendix of Chapter VII: Derivation of simplified propulsion-load model

Considering the propeller load torque model of (7.11) with $\bar{c}_i = \text{sgn}(n)\beta\rho D^5 c_i \left(\frac{U}{D}\right)^i$, $(i = 0, 1, 2, 3)$ and $1 - w = M_0 - M_1 cos(4\theta)$, we have the derivation of the simplified model (7.12) presented in the following:

$$
\begin{aligned}
T_{Load} =& \bar{c}_0 n^2 + \bar{c}_1(1-w)n + \bar{c}_2(1-w)^2 + \bar{c}_3(1-w)^3\frac{1}{n} \\
=& \bar{c}_0 n^2 + \bar{c}_1 M_0 n + \bar{c}_2(M_0^2 + 0.5M_1^2) + \frac{\bar{c}_3}{n}(M_0^3 + 1.5M_0M_1^2) \\
& - \left(\bar{c}_1 M_1 n + 2\bar{c}_2 M_0 M_1 + 3\frac{\bar{c}_3}{n} M_1 M_0^2\right) cos(4\theta) \\
& + \left(0.5\bar{c}_2 M_1^2 + 1.5\frac{\bar{c}_3}{n} M_0 M_1^2\right) cos(8\theta) - \bar{c}_3 M_1^3 cos(4\theta)^3 \\
\approx& \bar{c}_0 n^2 + \bar{c}_1 M_0 n + \bar{c}_2(M_0^2 + 0.5M_1^2) + \frac{\bar{c}_3}{n}(M_0^3 + 1.5M_0M_1^2) \\
& - \left(\bar{c}_1 M_1 n + 2\bar{c}_2 M_0 M_1 + 3\bar{c}_3 M_1 M_0^2 \frac{1}{n}\right) cos(4\theta) \\
\approx& \bar{c}_0(n_{ref}^2 + 2n_{ref}\Delta n) + \bar{c}_1 M_0(n_{ref} + \Delta n) \\
& + \bar{c}_2(M_0^2 + 0.5M_1^2) + \bar{c}_3\frac{1}{n_{ref}}(M_0^3 + 1.5M_0M_1^2) \\
& - (\bar{c}_1 M_1(n_{ref} + \Delta n) + 2\bar{c}_2 M_0 M_1) cos(4\theta) \\
& - 3\bar{c}_3 M_1 M_0^2 \frac{1}{n_{ref}} cos(4\theta) \\
=& \bar{C}_1 + \bar{C}_2 cos(4\theta) + \bar{C}_3\Delta n + \bar{C}_4 \Delta n cos(4\theta) \\
\approx& \bar{C}_1 + \bar{C}_2 cos(4\theta) + \bar{C}_3\Delta n.
\end{aligned}
$$

where,

$$\bar{C}_1 = \bar{c}_0 n_{ref}^2 + \bar{c}_1 M_0 n_{ref} + \bar{c}_2 (M_0^2 + 0.5 M_1^2) + \bar{c}_3 \frac{1}{n_{ref}} (M_0^3 + 1.5 M_0 M_1^2),$$

$$\bar{C}_2 = -(\bar{c}_1 M_1 n_{ref} + 2\bar{c}_2 M_0 M_1 + 3\bar{c}_3 M_1 M_0^2 \frac{1}{n_{ref}}),$$

$$\bar{C}_3 = 2 n_{ref} \bar{c}_0 + \bar{c}_1 M_0,$$

$$\bar{C}_4 = -\bar{c}_1 M_1,$$

$$\Delta n = n - n_{ref}.$$

The first step of simplification is to ignore the high-frequency terms, i.e., the terms $\left(0.5\bar{c}_2 M_1^2 + 1.5\bar{c}_3 M_0 M_1^2 \frac{1}{n}\right) cos(8\theta) - \bar{c}_3 M_1^3 cos(4\theta)^3$, which are greater than the propeller blade frequency. This is because the amplitudes of these high-frequency terms are much smaller than other terms, and are usually filtered significantly by the inertia of the propeller. The second step is to linearize the load torque model around the reference speed.

In this linearized model, the component $\bar{C}_4 \Delta n cos(4\theta)$ only contains the variation terms, such as M_1, Δn, $cos(4\theta)$, and can be considered as a high order component. Because $\bar{C}_4 \Delta n cos(4\theta)$ is much smaller than other components, i.e., $\bar{C}_1$, $\bar{C}_2 cos(4\theta)$ and $\bar{C}_3 \Delta n$, $\bar{C}_4 \Delta n cos(4\theta)$ can also be ignored. Finally, the linearized model $\bar{C}_1 + \bar{C}_2 cos(4\theta) + \bar{C}_3 \Delta n$ has only three unknown parameters. According to the time-scale separation approach, these three parameters are assumed to be slowly time-varying.

CHAPTER VIII

Experimental Implementation of Real-time Model Predictive Control

In this chapter, we implement a real-time model predictive controller (MPC) on a physical testbed, namely the Michigan Power and Energy Lab (MPEL) Advanced Electric Drive with Hybrid Energy Storage (AED-HES) testbed described in Chapter III, and evaluate the effectiveness of real-time MPC. Given the multi-frequency characteristic of the load fluctuations, a filter-based strategy is used as a baseline control to demonstrate the benefits of the proposed MPC. The objective of the real-time MPC is to address the shipboard load fluctuations, including pulse power load and propulsion load fluctuations, and validate the effectiveness of the proposed energy management strategy (EMS) on a physical testbed. The battery with ultra-capacitor (UC) hybrid energy storage system (HESS) configuration is considered in this chapter. In order to achieve real-time feasibility, three different efforts have been made:

- Modifying MPC formulation: the CC-MPC with SOC reference is used to achieve the desired performance with a relatively short predictive horizon.
- Developing efficient optimization solver: An integrated perturbation analysis and sequential quadratic programming (IPA-SQP) algorithm [89, 90] is used to solve the optimization problem with high computational efficiency.

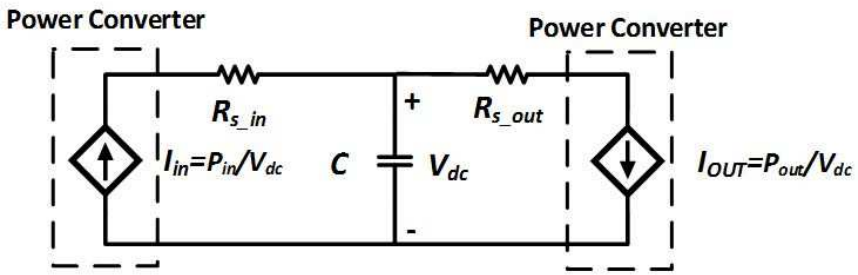

Figure 8.1: Simplified DC bus dynamic model of the AED-HES test-bed.

- Exploiting hardware: a multi-core structure is used for the real-time system controller to guarantee system signal synchronization and separate system-level and component-level controls, thereby increasing the real-time capabilities.

8.1 Problem Formulation

In DC shipboard networks, the DC bus voltage can be used to identify the stability of the DC ship power system [91]. The AED-HES test-bed differs from other DC micro-grids as there is no LC filter between the DC bus and power converters. Such a filter can greatly impact the stability of DC micro-grids [92]. However, without these filters there is only a bus capacitor on the DC bus, as shown in Fig.8.1 (simplified DC bus dynamic model). This configuration only requires balanced input and output power to maintain a stable bus voltage. Therefore, the first control objective is system reliability, which is validated by a stable DC bus voltage. In this experiment, the desired DC voltage is chosen to be 200V.

The second control objective is system efficiency. The plug-in configuration described in Chapter V is considered in this chapter. We assume the motor is working at the nominal operating point and the generator sets provide the average power. Since there is no generator in our testbed, we use a DC/DC converter to provide the average power to the DC bus in order to emulate the generator sets. In order to improve the system efficiency, the losses of the HESS must be minimized. Furthermore,

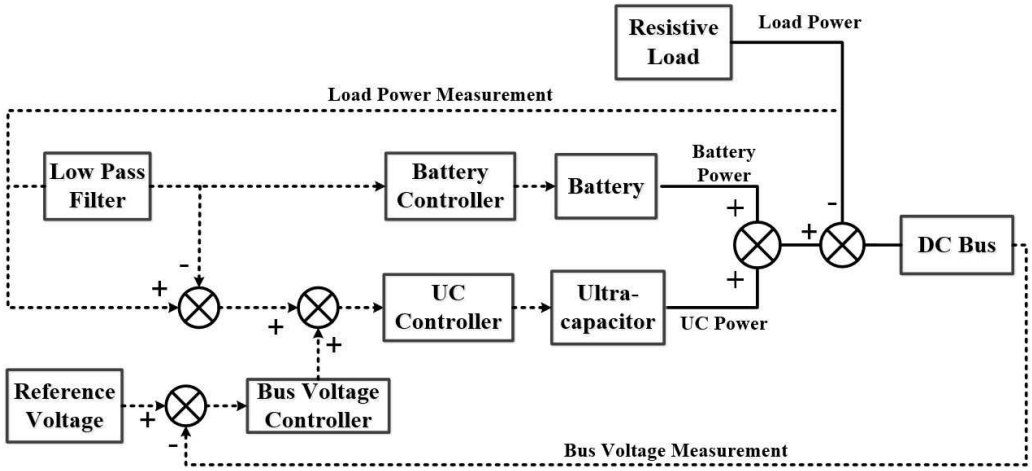

Figure 8.2: Schematic of the filter-based control.

as discussed in Chapter V, a long self-sustained time is preferred to take advantage of the battery's high energy density. The battery power is used to ensure the UC is operating in its high-efficiency range. In this experiment, the battery power keeps the UC operating around 145V.

Finally, the third control objective is to extend the battery life cycle. Along with the reduction of battery life cycle, the battery degradation causes its capacity to decrease and its resistance to increase [79, 93]. The battery C-rate and usage are two important factors for battery life cycle [94, 95]. In this chapter, the battery peak and RMS currents are used to represent high C-rate operation and battery usage.

The control objectives are therefore summarized as follows:

- System reliability: maintain the DC bus voltage at 200V.
- System efficiency: Minimize HESS losses.
- Extend battery life cycle: reduce battery peak and RMS currents.

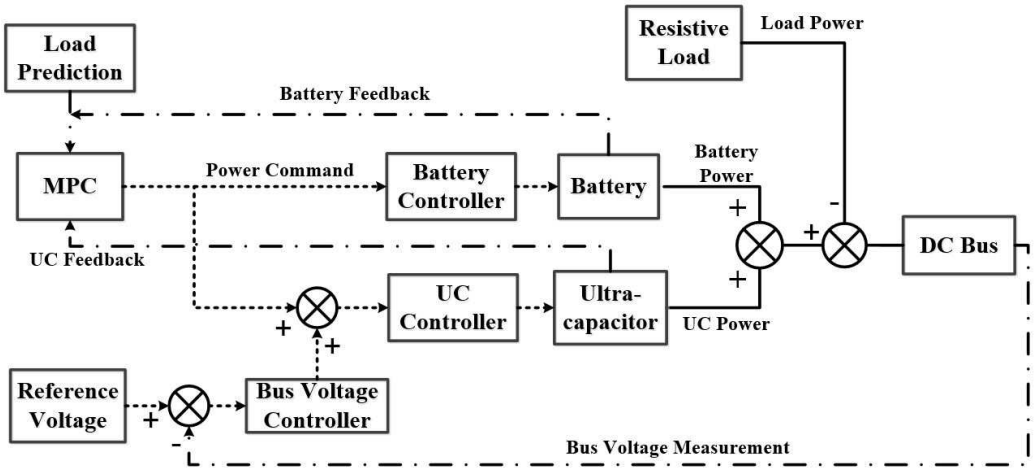

Figure 8.3: Schematic of the real-time MPC.

8.2 System-level Controller Development: Energy Management Strategy

In Chapter III, experimental results show that the filter-based control strategy outperforms the independent PI control strategy. In this chapter, the filter-based strategy is used as a baseline control to evaluate the effectiveness of the proposed real-time MPC strategy. The schematic of the filter-based controller is shown in Fig. 8.2. In order to perform a fair comparison, the same voltage regulator is used in the real-time MPC. The schematic of the real-time MPC is shown in Fig. 8.3. In order to achieve the control objectives discussed in previous section, the optimization problem is formulated as follows:

$$\begin{aligned} J_{HESS_{B/UC}}(x(k),u(k)) = &\sum_{k=0}^{N}(1-\lambda)(P_{FL}(k)-P_B(k)-P_{UC}(k))^2 \\ &+\lambda(N_B R_B u_B^2(k)+N_{UC}R_{UC}u_{UC}^2(k)) \\ &+\gamma_{UC_{SOC}}(x_{UC}(k)-SOC_{UC_d})^2, \end{aligned} \tag{8.1}$$

subject to the constraints:

$$\begin{aligned} 20\% \leq x_B \leq 90\%, \\ 50\% \leq x_{UC} \leq 99\%, \\ -30A \leq u_B \leq 30A, \\ -30A \leq u_{UC} \leq 30A, \end{aligned} \tag{8.2}$$

$$\begin{aligned} \begin{bmatrix} x_B(k+1) \\ x_{UC}(k+1) \end{bmatrix} = \begin{bmatrix} 1 & 0 \\ 0 & 1 \end{bmatrix} \begin{bmatrix} x_B(k) \\ x_{UC}(k) \end{bmatrix} \\ + \begin{bmatrix} \frac{T_s}{3600 Q_B} & 0 \\ 0 & \frac{T_s}{V_{max} C_{UC}} \end{bmatrix} \begin{bmatrix} u_B(k) \\ u_{UC}(k) \end{bmatrix}. \end{aligned} \tag{8.3}$$

In order to solve the optimization problem efficiently, we use the IPA-SQP algorithm, which includes prediction-correction in approximating the optimal solution numerically. It uses neighboring extremal (NE) updates in the prediction step to improve computational efficiency [90]. The IPA-SQP approach combines the solutions derived using perturbation analysis (PA) and SQP. This approach updates the solution to the optimization problem at time t by considering it as a perturbation to the solution at time $(t-1)$ using neighboring optimal control theory [96] extended to discrete-time systems with constraints, and then corrects the results using SQP updates. The merged PA and SQP updates exploit the sequential form of predictor and corrector steps, thereby yielding a fast solver for nonlinear MPC problems [89]. The flowchart of IPA-SQP is shown in Figure 8.4 [5, 97], and illustrates the main steps of the IPA-SQP algorithm to obtain the NE solutions and to deal with changes in the activity status of constraints.

To implement the system-level controller, namely the EMS, component-level controllers are required to follow the reference power commands, as shown in Fig. 8.5. In the following sections, the component-level control development and validation will be presented first, then real-time feasibility is demonstrated by real-time simulation

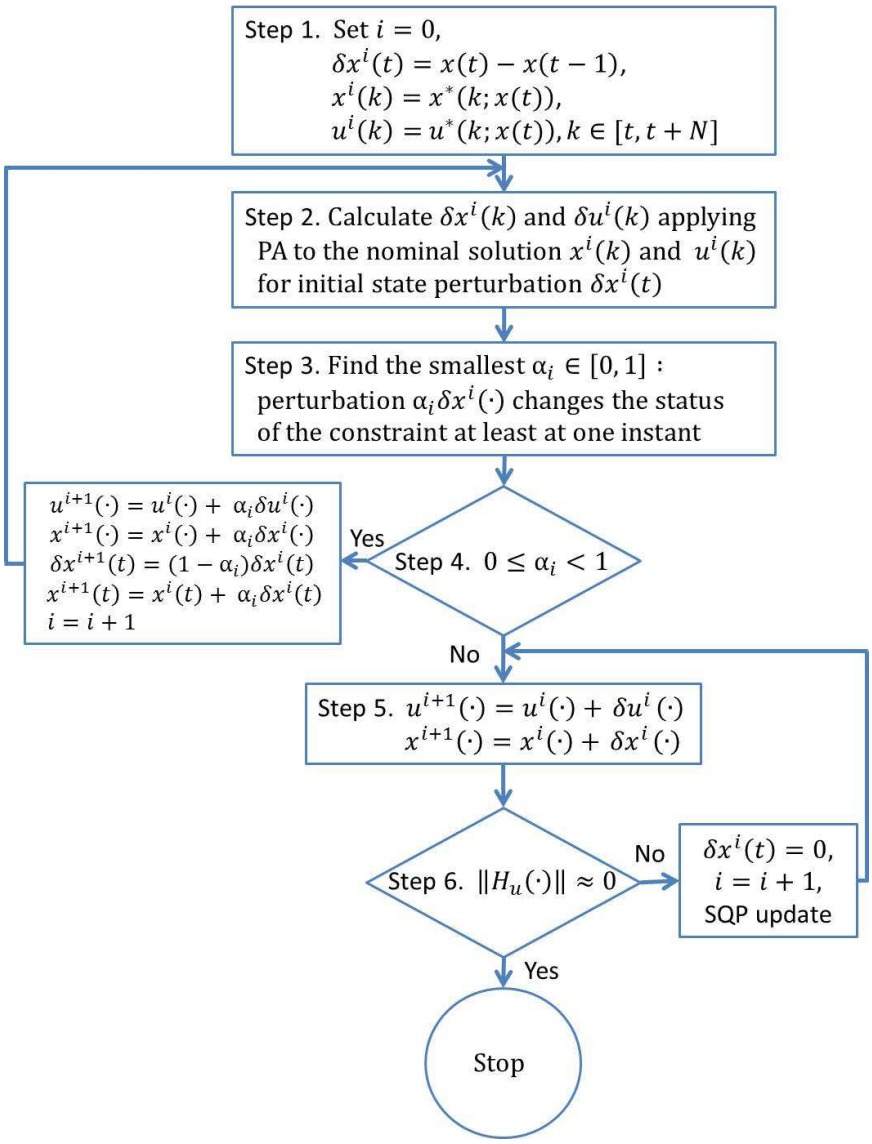

Figure 8.4: Flowchart of the IPA-SQP algorithm [5].

results. Finally, the overall experimental results are presented and analyzed.

8.3 Component-level Controller Development: Current Regulators for HESS

In our testbed, bi-directional DC/DC converters are used for HESS control. The circuit diagram of the bi-directional DC/DC converters is shown in Fig. 8.6. The

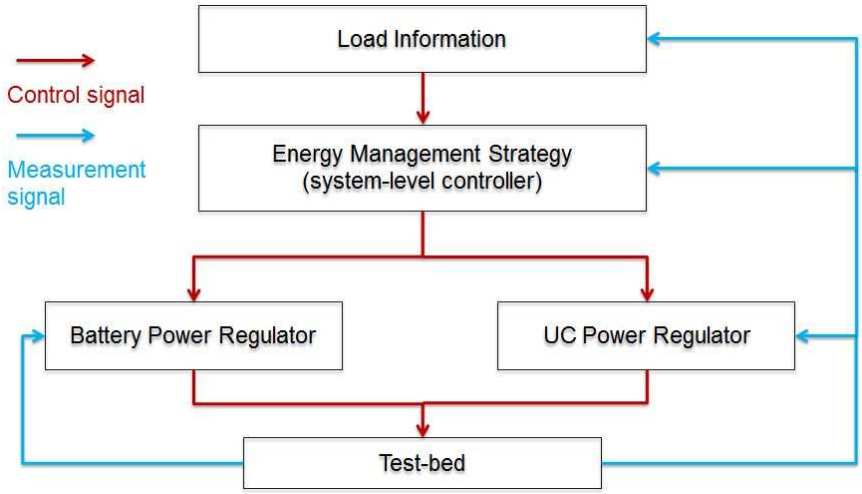

Figure 8.5: Hierarchical control structure for real-time control implementation.

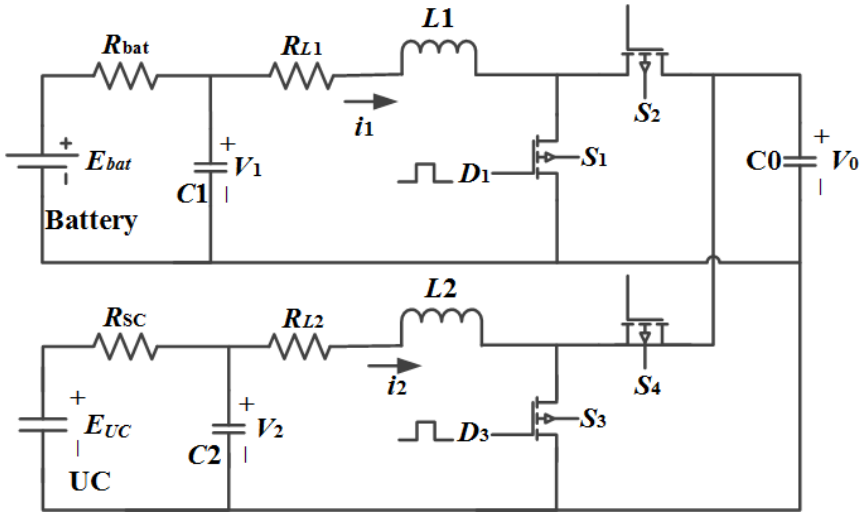

Figure 8.6: Circuit diagram of bi-directional DC/DC converters for HESS.

average-value model of the HESS can be described as follows:

$$
\begin{aligned}
\dot{V}_1 =& -\frac{V_1 + i_1 R_{bat} - E_{bat}}{C_1 R_{bat}}, \\
\dot{V}_2 =& -\frac{V_2 + i_2 R_{UC} - E_{UC}}{C_2 R_{UC}}, \\
\dot{i}_1 =& \frac{V_1 - i_1(R_{L1} + R_{on2}) - V_0 + D_1[i_1(R_{on2} - R_{on1}) + V_0]}{L_1}, \\
\dot{i}_2 =& \frac{V_2 - i_2(R_{L2} + R_{on4}) - V_0 + D_3[i_2(R_{on4} - R_{on3}) + V_0]}{L_2}, \\
\dot{V}_0 =& \frac{i_1 + i_2 - i_{load} - D_1 i_1 - D_3 i_2}{C_0},
\end{aligned}
\tag{8.4}
$$

where C_0 is the bus capacitor; C_1, and C_2 are the capacitors in parallel with the battery and UC, respectively; V_0, V_1 and V_2 are the voltages corresponding to capacitors C_0, C_1, and C_2, respectively; L_1, and L_2 are the inductors of the bi-directional DC/DC converters; i_1 and i_2 are the inductor currents; R_{L1}, and R_{L2} are the resistance of inductor L_1 and $L2$, respectively; and D_1 and D_3 are the duty cycle commands of the DC/DC converters.

As shown in Equation (8.4), the HESS with bi-directional converters is a nonlinear system, which requires a robust nonlinear approach. Sliding-mode control is a robust nonlinear control approach, which has been successfully applied to robot manipulators, vehicles, high-performance electric motors, and power systems [98]. In this chapter, the sliding-mode control is used to control the bi-directional DC/DC converters [69]. The sliding surface is defined as $S = [S_1, S_2]^T$, where $S_1 = i_{1ref} - i_1$ and $S_2 = i_{2ref} - i_2$.

In order to ensure the existence of the sliding-mode surface, the condition $\dot{S}S < 0$ must be satisfied. The differential sliding variable is set as:

$$\dot{S} = -kS - \varepsilon sat(S), \tag{8.5}$$

where the saturation function sat(S) is defined as:

$$sat(S_n) = \begin{cases} 1, & S_n \in (1, \infty), \\ S_n, & S_n \in [-1, 1], \\ -1, & S_n \in (-\infty, -1), \end{cases} \tag{8.6}$$

$n = 1, 2$, k and ε are the sliding-mode gains.

To simplify the solution, we assume that $R_{on1} = R_{on2}$ and $R_{on3} = R_{on4}$. Assuming a time scale separation (i.e., the current dynamic is much faster than the voltage dynamic due to large values for the capacitances C_0, C_1, and C_2), the voltages $V_{0,1,2}$

are assumed to be constant. Therefore, the sliding-mode control law is developed as follows:

$$\begin{bmatrix} D_1 \\ D_3 \end{bmatrix} = \begin{bmatrix} 1 - \frac{V_1}{V_0} + i_1 \frac{R_{L1}+R_{on2}}{V_0} + k_1 \frac{L_1}{V_0}(i_{bat,ref} - i_1) + \varepsilon_1 \frac{L_1}{V_0} sat(i_{bat,ref} - i_1) \\ 1 - \frac{V_2}{V_0} + i_2 \frac{R_{L2}+R_{on4}}{V_0} + k_2 \frac{L_2}{V_0}(i_{UC,ref} - i_2) + \varepsilon_2 \frac{L_2}{V_0} sat(i_{UC,ref} - i_2) \end{bmatrix}. \tag{8.7}$$

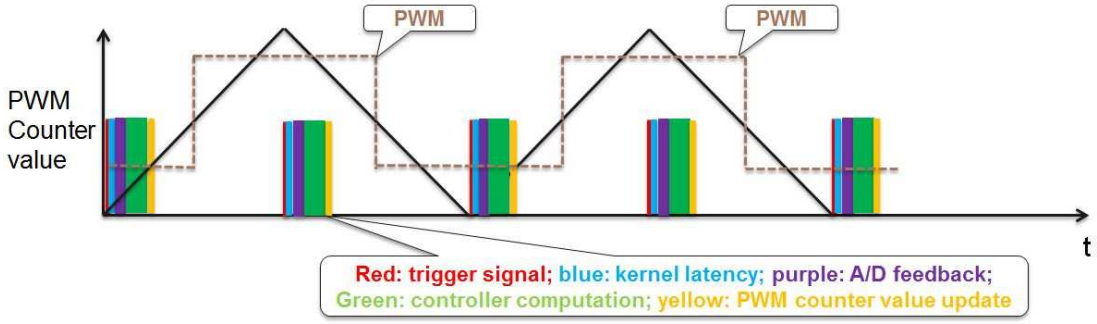

Figure 8.7: The implementation of Speedgoat controller.

To validate the performance of component-level controllers, the proposed sliding-mode control has been implemented in the MPEL AED-HES test-bed. The system controller, Speedgoat, supports Matlab Real-Time Simulink (xPC Target) to enable rapid prototyping of advanced control algorithms. The implementation of the Speedgoat controller is shown in Fig. 8.7. A center-based PWM trigger signal enables the synchronization of the PWM waveforms and analog-to-digital measurements. The trigger signal is generated at the center of PWM waveforms. The kernel of Speedgoat receives this trigger signal to read A/D feedback, and then initials the controller computation. Once the controller computation is completed, the PWM counter values are updated for the next switching period. This center-based trigger reduces the effects of noise, as the switching of the power electronic transistors and the sampling of the analog-to-digital converters are synchronized. Consequently, sampling always occurs in between switching transitions, avoiding the pick-up of electromagnetic in-

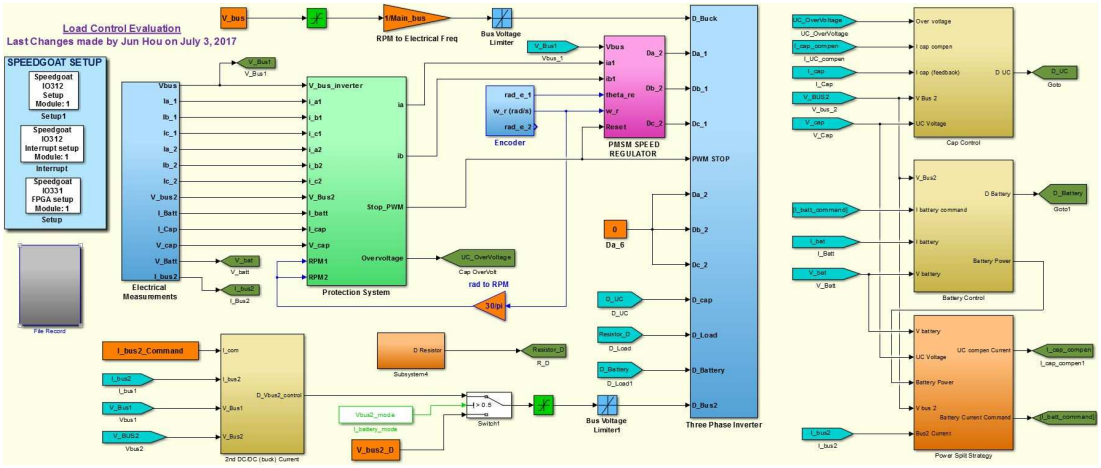

Figure 8.8: Matlab/Simulink program of the local controllers.

terference caused by the transitions. Center-based sampling is also able to measure the average value of the inductor current. However, due to hardware delays, a phase shift can cause measurement errors, which can be significant when the value of the measurement is small. Our double-sampling method, which samples twice within one switching period, can achieve more accurate average feedback. The Matlab/Simulink code is developed as shown in Fig. 8.8. As shown in Fig. 8.9, the actual output power of the HESS can follow the power reference quite accurately.

8.4 Experimental Implementation and Performance Evaluation

In addition to the efficient optimization algorithm described in the previous section, parallel computing using a multi-core structure can also increase the computational capabilities of our system [99, 100]. In this experiment, the system-level controller is executed in core 1, while the component-level controllers are executed in core 2. Both system-level and component-level controllers are synchronized with the center-based trigger signal. The multi-core structure in Matlab/Simulink is shown in Figure 8.10. A real-time simulation is performed to evaluate the computational

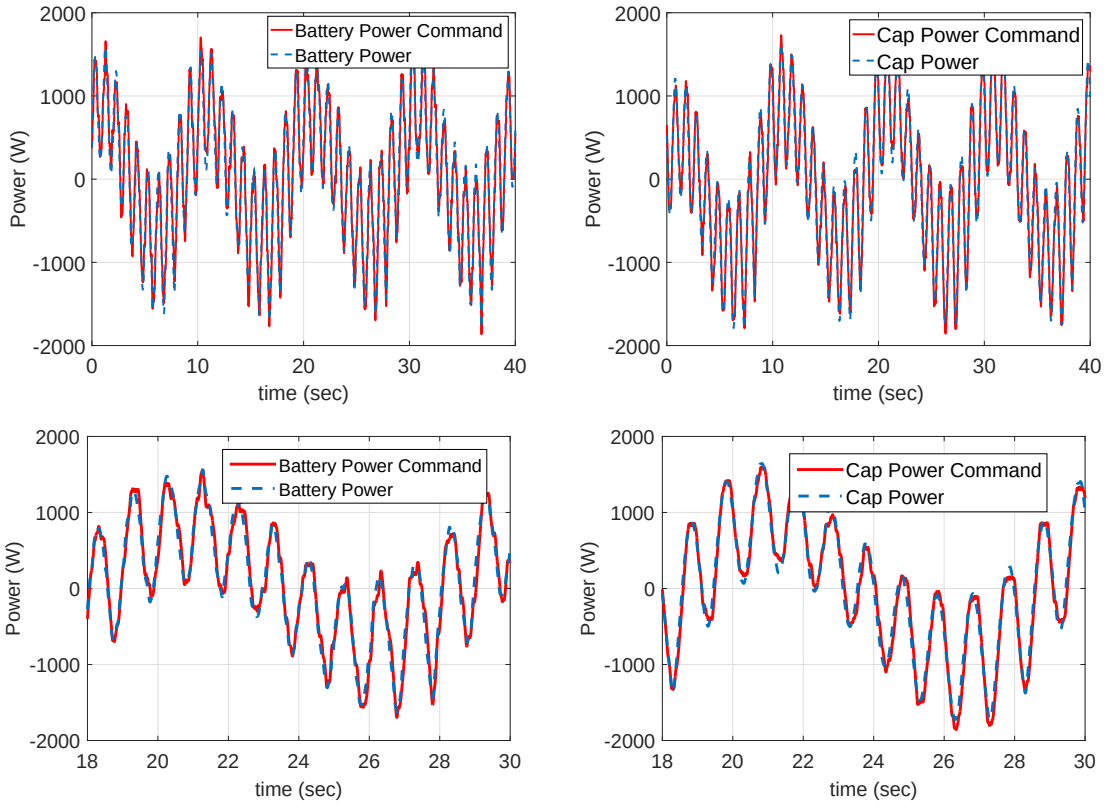

Figure 8.9: Control performance: battery and UC command power and actual power (zoom-in plots in the bottom).

capability of our proposed hierarchical real-time MPC. As shown in Figures 8.11 and 8.12, the maximum execution time for both cores 1 and 2 are much smaller than their corresponding sampling times.

In this experiment, the maximum voltage and the desired reference voltage of UC are defined as 150V and 145V, respectively. The maximum and minimum output currents of the battery and UC are 30A and -30A, respectively. The load fluctuations are scaled to a peak value of 2kW. Uncertainties, such as load uncertainties, parameter uncertainties, modeling uncertainties, and measurement uncertainties, exist in the system and can be used to evaluate the robustness of the proposed controller. A diagram of this experimental setup is shown in Fig. 8.13. A three-phase diode rectifier converts the AC power from the grid to DC power, and then a DC/DC converter

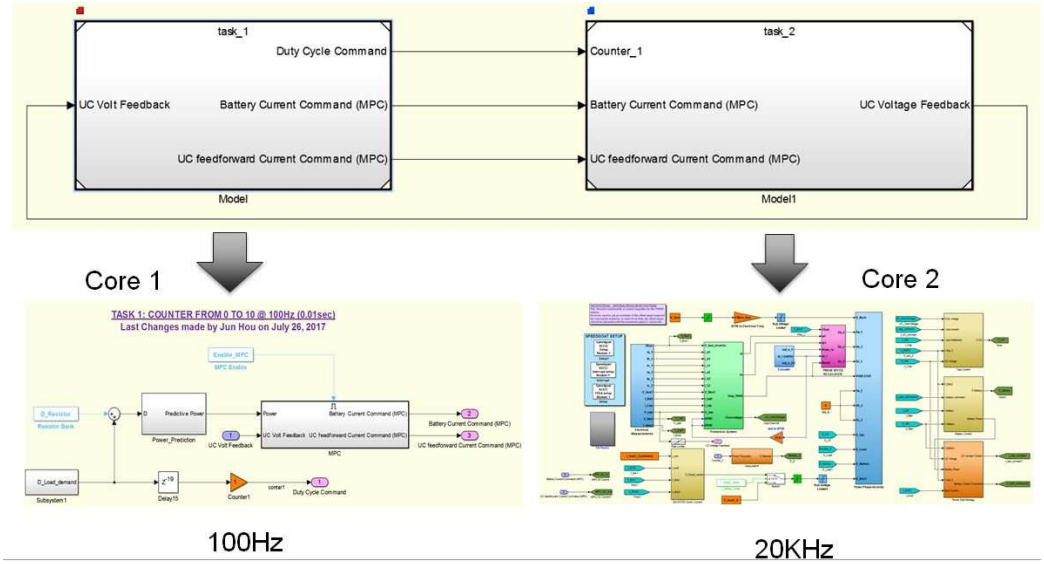

Figure 8.10: Multi-core structure of Speedgoat.

Figure 8.11: Real-time simulation evaluation of system-level controller (core1).

Figure 8.12: Real-time simulation evaluation of component-level controllers (core2).

"bucks" the DC voltage down to the nominal voltage. We note that a constant duty cycle is used for this DC/DC converter. In order to emulate the generator sets, the second DC/DC converter is controlled to provide the average power for the DC bus. The resistive load bank is controlled to emulate the load fluctuations by using the

propulsion-load model described in Chapter II. The HESS compensates the load fluctuations to maintain a constant DC bus voltage. The predictive horizon is chosen to be N=20. The experimental results of the filter-based and real-time MPC strategies are shown in Figs. 8.14 (sea state 4) and 8.15 (sea state 6).

The pulse power load is another important load fluctuation in the shipboard network. In the following experiments, we also evaluate the capability of the proposed HESS solution to address the propulsion load fluctuations with pulse power loads, as shown in Fig. 8.16. The following normalized performance metrics are used to compare the real-time MPC with the filter-based strategy:

1. Voltage variation (Vol%): $\frac{rms(Vbus_{MPC}-Vbus_{ref})}{rms(Vbus_{filter}-Vbus_{ref})} \times 100\%$;
2. Estimated HESS losses (HESS%): $\frac{Losses_{MPC}}{Losses_{filter}} \times 100\%$;
3. Battery peak current (Peak%): $\frac{max(|I_{B,MPC}|)}{max(|I_{B,filter}|)} \times 100\%$;
4. Battery RMS current (RMS%): $\frac{rms(I_{B,MPC})}{rms(I_{B,filter})} \times 100\%$.

Table 8.1: Performance comparison: filter-based vs. MPC.

	SS4	SS6	SS4 with Pulse
Vol%	61.96%	63.95%	71.10%
HESS%	34.05%	49.77%	35.82%
Peak%	51.11%	67.35%	53.50%
RMS%	40.99%	64.19%	50.36%

As shown in Table 8.1, compared with the filter-based strategy, the proposed real-time MPC can reduce the bus voltage variation to as low as 62% of the filter-based approach, and HESS total losses are reduced as low as 35% of the filter-based approach. Furthermore, the real-time MPC operates with much smaller battery peak and RMS currents than the filter-based strategy, leading to an extended battery life cycle. As shown in Figs. 8.14 - 8.16, the UC is operating around the desired reference voltage under the real-time MPC strategy, while the voltage of UC keeps decreasing under the filter-based strategy. The efficiency of the filter-based strategy will decrease

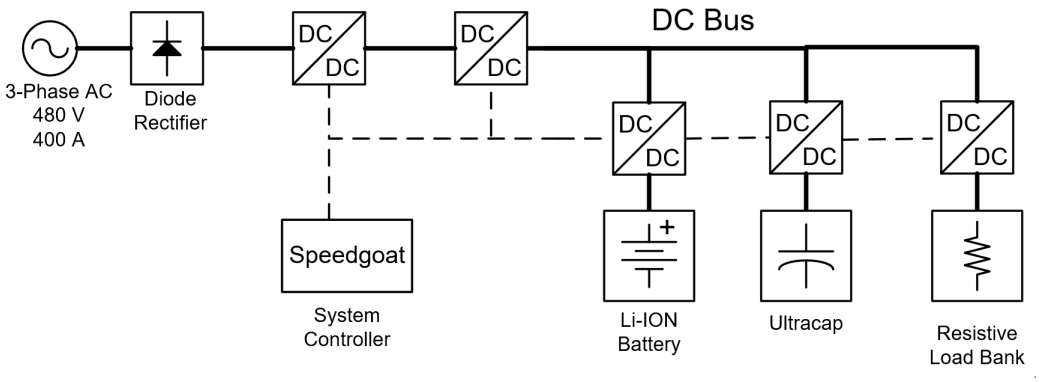

Figure 8.13: Diagram of real-time MPC experiment.

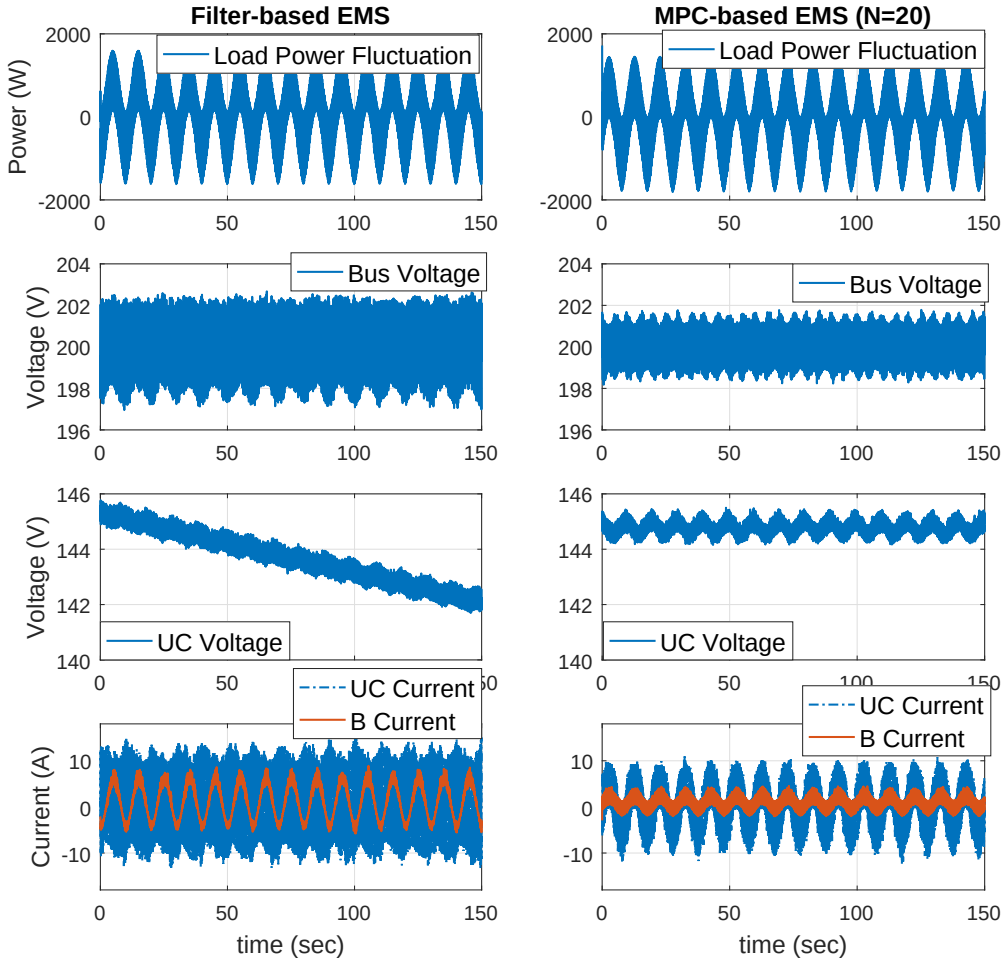

Figure 8.14: Experimental results of sea state 4: MPC vs. filter-based control

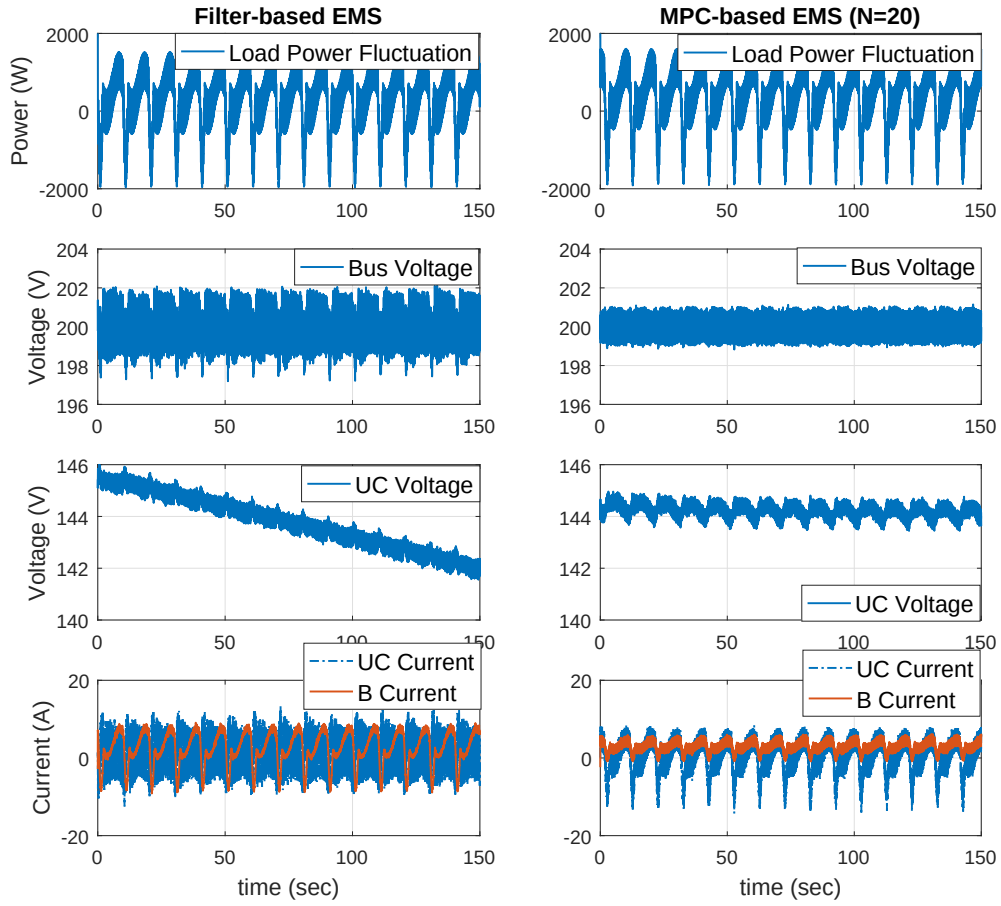

Figure 8.15: Experimental results of sea state 6: MPC vs. filter-based control.

as the UC voltage drops, and so the self-sustained time of the filter-based strategy is much shorter than the real-time MPC. In summary, compared to the baseline control, this experiment shows the effectiveness of the proposed real-time MPC in terms of enhanced system reliability, improved HESS efficiency, long self-sustained time, and extended battery life cycle.

The predictive horizon was found to be an important design parameter. Extending the predictive horizon will generally improve performance, at the cost of increased computational complexity. However, when uncertainties exist, performance improvement with increasing horizon is not guaranteed. In order to provide insight into the

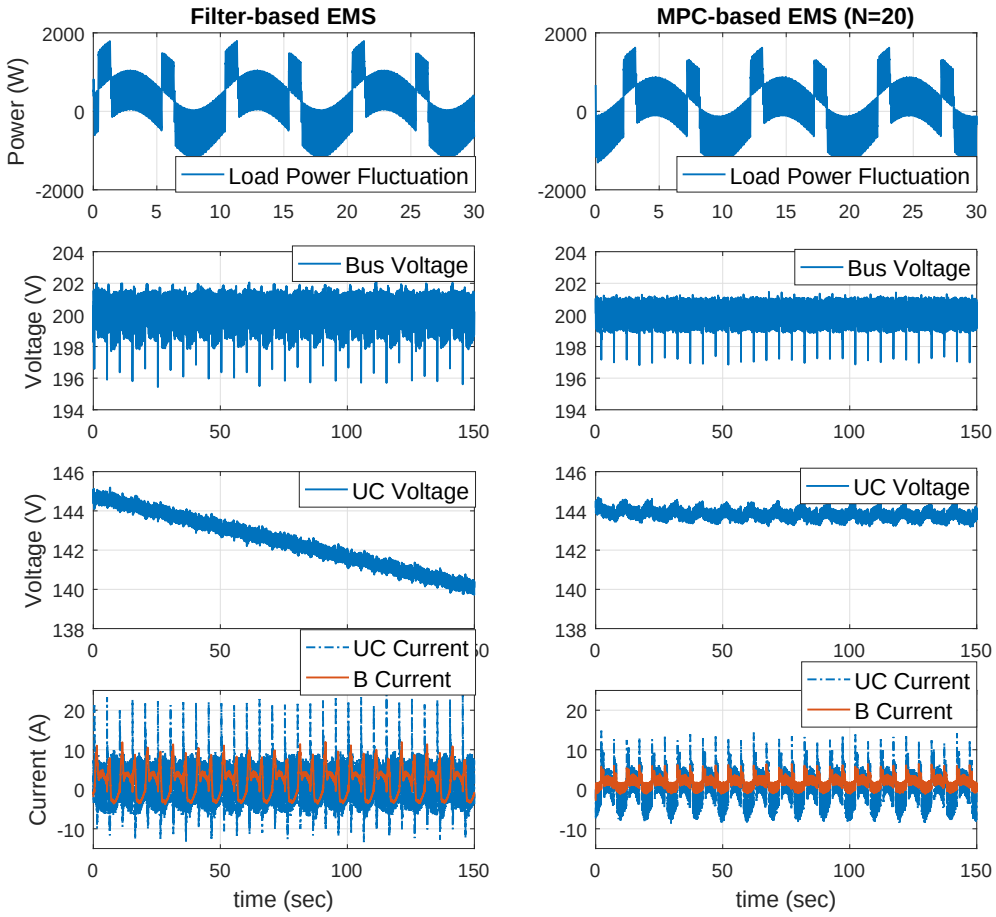

Figure 8.16: Experimental results of pulse power load: MPC vs. filter-based control.

predictive horizon, the real-time MPC with an extended predictive horizon N=40 is implemented on the testbed. The experimental results are shown in Figs.8.17 - 8.19. The normalized performance metrics are presented as follows:

1. Voltage variation (Vol%): $\frac{rms(Vbus_{N=40}-Vbus_{ref})}{rms(Vbus_{N=20}-Vbus_{ref})} \times 100\%$;
2. HESS losses (HESS%): $\frac{Losses_{N=40}}{Losses_{N=20}} \times 100\%$;
3. Battery peak current (Peak%): $\frac{max(|I_{B,N=40}|)}{max(|I_{B,N=20}|)} \times 100\%$;
4. Battery RMS current (RMS%): $\frac{rms(I_{B,N=40})}{rms(I_{B,N=20})} \times 100\%$.

Table 8.2: Performance comparison: MPC(N=20) vs. MPC(N=40).

	SS4	SS6	SS4 with Pulse
Vol%	102.27%	100.52%	101.45%
HESS%	101.86%	110.59%	98.55%
Peak%	107.69%	107.67%	98.30%
RMS%	105.94%	108.36%	100.44%

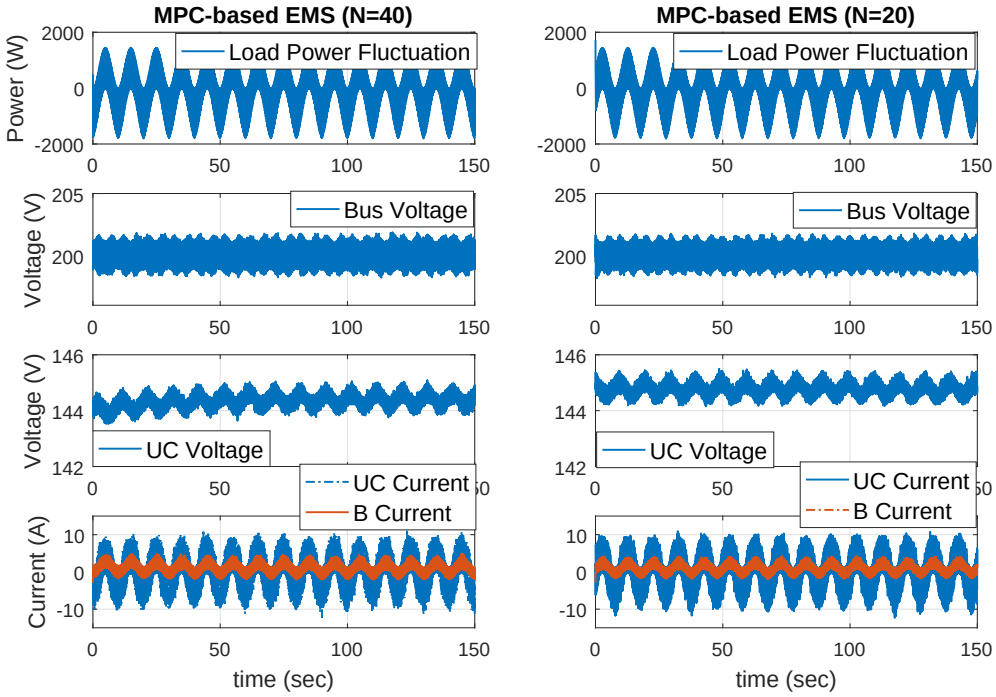

Figure 8.17: Experimental results of sea state 4: MPC(N=20) vs. MPC(N=40).

As shown in Table 8.2, MPC with N=40 does not outperform MPC with N=20 in most performance metrics. The real-time MPC only applies the first element of the control sequence as the control action before moving to the next sample, when new measurements are collected and the optimization is repeated with new initial conditions. This feedback mechanism is helpful to improve the robustness of the MPC strategy. However, as the predictive horizon increases, it is seen that uncertainties can affect the control performance more significantly than a short predictive horizon. In this study, therefore, the predictive horizon was chosen to be N=20.

Remark 8.1 As shown in Equation (8.1), this is nonlinear and nonconvex opti-

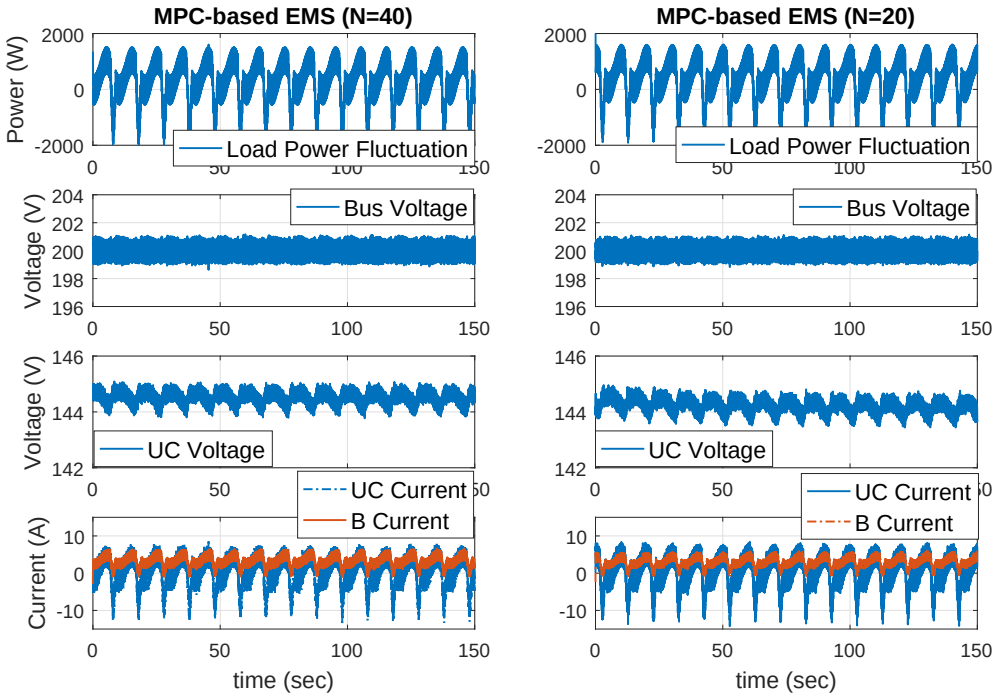

Figure 8.18: Experimental results of sea state 6: MPC(N=20) vs. MPC(N=40).

mization problem. To solve this optimization problem is a challenge for implementing the proposed MPC-based EMS in real-time applications. In this experiment, the output currents of HESS do not reach their corresponding physical constraints, namely -30A and 30A. It is important to understand the impact of constraints on solving the optimization problem, so a new real-time simulation case study is performed. The constraint of UC output current is changed from $[-30A, 30A]$ to $[-5A, 5A]$, and sea state 6 load profile is used. In this case study, the real-time simulation results are shown in Figure 8.20, where the UC current is always within its constraints. Furthermore, the iteration to solve the optimization problem is significantly increased when the UC current reaches its constraint. For example, the iteration is less than 15 (minimum: 3 times; maximum: 14 times) from 9 second to 11 second, while the iteration can be as high as 30 when the constraint is active, such as from 4 second to 6 second. The maximum execution time are shown in Figure 8.21 to validate the

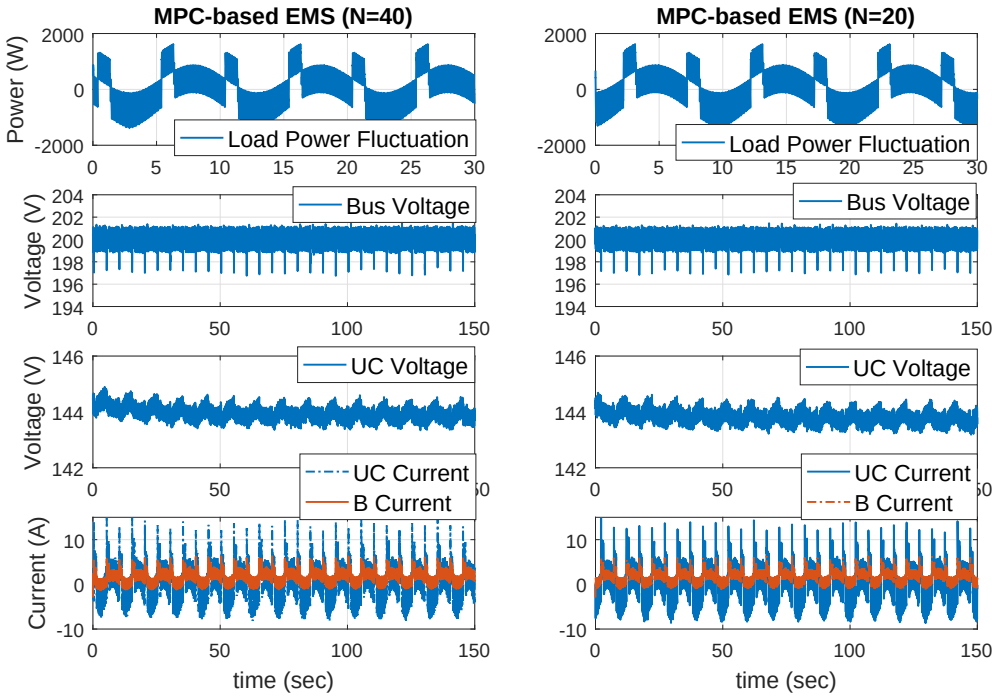

Figure 8.19: Experimental results of pulse power load: MPC(N=20) vs. MPC(N=40)

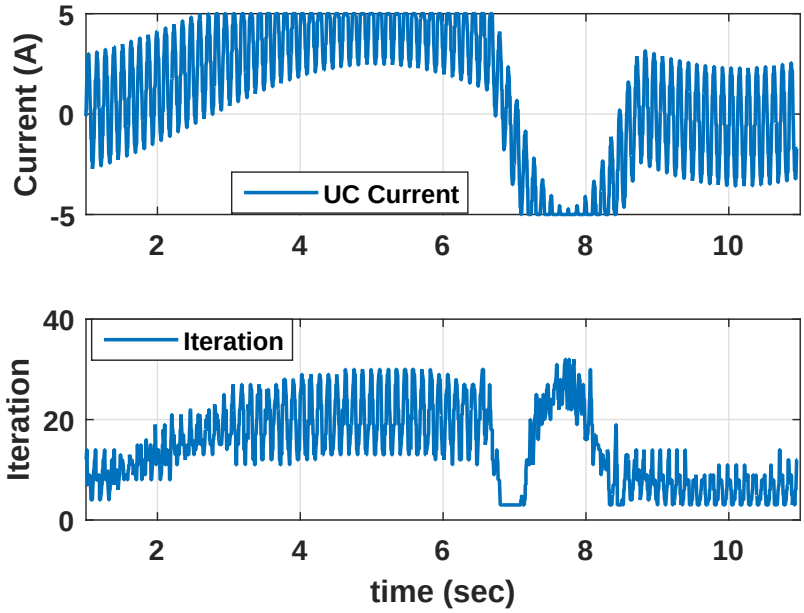

Figure 8.20: UC output current and the number of iteration to solve the optimization problem.

Figure 8.21: Real-time simulation comparison of maximum execution time.

real-time feasibility when the constraint is active. The blue and red bars represent the maximum execution time with the UC current constraint as $[-30A, 30A]$ and $[-5A, 5A]$, respectively. The green bar represents the sample time. As shown in Figure 8.21, although the computational time is increased when the constraint is active, it is still much smaller than its sample time.

8.5 Summary

In this chapter, the proposed real-time MPC has been implemented on the AED-HES testbed. In order to achieve real-time feasibility, three different efforts have been made: properly formulating the optimization problem, identifying an efficient optimization solver, and implementing the controller with a multi-core structure. Furthermore, effective HESS component current regulators using sliding-mode control have been developed and validated. Compared to the filter-based control, the proposed MPC demonstrated on the testbed can achieve superior performance in terms of reduced bus voltage variation, battery peak and RMS currents, and HESS losses. Given the uncertainties in the testbed, the robustness of the proposed MPC is also demonstrated.

CHAPTER IX

Conclusions and Future Work

9.1 Conclusions

This research has focused on the modeling, analysis, and control of an electric ship propulsion system with hybrid energy storage system (HESS), aiming at mitigating the effect of the propulsion load fluctuations. The tools development, namely modeling and testbed development, are presented in Chapter II and III, respectively. The feasibilities and effectiveness of HESS have been investigated in Chapter IV and V. Two energy management strategies (EMSs) have been proposed and analyzed with simulation results presented in Chapter VI. In Chapter VII, the propulsion load torque estimation and prediction that are needed to implement model predictive control (MPC) have been addressed by two approaches: adaptive load estimation/prediction with model predictive control and input observer with linear prediction. The real-time MPC is implemented on the test-bed in Chapter VIII. Compared to the filter-based strategy, the experimental results demonstrate the effectiveness of the proposed real-time MPC.

The main work and results are summarized as follows:

- Developed a control-oriented model for an all-electric ship propulsion system with hybrid energy storage. This model included a propeller and ship dynamic

model, hybrid energy storage models, a diesel engine and generator set model, a electrical motor model and a DC bus dynamic model. The propeller and ship dynamic model is the main contribution, which captured both high- and low-frequency load fluctuations on the propeller. The in-and-out-of-water effect are also taken into consideration in this model.

- Developed a hardware test-bed in order to support and demonstrate modeling and control solutions on a hardware platform. This test-bed included a system-level controller that can simultaneously control all of the power electronic converters interfacing with the HESS. My contributions to the test-bed development include the system controller, energy storages and DC/DC converters. Two preliminary experimental results, i.e., battery with UCs and flywheel with UCs, were presented to demonstrate the capabilities of the test-bed in control implementation and system integration for electric drive systems with HESS.

- Investigated the feasibility and effectiveness of different hybrid energy storage system configurations, namely battery combined with ultra-capacitor (B/UC) and battery with flywheel (B/FW), to mitigate load fluctuations. Dynamic programming was used to obtain the global optimal solutions. These global optimal solutions formed the basis of a comparative study of B/FW and B/UC HESS, where the Pareto fronts of these two technologies at different sea state (SS) conditions were derived. The analysis aimed to provide insights into the advantages and limitations of each HESS solution.

- Two MPC-based control strategies, coordinated model predictive control (CC-MPC) and pre-filtered model predictive control (PF-MPC), were designed and evaluated. The results indicated that the CC-MPC strategy outperforms the PF-MPC strategy in terms of power tracking, HESS efficiency, and self-sustained

operation time. A sensitivity analysis of the predictive horizon for the coordinated control showed the feasibility of MPC-based strategies for real-time applications. This study provided insights into the importance of the coordination of HESS.

- Developed two energy management strategies based on different integration configurations, namely "plug-in" and "integrated". For the "plug-in" approach, different strategies were investigated to address the effect of the load fluctuation in the electric ship propulsion system. Model-based analysis was performed to understand the interactions between HESS and generator control systems. To validate the interaction analysis and evaluate the benefits or limitations for each strategy, a comparative study was performed. Results showed that the proposed energy management system, i.e., the coordinated HESS EMS, is more effective in improving the system efficiency and reliability than other strategies. This work illustrated that a properly coordinated control is critical when introducing HESS into an existing electric ship propulsion system. For the "integrated" approach, a new energy management strategy was proposed to integrate power generation, electric motor, and hybrid energy storage control for electric ship propulsion systems in order to address the effects of power fluctuations in the shipboard network. Simulation results showed that the proposed strategy is effective at improving system efficiency, enhancing reliability, and reducing mechanical wear and tear.

- Developed two approaches to address propeller-load torque estimation and prediction. The first combined an input observer with linear prediction, and the second integrated parameter identification with model predictive control. A comparative study was performed to illustrate the effectiveness of the proposed model-based approach. The importance of load torque estimation and predic-

tion was also determined through this comparative study.

- The real-time MPC was implemented on the physical testbed. Three different efforts have been made to enable real-time feasibility: a specially tailored problem formulation, an efficient optimization algorithm and a multi-core hardware implementation. Component-level control was also developed to guarantee the system-level control performance. Compared to the filter-based control strategy, the proposed real-time MPC achieved much better performance in terms of the enhanced system reliability, improved HESS efficiency, long self-sustained time, and extended battery life cycle.

9.2 Ongoing and Future Research

Although substantial progress has been made on the modeling, analysis, optimization, and control of all-electric ship propulsion systems with hybrid energy storage to mitigate the impact of the propulsion load fluctuations, there are several ongoing and future research topics to address open issues. These research activities are highlighted in the following:

- *Improve computational efficiency for solving the load-following optimization problem with periodic load profiles*

  Propulsion-load fluctuations caused by the encounter waves and propeller rotation have a periodic characteristic, which could potentially be exploited to improve the computational efficiency and reduce the memory required for the load-following optimization problem. How to take advantage of this periodic characteristic is an ongoing research problem.

- *Energy management strategy implementation for integrated approach*

The energy management strategy for the plug-in approach has been implemented on the testbed and achieves desired performance. The EMS for the integrated approach requires more efforts on both system-level control and component-level control, as well as the hardware. The experimental validation of EMS for the integrated approach will be performed in the future research.

BIBLIOGRAPHY

BIBLIOGRAPHY

[1] Norbert Doerry. Naval power systems: Integrated power systems for the continuity of the electrical power supply. *IEEE Electrification Magazine*, 3(2):12–21, 2015.

[2] Torstein Ingebrigtsen Bø. *Scenario-and Optimization-Based Control of Marine Electric Power Systems*. PhD thesis, Norwegian University of Science and Technology, 2016.

[3] Bijan Zahedi, Lars E Norum, and Kristine B Ludvigsen. Optimized efficiency of all-electric ships by dc hybrid power systems. *Journal of power sources*, 255:341–354, 2014.

[4] John Kuseian. Naval power systems technology development roadmap. *Electric Ships Office, PMS*, 320, 2013.

[5] Hyeongjun Park. Real-time predictive control of constrained nonlinear systems using the ipa-sqp approach. 2014.

[6] Espen Skjong, Rune Volden, Egil Rødskar, Marta Molinas, Tor Arne Johansen, and Joseph Cunningham. Past, present, and future challenges of the marine vessels electrical power system. *IEEE Transactions on Transportation Electrification*, 2(4):522–537, 2016.

[7] Timothy J McCoy. Trends in ship electric propulsion. In *Power Engineering Society Summer Meeting, 2002 IEEE*, volume 1, pages 343–346. IEEE, 2002.

[8] Alf Kåre Ådnanes. *Maritime electrical installations and diesel electric propulsion*. ABB, 2003.

[9] Bijan Zahedi. *Shipboard DC Hybrid Power Systems: Modeling, efficiency analysis and stability control*. PhD thesis, Norwegian University of Science and Technology, 2014.

[10] Timothy J McCoy. Electric ships past, present, and future [technology leaders]. *IEEE Electrification Magazine*, 3(2):4–11, 2015.

[11] Norbert Doerry, John Amy, and Cy Krolick. History and the status of electric ship propulsion, integrated power systems, and future trends in the us navy. *Proceedings of the IEEE*, 103(12):2243–2251, 2015.

[12] Timothy J McCoy. Integrated power systemsan outline of requirements and functionalities for ships. *Proceedings of the IEEE*, 103(12):2276–2284, 2015.

[13] Norbert Doerry, Henry Robey, John Amy, and Chester Petry. Powering the future with the integrated power system. *Naval Engineers Journal*, 108(3):267–282, 1996.

[14] Herbert Ginn and Robert Cuzner. The shipboard integrated power system. *IEEE Electrification Magazine*, 1(2):2–3, 2015.

[15] So-Yeon Kim, Sehwa Choe, Sanggi Ko, and Seung-Ki Sul. A naval integrated power system with a battery energy storage system: Fuel efficiency, reliability, and quality of power. *IEEE Electrification Magazine*, 3(2):22–33, 2015.

[16] Andrea Vicenzutti, Daniele Bosich, Giovanni Giadrossi, and Giorgio Sulligoi. The role of voltage controls in modern all-electric ships: Toward the all electric ship. *IEEE Electrification Magazine*, 3(2):49–65, 2015.

[17] Gayathri Seenumani, Jing Sun, and Huei Peng. Real-time power management of integrated power systems in all electric ships leveraging multi time scale property. *IEEE Transactions on Control Systems Technology*, 20(1):232–240, 2012.

[18] Norbert Doerry and Kevin McCoy. Next generation integrated power system: Ngips technology development roadmap. Technical report, DTIC Document, 2007.

[19] Øyvind Notland Smogeli. *Control of marine propellers: From normal to extreme conditions*. PhD thesis, Norwegian University of Science and Technology, 2006.

[20] Damir Radan. *Integrated control of marine electrical power systems*. PhD thesis, Norwegian University of Science and Technology, 2008.

[21] Øyvind Notland Smogeli and Asgeir J Sørensen. Antispin thruster control for ships. *IEEE Transactions on Control Systems Technology*, 17(6):1362–1375, 2009.

[22] Øyvind N Smogeli, Asgeir J Sørensen, and Knut J Minsaas. The concept of anti-spin thruster control. *Control Engineering Practice*, 16(4):465–481, 2008.

[23] Asgeir J Sørensen and Øyvind N Smogeli. Torque and power control of electrically driven marine propellers. *Control Engineering Practice*, 17(9):1053–1064, 2009.

[24] Justin H McCarthy. On the calculation of thrust and torque fluctuations of propellers in nonuniform wake flow. Technical report, DTIC Document, 1961.

[25] John Carlton. *Marine propellers and propulsion*. Butterworth-Heinemann, 2012.

[26] Kourosh Koushan et al. Dynamics of propeller blade and duct loadings on ventilated thrusters in dynamic positioning mode. In *Dynamic positioning conference. Houston, USA*, 2007.

[27] RD Geertsma, RR Negenborn, K Visser, and JJ Hopman. Design and control of hybrid power and propulsion systems for smart ships: A review of developments. *Applied Energy*, 194:30–54, 2017.

[28] Robert E Hebner, Kent Davey, John Herbst, David Hall, Jonathan Hahne, Dwayne D Surls, and Abdelhamid Ouroua. Dynamic load and storage integration. *Proceedings of the IEEE*, 103(12):2344–2354, 2015.

[29] Srdjan M Lukic, Jian Cao, Ramesh C Bansal, Fernando Rodriguez, and Ali Emadi. Energy storage systems for automotive applications. *IEEE Transactions on industrial electronics*, 55(6):2258–2267, 2008.

[30] Siang Fui Tie and Chee Wei Tan. A review of energy sources and energy management system in electric vehicles. *Renewable and Sustainable Energy Reviews*, 20:82–102, 2013.

[31] Joel R Anstrom, Benjamin Zile, Kandler Smith, H Hofmann, and A Batra. Simulation and field-testing of hybrid ultra-capacitor/battery energy storage systems for electric and hybrid-electric transit vehicles. In *Applied Power Electronics Conference and Exposition*, volume 1, pages 491–497, 2005.

[32] Micah Ortúzar, Jorge Moreno, and Juan Dixon. Ultracapacitor-based auxiliary energy system for an electric vehicle: Implementation and evaluation. *IEEE Transactions on industrial electronics*, 54(4):2147–2156, 2007.

[33] Ziyou Song, Heath Hofmann, Jianqiu Li, Jun Hou, Xuebing Han, and Minggao Ouyang. Energy management strategies comparison for electric vehicles with hybrid energy storage system. *Applied Energy*, 134:321–331, 2014.

[34] Ziyou Song, Heath Hofmann, Jianqiu Li, Jun Hou, Xiaowu Zhang, and Minggao Ouyang. The optimization of a hybrid energy storage system at subzero temperatures: Energy management strategy design and battery heating requirement analysis. *Applied Energy*, 159:576–588, 2015.

[35] Ziyou Song, Jun Hou, Shaobing Xu, Minggao Ouyang, and Jianqiu Li. The influence of driving cycle characteristics on the integrated optimization of hybrid energy storage system for electric city buses. *Energy*, 135:91–100, 2017.

[36] Francisco Díaz-González, Andreas Sumper, Oriol Gomis-Bellmunt, and Roberto Villafáfila-Robles. A review of energy storage technologies for wind power applications. *Renewable and Sustainable Energy Reviews*, 16(4):2154–2171, 2012.

[37] Sam Koohi-Kamali, VV Tyagi, NA Rahim, NL Panwar, and H Mokhlis. Emergence of energy storage technologies as the solution for reliable operation of

smart power systems: A review. *Renewable and Sustainable Energy Reviews*, 25:135–165, 2013.

[38] Tarik Kousksou, Pascal Bruel, Abdelmajid Jamil, T El Rhafiki, and Youssef Zeraouli. Energy storage: Applications and challenges. *Solar Energy Materials and Solar Cells*, 120:59–80, 2014.

[39] Gastón Orlando Suvire, Marcelo Gustavo Molina, and Pedro Enrique Mercado. Improving the integration of wind power generation into ac microgrids using flywheel energy storage. *IEEE Transactions on smart grid*, 3(4):1945–1954, 2012.

[40] Jae-Do Park, Claude Kalev, and Heath F Hofmann. Control of high-speed solid-rotor synchronous reluctance motor/generator for flywheel-based uninterruptible power supplies. *IEEE Transactions on Industrial Electronics*, 55(8):3038–3046, 2008.

[41] Wenjie Chen, Alf Kåre Ådnanses, Jan Fredrik Hansen, John Olav Lindtjørn, and Tianhao Tang. Super-capacitors based hybrid converter in marine electric propulsion system. In *Electrical Machines (ICEM), 2010 XIX International Conference on*, pages 1–6. IEEE, 2010.

[42] Hyeongjun Park, Jing Sun, Steven Pekarek, Philip Stone, Daniel Opila, Richard Meyer, Ilya Kolmanovsky, and Raymond DeCarlo. Real-time model predictive control for shipboard power management using the ipa-sqp approach. *IEEE Transactions on Control Systems Technology*, 23(6):2129–2143, 2015.

[43] Saurabh Kulkarni and Surya Santoso. Impact of pulse loads on electric ship power system: With and without flywheel energy storage systems. In *2009 IEEE Electric Ship Technologies Symposium*, pages 568–573. IEEE, 2009.

[44] Lori N Domaschk, Abdelhamid Ouroua, Robert E Hebner, Oscar E Bowlin, and WB Colson. Coordination of large pulsed loads on future electric ships. *IEEE transactions on Magnetics*, 43(1):450–455, 2007.

[45] Ahmed T Elsayed and Osama A Mohammed. Distributed flywheel energy storage systems for mitigating the effects of pulsed loads. In *2014 IEEE PES General Meeting— Conference & Exposition*, pages 1–5. IEEE, 2014.

[46] Ahmed T Elsayed and Osama A Mohammed. A comparative study on the optimal combination of hybrid energy storage system for ship power systems. In *2015 Electric Ship Technologies Symposium (ESTS)*, pages 140–144. IEEE, 2015.

[47] Torstein Ingebrigtsen Bø and Tor Arne Johansen. Battery power smoothing control in a marine electric power plant using nonlinear model predictive control. *IEEE Transactions on Control Systems Technology*, 2016.

[48] Michel R Miyazaki, Asgeir J Sørensen, and Bjørn J Vartdal. Reduction of fuel consumption on hybrid marine power plants by strategic loading with energy storage devices. *IEEE Power and Energy Technology Systems Journal*, 3(4):207–217, 2016.

[49] Yichao Tang and Alireza Khaligh. On the feasibility of hybrid battery/ultracapacitor energy storage systems for next generation shipboard power systems. In *2010 IEEE Vehicle Power and Propulsion Conference*, pages 1–6. IEEE, 2010.

[50] Ali Haseltalab, Rudy R Negenborn, and Gabriel Lodewijks. Multi-level predictive control for energy management of hybrid ships in the presence of uncertainty and environmental disturbances. *IFAC-PapersOnLine*, 49(3):90–95, 2016.

[51] Jun Hou, Jing Sun, and Heath Hofmann. Mitigating power fluctuations in electric ship propulsion with hybrid energy storage system: Design and analysis. *IEEE Journal of Oceanic Engineering*, 2017, to be published. [Online]. Available: http://ieeexplore.ieee.org/document/7887693/.

[52] Jun Hou, Jing Sun, and Heath Hofmann. Mitigating power fluctuations in electrical ship propulsion using model predictive control with hybrid energy storage system. In *2014 American Control Conference*, pages 4366–4371. IEEE, 2014.

[53] Jun Hou, Jing Sun, and Heath Hofmann. Battery/flywheel hybrid energy storage to mitigate load fluctuations in electric ship propulsion systems. In *2017 American Control Conference (ACC)*, pages 1296–1301. IEEE, 2017.

[54] Jun Hou, Jing Sun, and Heath Hofmann. Interaction analysis and integrated control of hybrid energy storage and generator control system for electric ship propulsion. In *2015 American Control Conference (ACC)*, pages 4988–4993. IEEE, 2015.

[55] Jun Hou, Jing Sun, and Heath Hofmann. Integrated control of power generation, electric motor and hybrid energy storage for all-electric ships. In *2016 American Control Conference (ACC)*, pages 6797–6802. IEEE, 2016.

[56] Jing Sun. Optimisation-based control for electrified vehicles: challenges and opportunities. *Journal of Control and Decision*, 2(1):46–63, 2015.

[57] Philip Stone, Daniel F Opila, Hyeongjun Park, Jing Sun, Steve Pekarek, Ray DeCarlo, Eric Westervelt, James Brooks, and Gayathri Seenumani. Shipboard power management using constrained nonlinear model predictive control. In *2015 Electric Ship Technologies Symposium (ESTS)*, pages 1–7. IEEE, 2015.

[58] Pengfei Liu, Mohammed Islam, and Brian Veitch. Some unsteady propulsive characteristics of a podded propeller unit under maneuvering operation. In

Proceedings of the First International Symposium on Marine Propulsors-smp09, pages 507–516, 2009.

[59] Tristian Perez, Øyvind N Smogeli, Thor I Fossen, and Asgeir J Sørensen. An overview of the marine systems simulator (mss): A simulink® toolbox for marine control systems. *Modeling, identification and Control*, 27(4):259–275, 2006.

[60] Tor A Johansen, Torstein I Bø, Eirik Mathiesen, Aleksander Veksler, and Asgeir J Sørensen. Dynamic positioning system as dynamic energy storage on diesel-electric ships. *IEEE Transactions on Power Systems*, 29(6):3086–3091, 2014.

[61] Damir Radan, Asgeir J Sørensen, Alf Kåre Ådnanes, and Tor A Johansen. Reducing power load fluctuations on ships using power redistribution control. *Marine Technology*, 45(3):162–174, 2008.

[62] Aleksander Veksler, Tor Arne Johansen, and Roger Skjetne. Thrust allocation with power management functionality on dynamically positioned vessels. In *2012 American Control Conference (ACC)*, pages 1468–1475. IEEE, 2012.

[63] Jun Hou, David M Reed, Kan Zhou, Heath Hofmann, and Jing Sun. Modeling and test-bed development for an electric drive system with hybrid energy storage. In *Electric Machines Technology Symposium*, 2014.

[64] Jun Hou, David M Reed, Heath Hofmann, and Jing Sun. A low-voltage test-bed for electric ship propulsion systems with hybrid energy storage. In *Advanced Machinery Technology Symposium (AMTS)*. ASNE, 2016.

[65] Jun Hou, David M Reed, Heath Hofmann, and Jing Sun. A low-voltage test-bed for electric ship propulsion systems with hybrid energy storage. *Naval Engineers Journal*, 2017, under review.

[66] Jun Hou, Jing Sun, and Heath Hofmann. Control development and performance evaluation for battery/flywheel hybrid energy storage solutions to mitigate load fluctuations in all-electric ship propulsion systems. 2017, under review.

[67] Jun Hou, Ziyou Song, Hyeongjun Park, Jing Sun, and Heath Hofmann. Real-time model predictive control for load fluctuations mitigation in all-electric ship propulsion systems. 2017, under preparation.

[68] Jun Hou, Jing Sun, and Heath Hofmann. Adaptive mpc with propulsion load estimation and prediction for all-electric ship energy management. 2017, under review.

[69] Ziyou Song, Jun Hou, Heath Hofmann, Jianqiu Li, and Minggao Ouyang. Sliding-mode and lyapunov function-based control for battery/supercapacitor hybrid energy storage system used in electric vehicles. *Energy*, 122:601–612, 2017.

[70] MM Barnitsas, D Ray, and P Kinley. Kt, kq and efficiency curves for the wageningen b-series propellers. Technical report, University of Michigan, 1981.

[71] HydroComp. Correlating propeller performance with kt/kq multipliers. Technical report, HydroComp, Inc., 2003.

[72] Kenneth John Rawson. *Basic ship theory*, volume 1. Butterworth-Heinemann, 2002.

[73] Zhen Li. *Path following with roll constraints for marine surface vessels in wave fields*. PhD thesis, The University of Michigan, 2009.

[74] R.L. Beck and J. Wolfe. Developing a ship motions prediction program using linear theory for a ship maneuvering through a seaway. Technical report, Technical Report, 2007.

[75] D. Peng. Propeller design report. Technical report, Technical Report, 2009.

[76] Min Chen and Gabriel A Rincon-Mora. Accurate electrical battery model capable of predicting runtime and iv performance. *IEEE transactions on energy conversion*, 21(2):504–511, 2006.

[77] Petar J Grbovic. *Ultra-capacitors in power conversion systems: analysis, modeling and design in theory and practice*. John Wiley & Sons, 2013.

[78] Reed T Doucette and Malcolm D McCulloch. A comparison of high-speed flywheels, batteries, and ultracapacitors on the bases of cost and fuel economy as the energy storage system in a fuel cell based hybrid electric vehicle. *Journal of Power Sources*, 196(3):1163–1170, 2011.

[79] Dongxiang Yan, Languang Lu, Zhe Li, Xuning Feng, Minggao Ouyang, and Fachao Jiang. Durability comparison of four different types of high-power batteries in hev and their degradation mechanism analysis. *Applied Energy*, 179:1123–1130, 2016.

[80] Eduardo F Camacho and Carlos Bordons Alba. *Model predictive control*. Springer Science & Business Media, 2013.

[81] David Q Mayne. Model predictive control: Recent developments and future promise. *Automatica*, 50(12):2967–2986, 2014.

[82] M Bash, RR Chan, J Crider, C Harianto, J Lian, J Neely, SD Pekarek, SD Sudhoff, and N Vaks. A medium voltage dc testbed for ship power system research. In *2009 IEEE Electric Ship Technologies Symposium (ESTS)*, 2009.

[83] Jorge Solsona, Maria I Valla, and Carlos Muravchik. Nonlinear control of a permanent magnet synchronous motor with disturbance torque estimation. *IEEE Transactions on Energy Conversion*, 15(2):163–168, 2000.

[84] Chia-Shang Liu and Huei Peng. Disturbance observer based tracking control. *Journal of Dynamic Systems, Measurement, and Control*, 122(2):332–335, 2000.

[85] Ilya Kolmanovsky, Irina Sivergina, and Jing Sun. Simultaneous input and parameter estimation with input observers and set-membership parameter bounding: theory and an automotive application. *International Journal of Adaptive Control and Signal Processing*, 20(5):225–246, 2006.

[86] Wen-Hua Chen, Jun Yang, Lei Guo, and Shihua Li. Disturbance-observer-based control and related methodsan overview. *IEEE Transactions on Industrial Electronics*, 63(2):1083–1095, 2016.

[87] PP Vaidyanathan. The theory of linear prediction. *Synthesis lectures on signal processing*, 2(1):1–184, 2007.

[88] Petros A Ioannou and Jing Sun. Robust adaptive control, 2012.

[89] R. Ghaemi. *Robust model based control of constrained systems*. PhD thesis, The University of Michigan, 2010.

[90] Hyeongjun Park, Jing Sun, and Ilya Kolmanovsky. A tutorial overview of ipa-sqp approach for optimization of constrained nonlinear systems. In *Intelligent Control and Automation (WCICA), 2014 11th World Congress on*, pages 1735–1740. IEEE, 2014.

[91] Marco Cupelli, Ferdinanda Ponci, Giorgio Sulligoi, Andrea Vicenzutti, Chris S Edrington, Touria El-Mezyani, and Antonello Monti. Power flow control and network stability in an all-electric ship. *Proceedings of the IEEE*, 103(12):2355–2380, 2015.

[92] Luis Herrera, Wei Zhang, and Jin Wang. Stability analysis and controller design of dc microgrids with constant power loads. *IEEE Transactions on Smart Grid*, 8(2):881–888, 2017.

[93] Noshin Omar, Mohamed Abdel Monem, Yousef Firouz, Justin Salminen, Jelle Smekens, Omar Hegazy, Hamid Gaulous, Grietus Mulder, Peter Van den Bossche, Thierry Coosemans, et al. Lithium iron phosphate based battery–assessment of the aging parameters and development of cycle life model. *Applied Energy*, 113:1575–1585, 2014.

[94] Masoud Masih-Tehrani, Mohammad-Reza Ha'iri-Yazdi, Vahid Esfahanian, and Ali Safaei. Optimum sizing and optimum energy management of a hybrid energy storage system for lithium battery life improvement. *Journal of Power Sources*, 244:2–10, 2013.

[95] John Wang, Ping Liu, Jocelyn Hicks-Garner, Elena Sherman, Souren Soukiazian, Mark Verbrugge, Harshad Tataria, James Musser, and Peter Finamore. Cycle-life model for graphite-lifepo 4 cells. *Journal of Power Sources*, 196(8):3942–3948, 2011.

[96] A. Bryson and Y. Ho. *Applied optimal control: optimization, estimation, and control*. Taylor & Francis, 1975.

[97] Y. Xie, R. Ghaemi, J. Sun, and J. Freudenberg. Model predictive control for a full bridge dc/dc converter. *IEEE Transactions on Control Systems Technology*, 20(1):164–172, 2012.

[98] Jean-Jacques E Slotine, Weiping Li, et al. *Applied nonlinear control*, volume 199. Prentice hall Englewood Cliffs, NJ, 1991.

[99] Piotr Luszczek. Enhancing multicore system performance using parallel computing with matlab. *MATLAB Digest*, 17(5), 2008.

[100] Jeremy Kepner. *Parallel MATLAB for multicore and multinode computers*. SIAM, 2009.